ELECTROCHEMICAL AND COMPUTATIONAL STUDY OF OXYGEN REDUCTION REACTION ON NON-PRECIOUS TRANSITION METAL/NITROGEN DOPED CARBON MATERIALS

by

Kexi Liu

B.S., Tsinghua University, China, 2012

Submitted to the Graduate Faculty of

the Swanson School of Engineering in partial fulfillment

of the requirements for the degree of

Doctor of Philosophy

University of Pittsburgh

2017

UNIVERSITY OF PITTSBURGH

SWANSON SCHOOL OF ENGINEERING

This dissertation was presented

by

Kexi Liu

It was defended on

November 3rd, 2017

and approved by

Guofeng Wang, Ph.D., Associate Professor, Department of Mechanical Engineering and Materials Science

Albert C. To, Ph.D., Associate Professor, Department of Mechanical Engineering and Materials Science

Ian Nettleship, Ph.D., Associate Professor, Department of Mechanical Engineering and Materials Science

Scott X. Mao, Ph.D., Professor, Department of Mechanical Engineering and Materials Science

John A. Keith, Ph.D., Assistant Professor, Department of Chemical and Petroleum Engineering

Dissertation Director: **Guofeng Wang**, Ph.D., Associate Professor, Department of Mechanical Engineering and Materials Science

ELECTROCHEMICAL AND COMPUTATIONAL STUDY OF OXYGEN REDUCTION REACTION ON NON-PRECIOUS TRANSITION METAL/NITROGEN DOPED CARBON MATERIALS

Kexi Liu, PhD

University of Pittsburgh, 2017

An important challenge in low temperature fuel cell development is to find high performance non-precious catalysts replacing expensive platinum cathode catalysts for oxygen reduction reaction (ORR). The recently developed transition metal/nitrogen doped carbon-based materials (TM-N-C) exhibited catalytic activity close to that of platinum, but there are still many questions under debate. In this thesis, electrochemical and computational methods were employed to reveal the ORR mechanism on TM-N-C catalysts.

In the experimental aspect, a cost-effective two-step process, electrospinning and pyrolysis, was developed to produce the TM-N-C catalysts. The electrochemical techniques were applied to the catalytic property characterization of the synthesized catalysts, showing that the Fe-N-C catalyst possesses higher activity than the Co-N-C catalyst and could promote $4e^-$ pathway, while O_2 electroreduction was found to proceed mainly with $2e^-$ pathway yielding hydrogen peroxide on the Co-N-C catalyst.

In the computational aspect, the first-principles density functional theory (DFT) was employed to calculate the adsorption energies and activation energies, elucidating the ORR mechanism on TM-N_4 type active sites. Based upon the calculation results, the linear correlation between the O_2 adsorption energy and the non-bonding d orbitals center in the transition metal macrocyclic complexes was established. The free energy diagram extracted from the calculation results uncovered that the ORR could happen through $4e^-$ associative pathway on the FeN_4 site, whereas might end with a $2e^-$ pathway on the CoN_4 site due

to high energy barrier for O-O bond splitting, supporting the experimental observations. The superior activity of TM-N-C catalysts in alkaline than in acid was well-explained by the activity loss of the coexisted metal-free active sites induced by pyridinic nitrogen protonation in acid. Moreover, the microkinetic analysis was demonstrated to interpret DFT calculated energy parameters as polarization curves. With this tool, the study of the local carbon structures in the Fe-N-C catalysts directly revealed that the introduction of micropores could enhance their catalytic activity through facilitating the formation of FeN_4-C_8 active sites with high specific activity.

Keywords: polymer electrolyte fuel cell, oxygen reduction reaction, non-precious metal catalysts, electrospinning, voltammetry, density functional theory, binding energy, activation energy, nudged elastic band method, catalytic mechanism, microkinetic model.

TABLE OF CONTENTS

LIST OF TABLES

LIST OF FIGURES

PREFACE

The PhD study is such a long journey full of challenges. There are successes and failures, gain and loss, happinesses and frustrations. I can't get through this journey without those people who have guided me, helped me, and supported me in this process.

First of all, I would like to acknowledge my doctoral advisor Prof. Guogeng Wang. I am so fortunate to have him as my mentor since his kindness, patience and encouragement drived me to keep moving so far on the academic path. His guidence, instructions, and inspirations brought positive influence to me and will benefit me in the future.

I am grateful to my doctoral committee members Prof. Albert C. To, Prof. Scott X. Mao, Prof. Ian Nettleship, and Prof. John A. Keith for their insightful comments on my research work. I am specially grateful to Prof. Scott X. Mao for providing me the lab space so that I could complete the experiments.

I owe much appreciation to my friends and colleagues in the research group of Prof. Guofeng Wang, especially Dr. Shyam Kattel, Dr. Yinkai Lei, Dr. Zhiyao Duan, Dr. Corinne Gray, Zhenyu Liu, Boyang Li, Siming Zhang for their effort and help in this work and the joy times and so much fun we had together.

I am grateful to my experiment collaborators Dr. Xingxu Yan and Prof. Jun Luo. Without Xingxu's work and discussions, we would not have such fruitful research results. It is also him who trained me when I was an undergraduate at Tsinghua University. And Prof. Luo led my research at that time. I appreciated to their guidance at my beginning of academic journey.

Last but not least, I would like to thank my mom for her unconditional love and support. I am thankful to my grandma for her accompanying during my childhood. And, my dad, I wish you could see this too.

1.0 INTRODUCTION

Every year, humans consume a large amount of energy to sustain our lives. According to International Energy Agency, fossil fuels supply about 81% of the world's energy [1]. In the past few decades, the demand of world for oil and natural gas continues to grow. Developing renewable energy and imrpoving energy efficiency have become important issues. Along with energy shortage, burning fossil fuels also brought our society environmental problems such as greenhouse gas emissions and particulate matter (PM) pollution. It is a big challenge to alleviate these social problems nowadays. It is noteworthy that about 19% of energy consumption is in the transportation sector [1]. The internal combustion engine (ICE) used in most vehicles has low thermal efficiency and considerable exhaust emissions. In the new trend, the polymer electrolyte fuel cell (PEFC) is of great potential to replace the ICE for automobile driving.

A fuel cell is a device which consumes fuel and converts its chemical energy into electricity. The first fully developed fuel cell type is the alkaline fuel cell (AFC) which was commercially used as power systems in NASA space programs [2]. Since then, other types of fuel cells, such as phosphoric acid fuel cell (PAFC), polymer electrolyte fuel cell (PEFC) and solid oxide fuel cell (SOFC), have been developed and used in multiple applications. Among these fuel cells, the PEFC has many advantages in transportation applications. The PEFC can operate at relatively low temperature and achieve twice the energy effeiciency of the ICE with negligible polution [3, 4]. Therefore, the PEFC draws wide attentions as one of the leading candidates for future automotive power technology.

The main feature of PEFCs is a proton-conducting polymer electrolyte membrane separating the anode and cathode electrodes shown in Figure 1.1. On the anode, hydrogen gas is split into protons and electrons. While on the cathode, oxygen gas acquires the electrons

travelling through the external circuit and the protons penetrating the membrane to produce water. Both reactions are sluggish at room temperature that high performance catalysts have to be applied. So far, Pt-based catalysts are the most efficient and reliable. However, the high cost and scarcity of platinum retard the commercialization of PEFCs, especially the cathode Pt loading for ORR takes up the main consumption of Pt in PEFCs [5]. In order to reduce the Pt use in PEFCs, the mass efficiency of Pt has been pushed to the limit through creating Pt nanowires [6], Pt alloy nanocrystals [7], and even supported single-atom Pt [8, 9]. In the long run, the solution to cutting cost on catalysts in PEFCs still lies in the discovery of inexpensive substitutes for Pt.

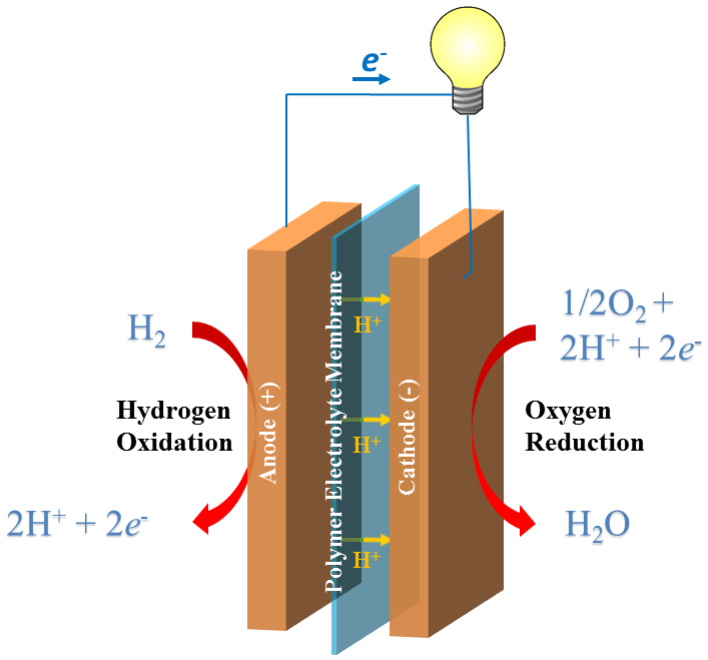

Figure 1.1: Scheme of H_2-O_2 polymer electrolyte fuel cell.

An alternative to Pt-based catalysts for PEFC cathode application is the non-precious metal-based catalyst (NPMC). The earlist NPMC is cobalt phthalocyanine discovered by Jasinski 1964 [10]. Since then, vatious transition metal macrocyclic complexes, such as metalloporphyrins and metallophthalocyanines, have been reported to have ORR activity

and extensively investigated [11–13]. The transition metal macrocyclic complexes typically consist of a center transition metal atom coordinated with four nitrogen ligands enclosed in a carbon macrocyclic skeleton. The catalytic activity of the macrocyclic complexes could be tuned by varying the type of central transition metal atom and peripheral functional groups [14]. However, the catalytic activity and stability of these molecular catalysts are inferior to that of Pt-based catalysts in acid electrolyte.

In recent years, non-precious transition metal/nitrogen doped carbon (TM-N-C) materials as novel ORR electrocatalysts emerge and become a new trend in NPMCs development [15–25]. It is widely reported that pyrolyzed TM-N-C materials could exhibit ORR activity comparable to that of Pt-based catalysts in acidic medium [18, 19, 22, 25], alkaline medium [19–21] and membrane electrode assembly [16–18]. These non-precious TM-N-C catalysts are typically synthesized by doping transition metal and nitrogen precursors into carbon materials (high specific area carbon, carbon nanotube and graphene) and subsequent heat treatment of the mixture at high temperature (700-900 °C) under inert gas and/or ammonia atmosphere [17]. The obtained TM-N-C catalysts exhibit not only high ORR activity, but also superb four-electron selectivity and good durability. It is speculated that some types of transition metal-nitrogen (TM-N_x) chelated structures form among the surface of carbon matrix during the heat treatment and the TM-N_x active sites play an important role in catalyzing ORR [16–19]. But the true nature of the active sites in the TM-N-C catalysts has not been fully revealed yet. It is of great significance to identify the active sites of TM-N-C catalysts and understand how they function in ORR catalysis through which the TM-N-C catalysts could be further improved.

As a complement to experimental study, computational simulation by first-principles based methods is an indispensable approach in heterogeneous catalyst design [26]. It proves that combining theory and experiment is extremely powerful in heterogeneous catalysts searching in many cases, such as ammonia synthesis [27], methanation reaction [28], and Pt-alloy catalysts for ORR [29]. More specifically, catalytic activities such as turnover frequency and selectivity can be measured through experiments, while energy parameters such as the adsorption energies and the activation energies in the catalytic process can be obtained by first-principles calculations. Hence the property correlations can be established and the

descriptor based approach can be used to screen new catalytic materials efficiently. Moreover, computational simulation can unravel the ORR mechanisms at atomic scale which help us gain fundamental understanding behind the heterogeneous catalysis.

In this thesis, both experimental and computational approaches have been applied to study ORR on the TM-N-C catalysts systematically. Pyrolyzed transition metal/nitrogen doped carbon nanofibers have been prepared as non-precious TM-N-C catalysts for ORR. The physical and chemical properties of the synthesized TM-N-C catalysts have been characterized by multiple techniques. Combined with experiments, the density functional theory calculation has been employed to investigate ORR mechanisms on different proposed active site models of the TM-N-C catalysts. Thermodynamic and kinetic analysis of the ORR process on the TM-N-C catalysts have been conducted. As a result, many discoveries in the TM-N-C catalysts have been made and scientific understanding on how the TM-N-C catalysts work for ORR has been advanced.

2.0 BACKGROUND

2.1 STATE-OF-THE-ART TM-N-C CATALYSTS

The TM-N_4 macrocyclic complex catalysts for ORR discovered at early time usually have a poor performance in acidic medium. One of the interesting phenomena observed in most studies is that the catalytic activity and stability of the TM-N_4 macrocyclic complexes can be highly enhanced through heat treatment on carbon substrate [30–32]. In 1989, Yeager *et al.* heat treated Co(II) or Fe(II) salts and polyacrylonitrile (PAN) with high-area carbon to produce a promising ORR catalysts in both alkaline and acidic medium [33]. Since then, the synthesis of TM-N-C catalysts from pyrolyzed transition metal/nitrogen doped carbon materials has entered a period of rapid development. A major breakthrough has been made in 2009 by Lefèvre *et al.* in which a volumetric activity of 99 $A \cdot cm^{-3}$ at 0.8 V in fuel cell tests (close to DOE 2010 target of 130 $A \cdot cm^{-3}$) was reported [17]. In this part, multiple methods to prepare and characterize the state-of-the-art TM-N-C catalysts and their performance are reviewed.

2.1.1 Preparation and performance

In the synthesis of TM-N-C catalysts, transition metal precursors and nitrogen precursors are necessary materials. Metal salts (such as acetates and chlorates) and TM-N_4 macrocyclic complexes (such as porphyrin and phthalocyanine) are usually used as metal precursors. Among them, TM-N_4 macrocyclic complexes serve as nitrogen precursors as well. Other nitrogen precursors include N-containing molecules (such as phenanthroline, polyaniline and polyacrylonitrile) and NH_3 gas. According to the type of metal and nitrogen re-

sources, the TM-N-C catalysts can be categorized in three types: TM-N-C derived from metal salts and NH_3 gas [17, 34–38], TM-N-C derived from metal salts and N-containing molecules [18, 39, 40], and TM-N-C derived from TM-N_4 macrocyclic complexes [41–43]. In some works, multiple nitrogen precursors (for example both N-containing molecules and NH_3 gas) are adopted [17, 43]. The precursor materials are mixed either by ball-milling or by wet impregnation. The mixtures are then pyrolyzed under inert gas or NH_3 atmosphere at temperature up to 1000 °C for hours in one time or multiple times. In some works, an acid washing procedure is applied to remove inactive metal species and other impurities before the last heat treatment step [18].

The catalytic activity of TM-N-C catalysts is optimized through varying the precursor materials and synthesis parameters involved in the procedures mentioned above. For example, Lefèvre *et al.* synthesized a series of iron-based catalysts using iron acetate as metal precursor under different temperature and duration of heat treatment in Ar or NH_3 atmosphere [36]. They found that the catalytic activity is highly correlated with the micropore area produced under different synthesis conditions. In their following work [17], a volumetric activity of 99 $A{\cdot}cm^{-2}$ was achieved by mixing high microporous carbon with phenanthroline (50 wt. %) and iron acetate (1 wt. % Fe), then heat treating the precursors in argon at 1050 °C for an hour and subsequently in NH_3 at 950 °C for five minutes. The addition of phenanthroline as micropore filler and the duration of the second heat treatment process in NH_3 has proven to be the key to reach such high catalytic activity.

Instead of NH_3 gas, N-containing polymers can also be used as nitrogen precursors for TM-N-C preparation. Polyacrylonitrile (PAN) and polyaniline (PANI) are two types of commonly used N-containing polymer precursors. For example, Los Alamos National Laboratory developed high performance TM-N-C catalysts from PANI, iron precursor ($FeCl_3$) and/or cobalt precursor ($Co(NO_3)_2{\cdot}6H_2O$) with high surface area carbon [18]. It was believed that the similarity between the structure of PANI and graphite is in favor of the incorporation of N-containing active sites into the partially graphitized carbon matrix. In this work, a two-step heat treatment procedure (one hour for the first step, three hour for the second step, and both in nitrogen gas) was adopted. The optimal temperature for heat treatment has been found to be 900 °C. It was also observed that the obtained catalyst derived from iron

shows a better activity than the catalyst derived from cobalt while the iron/cobalt co-doped sample exhibited the highest ORR activity close to Pt and long-term stability in the MEA test.

The catalytic activity of TM-N-C catalysts also depends on the type of carbon substrate used for synthesis. The microporous surface area greatly affects the active site density on the carbon support [36]. Moreover, it has been found that during the heat treatment in the NH_3 atmosphere, a high content of disordered carbon phase in the carbon matrix is required to facilitate the formation of active sites [44, 45]. Besides high surface area carbon, novel low dimensional carbon materials, such as carbon nanotube and graphene have also been applied as carbon supports in a few studies, showing improved ORR activity for TM-N-C catalysts [46–50]. It is worth noting that carbon substrate can alternatively produced during pyrolysis from precursor N-containing organic molecules or polymers with carbon skeleton. For example, Fe- and N-containing carbon nanofibers were synthesized from iron phthalocyanine (FePc) and PAN through electrospinning and pyrolysis for ORR catalysis recently [51, 52]. Electrospinning is a technology used to produce polymer nanofibers with controllable diameters and morphologies [53]. The as-spun nanofibers possess high surface area which makes them suitable as catalysts carriers. The FePc was directly doped into the PAN precursor solution for electrospinning and the as-spun FePc/PAN nanofibers were subsequently subjected to pyrolysis in N_2 atmosphere and converted to Fe- and N-containing carbon nanofibers during carbonization process [52]. The acquired Fe- and N-containing carbon nanofibers exhibited promising ORR activity in acidic electrolyte [52]. In this thesis, the electrospinning method has been employed to prepare TM-N-C samples due to its low cost and easy process.

It has also been recognized that TM-N-C catalysts exhibit higher activity for ORR in alkaline than in acid [54–56]. Dodelet *et al.* investigated the effect of pH value on the activity of FeNC catalysts and found that the activity of FeNC catalysts was 710 times higher at pH 13 than at pH 1 [54]. Due to the lack of the fundamental understanding on ORR active sites, these results on the electrolyte effect in TM-N-C catalysts have not been well understood.

2.1.2 Electrochemical characterization methods

To evaluate an ORR catalyst, there are several concerned properties including activity, selectivity and durability which can be charaterized through the electrochemical test or the fuel cell test. The catalytic activity is usually evaluated by the half wave potential or volumetric current density at 0.8 V on a polarization plot (U-I curve) measured through the electrochemical cell with three-electrode system or the fuel cell with membrane electrode assembly (MEA). Figure 2.1 shows the basic setup of an electrochemical cell which consists of a working electrode (WE), a counter electrode (CE), and a reference electrode (RE). The catalysts are applied on the WE and the ORR catalysis proceeds on this electrode during the test. The WE and the CE form a current circuit together. The RE which has a stable and well-known electrode potential works as a potential reference for the WE. The WE usually rotates to induce the electrolyte convection enhancing the mass transport of O_2 which is called rotating disk electrode (RDE) method. On the other hand, the MEA is an assembled stack of polymer electrolyte membrane, catalyst and flat plate electrode. The MEA is the core component of a fuel cell whose performance does not only depend on the catalyst performance. In this thesis, the electrochemical cell has been employed to characterize the electrochemical property of TM-N-C catalysts for ORR.

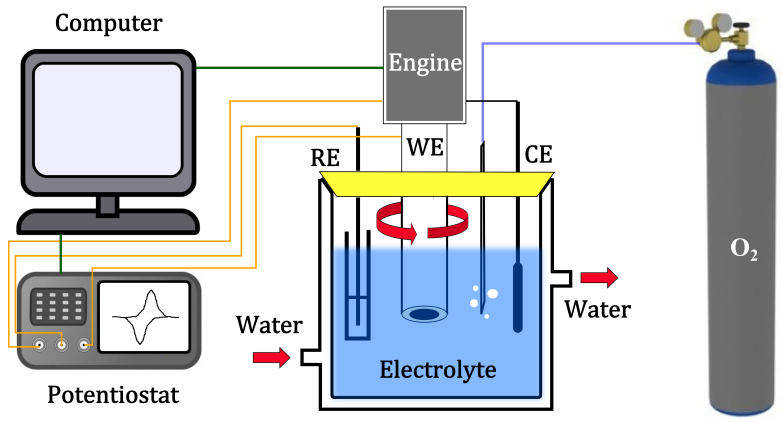

Figure 2.1: Scheme of the electrochemical cell with three-electrode system.

During the oxygen reduction to water, the oxygen may be alternatively reduced to hydrogen peroxide as an undesired byproduct which corrodes the membrane declining cell performance [57]. This side reaction involves only two electrons transfer ($2e^-$ pathway) per oxygen molecule instead of four electrons transfer ($4e^-$ pathway) per oxygen molecule to produce water. The $4e^-$ pathway is preferred for its high efficiency and free of hydrogen peroxide. The pathway selectivity can be determined either through the RDE method based on Koutecky-Levich equation or through rotating ring disk electrode (RRDE) method measuring hydrogen peroxide yield. The Koutecky-Levich equation [58] is

$$\frac{1}{J} = \frac{1}{J_k} + \frac{1}{0.62nFD_{\mathrm{O}}^{2/3}\nu^{-1/6}C_{\mathrm{O}}\omega^{1/2}} \tag{2.1}$$

in which J_k is kinetic current; n is electron transfer number; F is faraday constant; D_{O} is the diffusion coefficient of O_2; ν is the kinematic viscosity; C_{O} is the concentration of oxygen; ω is the electrode rotating speed in radian. The electron transfer number, which indicates the pathway selectivity, can be determined by measuring current density J under different electrode rotating speed ω. In the RRDE method, a second ring electrode wraps around the central disk electrode. During RRDE experiment, the ring is held at a sufficiently positive potential that any produced hydrogen peroxide reaching the ring is rapidly oxidized. Therefore, the hydrogen peroxide yield can be determined with the ring current and collection efficiency [58].

The stability of TM-N-C catalysts is usually studied by accelerated stress testing (AST) which is an approach used in durability tests of Pt-based catalysts [59, 60]. Basically, the test is performed through potential cycling in an RDE experiment or voltage cycling in a fuel cell. Alternatively, the long term stability test can be performed through examine the lifetime of a fuel cell held at a constant working voltage. In an AST test, the catalysts are completely exposed to the electrolyte and protons with high mobility in an acidic medium which accelerates the degradation of the catalysts.

2.1.3 Identification of catalytic active sites

Although the activity and durability of TM-N-C catalysts have been improved by several orders of magnitude recently, the chemical structures of the active sites are still unclear and under investigation. Many researchers proposed the isolated, planar TM-N_3 [61] and TM-N_4 [17, 62, 63] moieties embedded in a graphene layer to be the ORR active sites in pyrolyzed TM-N-C catalysts. Moreover, Holby *et al.* showed that a pair of adjacent TM-N_x sites could efficiently cleave the O-O bond during a $4e^-$ ORR using the first principles DFT calculations and thus suggested them as possible ORR active sites in pyrolyzed TM-N-C catalysts [64, 65]. However, it is a challenge to observe the appearance of the active site directly using electron microscopic techniques due to the non-crystalline structure of the pyrolyzed TM-N-C materials. Although the single iron site confined in a graphene matrix in TM-N-C materials has been revealed by high-resolution transmission electron microscopy (HR-TEM), high-angle annular dark-field scanning transmission electron microscopy (HAADF-STEM), and low-temperature scanning tunneling microscopy (LT-STM) in some works [66, 67], the widely conjectured FeN_4 composition and its function for ORR have not been confirmed.

On the other hand, specific spectroscopic techniques, including X-ray photoelectron spectroscopy (XPS), ^{57}Fe Mössbauer spectroscopy and X-ray absorption near edge structure (XANES), play an important role in revealing the nature of the active sites [63, 68–74]. XPS is a widely used surface analysis technique measuring the elemental composition and chemical state [69, 75]. ^{57}Fe Mössbauer spectroscopy is a powerful technique to identify iron species with different electronic states within materials [70, 73]. XANES is a highly sensitive technique to determine the chemical state of species even in very low concentration [63, 74]. In the pyrolyzed TM-N-C materials for ORR, various nitrogen functional groups and transition metal species exist. Some common nitrogen species include pyrrolic type, pyridinic type, quaternary type, nitrile and TM-N_x, while transition metal exists in these materials in forms of elementary particle, oxide, carbide, nitride, or TM-N_x [73, 74]. The relationship between the catalyst performance and its surface species can be established by comparing different samples synthesized under different conditions. For example, through multi-technique characterization and principal component analysis, Zelenay *et al.* found the activity of Fe-N-C

catalysts correlates well with Fe-N content, especially that of Fe in the porphyrazine and pyridinic coordination [73]. Moreover, many other studies also support that iron coordinated with nitrogen atoms (FeN_x) constitute the active site in Fe-N-C catalysts and several FeN_xC_y moieties have been proposed as active sites [71]. Recently, through quantitative analysis of the EXAFS and XANES regions on Fe-N-C catalysts, the porphyrin-like FeN_4-C_{12} moiety has been identified as the main active site responsible for ORR by Jaouen *et al.* [74] It was also shown that the highly basic N-groups formed during NH_3 pyrolysis can enhance the ORR activity of FeN_4-C_{12} active site [74].

2.2 COMPUTATIONAL SIMULATION OF ORR ON TM-N-C CATALYSTS

The Kohn-Sham density functional theory (DFT) [76, 77] calculation method is a powerful tool for directly calculating the energy and electronic structure of a many electrons system from the principles of quantum mechanics. With the rapid development of digital computers in the past few decades, the DFT calculation method becomes one of the most popular simulation methods in materials sciences owing to its relatively low computational costs and reasonable accuracy. DFT calculations have been employed for designing Pt-based ORR catalysts extensively [78] showing an indispensable role in searching new catalysts. There are several advantages of DFT calculations in the study of heterogeneous catalysis. First, DFT calculations can help find energetic or electronic descriptors of ORR activity and establish ORR catalytic activity trends on various catalytic surfaces. The *d*-band theory [79] developed by Nørskov proved to be effective in describing the activity trends on transition metal surface, such as Pt bimetallic alloy catalysts for ORR [29]. Second, DFT calculations can help screen possible active sites among different proposed models in pyrolyzed TM-N-C catalysts. Third, DFT calculations can help understand ORR mechanisms on catalytic sites. The reaction pathways and energetic parameters of ORR on Pt-based catalysts have been well understood [80] while only a few works have been done on TM-N-C catalysts. In this part, DFT studies of TM-N-C catalysts for ORR and related topics are reviewed.

2.2.1 DFT study of TM-N_4 macrocyclic complexes for ORR

The pyrolyzed TM-N-C catalysts are developed from TM-N_4 macrocyclic complexes which have well-defined molecule structures. Early experimental study found that the catalytic activity of TM-N_4 macrocyclic complexes is mainly correlated with the type of central transition metal and the peripheral functional group on the carbon skeleton [13]. Fe and Co usually exhibit better performance as the central transition metal atom than other candidates [12]. FeN_4 macrocyclic complexes mainly promote $4e^-$ pathway with O-O bond breaking to produce water while CoN_4 macrocyclic complexes mainly promote $2e^-$ pathway to yield hydrogen peroxide [81]. Moreover, the catalytic activity of TM-N_4 macrocyclic complexes can be tuned to some extent by adding different peripheral ligands onto the complexes [82].

The DFT calculations of ORR on various TM-N_4 macrocyclic complexes have been carried out by several research groups [83–88]. These studies mainly focused on metalloporphyrins and metallophthalocyanines including their derivatives consisting of a central transition metal atom chelated in a square planar N_4 macrocyclic molecule. Tsuda *et al.* conducted comparative study of O_2 dissociation on different metalloporphyrins (MnP, FeP, CoP, NiP) and found that O_2 dissociation has the lowest energy barrier on FeP [84]. The best performance of FeP was attributed to the large contribution of the d electrons of the Fe to the LUMO-HOMO level of the FeP and the stable Fe-O bond at the final state. Shi and Zhang performed DFT calculations on the O_2 adsorption on various iron and cobalt porphyrins and phthalocyanines [83]. The catalytic activity of the transition metal macrocyclic complexes was positively related with the ionization potential and the O_2 binding ability. The ORR pathways on FePc and CoPc were also investigated using DFT calculations. FeP and FePc were found to catalyze ORR through $4e^-$ pathway while CoP and CoPc though only $2e^-$ pathway, supporting most experimental observations. The difference was explained by the higher e_g orbital level of the FeP/FePc than that of the CoP/CoPc.

The ORR on TM-N_4 macrocyclic complexes starts with the O_2 adsorption on the central transition metal. Analysis by molecular orbital theory suggested that the O_2 molecule can interact with the central transition metal atom though end-on configurations or side-on

configurations [89, 90]. The most stable configuration could be determined by locating the configuration with the lowest adsorption energy through DFT calculations. Systematic studies of ORR on various iron and cobalt porphyrins and phthalocyanines have been conducted by Wang *et al.* [86] The adsorption configurations and energies of ORR species O_2, H_2O, OH, and H_2O_2 on the porphyrins, tetraphenylporphyrins, phthalocyanines, fluorinated phthalocyanines, and chlorinated phthalocyanines were determined through DFT calculations. From the DFT calculations, a linear relation between the adsorption energy of OH or H_2O_2 and the adsorption energy of O_2 on the studied macrocyclic TM-N_4 complexes has been established.

2.2.2 DFT study of TM-N-C catalysts for ORR

DFT calculations complement experiments in the study of TM-N-C catalysts for ORR in two aspects. One is to screen possible active sites among so many different chemical structures in pyrolyzed TM-N-C catalysts [64, 91, 92], the other is to understand how ORR proceeds on the active sites [93]. In the former aspect, Holby *et al.* used DFT and metropolis Monte Carlo method to search for active site candidates [64, 91]. It was found that N-coordinated Fe defects tend to form at graphene edges [64, 94]. Among different FeN_x sites, the FeN_4 and FeN_3 sites are most stable that thet may coexist in the FeNC catalysts, while the FeN_2 sites are thermodymically unstable [64]. Moreover, the FeN_3 sites favor sitting with each other to form clustered structures (Fe_2N_5) which can cleave the O_2 bond without activation energy barrier [64]. The FeN_4 sites can form in different local carbon structures either embedded in or bridged edges of graphene [74]. Figure 2.2 shows multiple proposed FeN_4-C_x moieties as active sites. FeN_4-C_{10} moiety has a structure of FeN_4 embedded in intact graphene. FeN_4-C_{12} moiety has a porphyrin-like architechture bridging two zig-zag edges of graphene. FeN_4C-$_8$ moiety has a structure of FeN_4 bridging two armchair-like edges of graphene.

Rossmeisl *et al.* conducted a comparative study on TM-N_4-C_{10} and TM-N_4-C_{12} with different central transition metals [95]. They found a scaling relation between the free energies of adsorbed $*$OOH and $*$OH intermediates by 3.15 eV which is known on (111) and (100) surfaces of transition metals and their alloys. The volcano plot of the ORR activity

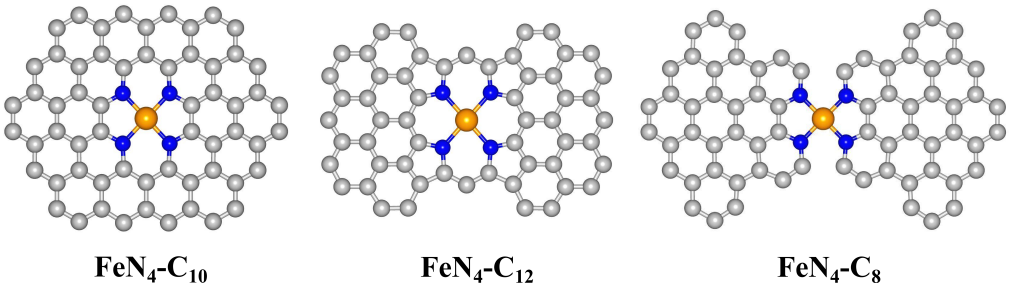

Figure 2.2: Various proposed FeN_4-C_x moieties as active sites for ORR.

vs. free energy of adsorbed OH resulting from the DFT calculations (similar to that on transition metals surface) was shown. It concluded that graphitic materials with active sites composed of the porphyrin-like moiety and transition metals belonging to groups 7 to 9 in the periodic table are active towards ORR. And the activity performance can be improved by finding the active sites which can stabilize the adsorption energy of $*$OOH with respect to that of $*$OH. Kattel *et al.* have done a series of studies on TM-N_x (TM = Fe, Co, Ni, x = 2, 4) embedded in graphene models [96–98]. It was found that TM-N_4 (TM = Fe, Co) moieties are energetically favorable as compared to TM-N_2 (TM = Fe, Co) moieties and they are probably the active sites in the catalysts [96, 98]. In contrast, O_2 and H_2O interact very weakly with NiN_x sites indicating that these NiN_x sites are unlikely catalytic sites for ORR [97]. On the other hand, TM-N_4 (TM = Fe, Co, Ni) clusters bridging the zig-zag edges of graphitic pores were studied [99]. The results implied that the TM-N_4 clusters preferably form to connect the edges of two graphene pieces. And it was proposed that the ORR would proceed on the FeN_4 and CoN_4 clusters through a $4e^-$ pathway with the O-O bond breaking during the interaction of intermediate HOOH with the FeN_4 and CoN_4 sites [99].

In the other aspect, the ORR mechanisms on TM-N_4 embedded in graphene models have been investigated by DFT calculations in several works [93, 100, 101]. Generally there are $4e^-$ pathway producing water and $2e^-$ pathway producing hydrogen peroxide for ORR. Along $4e^-$ pathway, three mechanisms were proposed including the dissociative mechanism (via O_2 dissociation), the associative mechanism (via OOH dissociation) and the mechanism involving O-O bond breaking via HOOH dissociation. Orellana studied O_2 dissociation on

the metal center of TM-N_4 (TM = Mn, Fe, Co) embedded in graphene models and located minimum energy paths as well as saddle points [100]. The activation energy of O_2 dissociation was found to be 0.7 eV on Mn-N_4 center, 1.1 eV on Fe-N_4 center and 1.6 eV on Co-N_4 center. On the other hand, the OOH dissociation pathway (shown in Figure 2.3) on Fe-N_4 embedded in graphene model was studied by Zhang *et al.* [101] The results showed that the rate-determining step (RDS) appears at the initial reduction step, adsorbed O_2 protonated to adsorbed OOH, with an activation energy of 0.62 eV. And the $4e^-$ reduction of O_2 into H_2O is kinetically preferred to the $2e^-$ pathway toward H_2O_2. A systematic mechanism study including all three pathways for ORR on FeN_4 embedded in graphene has been conducted by Kattel *et al.* recently [93]. Among all three mechanisms, the OOH dissociation pathway is identified as the kinetically most favorable one with an activation energy of 0.56 eV at RDS (OOH dissociation).

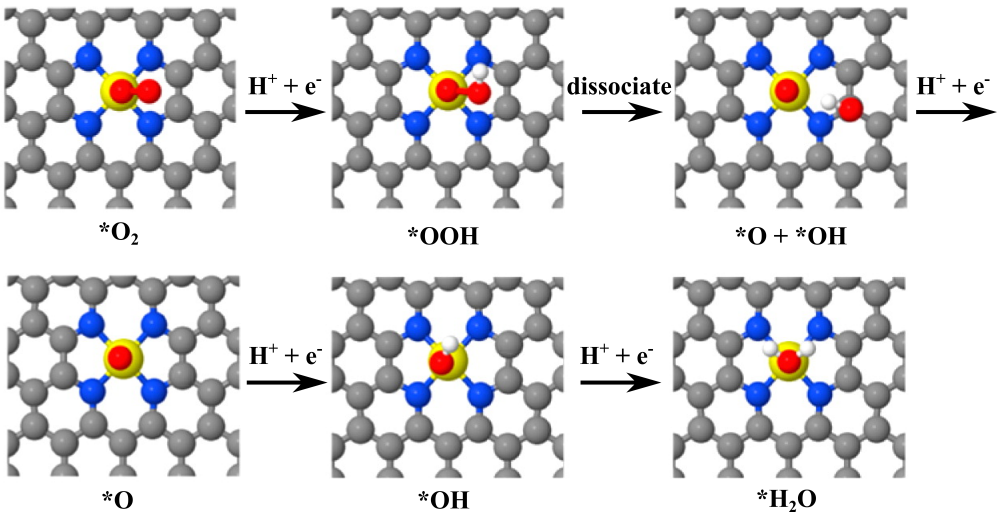

Figure 2.3: Atomic structures of ORR intermediates through the OOH dissociation pathway. The gray, blue, yellow, red, and white balls represent C, N, Fe, O, and H atoms, respectively.

2.2.3 Kinetic analysis by microkinetic model

Through DFT calculation, the energetic parameters such as the adsorption energies of ORR species and the activation energies of ORR elementary steps can be obtained. But the calculated energetic parameter cannot be compared with experiment-measured voltammograms directly. The microkinetic model using the energetic parameters from density functional theory calculations to predict the total reaction rate is a powerful tool to bridge the computational simulations and the experimental results. Specifically, a microkinetic model includes sequences of elementary steps, such as adsorption, desorption, and surface reactions constituting the complete reaction mechanism. The reaction rate of each elementary step can be derived from pre-factors, activation energies and concentration of reactant species. Hence a series of ordinary differential equations (ODEs) describing the time variation of each reaction intermediate concentration can be built from the reaction rates of elementary reactions. The total reaction rate, i.e. the polarization curve for ORR, can be predicted by solving these equations numerically under different reaction conditions.

Several microkinetic model based analysis of ORR on Pt surfaces has been reported [102, 103]. For example, Qi *et al.* developed an ORR microkinetic model based on DFT calculations which considers both the competitions of surface sites/adsorbates and the lateral attraction/repulsion between different ORR intermediates based on the mean-field approximation on Pt (111) and (100) surfaces [103]. Sensitivity analysis of ORR rate to individual energetic parameter was performed. It was found that the adsorbate interactions flatten the catalytic activity *vs.* adsorption strength volcano plot, indicating that variation of the energetic parameter (exponential factor to reaction rate) around the optimal peak of the plot would not change the catalytic activity a lot. This result agreed with observed experimental sensitivity behavior. In a more recent work [102], Hansen *et al.* reproduced an experimental polarization curve on Pt (111) surface by microkinetic model. They also demonstrated the existence of a kinetic activity volcano with close connection to the thermodynamic activity volcano. The unifying thermodynamic and kinetic analysis predicted an activity optimum when the OH binding is 0.1 eV weaker than that on Pt (111) surface. In contrast, there has been no microkinetic model based analysis for ORR on TM-N-C catalysts reported so far.

The above literatures suggest that the microkinetic model would be a powerful approach to the ORR study on TM-N-C catalysts.

3.0 HYPOTHESES

In this thesis, the following hypotheses are put forward:

1. *The TM-N-C catalysts could be synthesized by pyrolysis of transition metal/nitrogen doped polyacrylonitrile (PAN) nanofibers.* The carbon nanofibers are mainly produced by pyrolysis of PAN nanofibers in industry [104, 105]. It is speculated that the ORR active sites could be created during the pyrolysis by doping appropriate transition metal and nitrogen precursors into the PAN nanofibers [106, 107]. The catalytic activity would be determined by the type of precursors, the doping quantity and the pyrolysis process. The most widely used transtion metal doping is iron and FeNC is known to catalyze ORR through $4e^-$ pathway [18]. The doping quantity would be important in the catalyst preparation. It was reported that the ORR activity increases as the iron content increases from 0.5 wt% to 3 wt%, but excessive addition of iron only leads to the formation of oxide impurities instead of creating more active sites [108].
2. *The active sites in TM-N-C catalysts would have a TM-N_4 center.* Acoording to the literature review in Section 2.2.2, TM-N_4 sites were found to be the most stable sites among TM-N_x sites [64, 96] and the most widely studied sites.
3. *The binding strength of ORR species is correlated with the electronic structure of the TM-N_4 active site.* According to the *d*-band theory developed by Nørskov [109], the binding strength of an adsorbate on a metal surface depends on the local electronic structure of the surface, i.e. the *d*-band center positon with respect to the Fermi level. A similar correlation probably exists in the TM-N-C catalysts where different central transition metals have different *d*-orbital occupations and the local carbon structure tunes the energy level of *d*-orbital as well.

4. *The ORR pathway selectivity depends on the activation energy for oxygen-oxygen bond breaking.* The $4e^-$ pathway generating water involves oxygen-oxygen bond breaking while the $2e^-$ pathway doesn't. If the energy barrier for oxygen bond scission is too high to overcome, the $2e^-$ pathway is adopted alternatively.
5. *The type of central transition metal mainly determines the activity and selectivity of TM-N-C catalysts.* Each transition metal has its distinct *d*-electron number which directly determines the local orbital occupation influencing the spin state of the active site, the chemical bond between the adsorbate and the active site, and thus the binding strength. The Sabatier principle suggests that a moderate interaction between the reaction species and the catalyst is optimal. If the interation is too weak, the catalyst cannot bind the reactants. If the interation is too strong, the products cannot take off from the catalyst surface. Concequently, the central transition metal plays the primary role in the activity and selectivity of TM-N-C catalysts.
6. *The local carbon structures around the active sites affect the activity and selectivity of TM-N-C catalysts.* According to the experimental characterization, the TM-N_4 center can be embedded in the carbon matrix with various chemical structures shown in figure 2.2. The local carbon structure may affect the electronic structure of the TM-N_4 center thus tuning the catalytic activity and selectivity of TM-N-C catalysts.

4.0 OBJECTIVES

The aim of this thesis is to test the proposed hypotheses in section 3 through systematic experimental and computational studies on the TM-N-C catalysts. Specifically, there are the following objectives:

1. Develop an effective process to synthesize TM-N-C catalysts; Then characterize the physical properties, catalyic activity, and selectivity of the synthesized catalysts.
2. Find the adsorption configurations of ORR species and calculate the adsorption energies on the TM-N_4 active site; Analyze the electronic structures of the TM-N_4 centers; Establish a correlation between the binding strength and the electronic structure.
3. Calculate the free energy of each ORR intermediate and plot the free energy profile along the ORR reaction coordinates for thermodynamic analysis.
4. Calculate the activation energies of elementary reactions involving spliting oxygen-oxygen bond; Analyze the catalytic activity and selectivity of TM-N_4 active sites with various transtion metal and local carbon structures.
5. Develop microkinetic model to predict polarization curves of ORR on different TM-N_4 active sites based upon calculated energy parameters; Compare the computational prediction with the experimental observation.

5.0 EXPERIMENTAL AND COMPUTATIONAL METHODS

5.1 EXPERIMENTAL APPROACHES

5.1.1 Synthesis of TM-N-C catalysts

TM-N-C catalysts were synthesized by electrospinning method and subsequent pyrolysis. Electrospinning draws very fine fibers from a polymer solution or a molten polymer by static electrical field. The basic setup for electrospinning consists of a nozzle connected to a high-voltage DC power supply, a syringe pump, and a grounded collector. The applied high voltage induces the formation of a liquid jet from the tip of the nozzle. As the charged jet is stretched by electrical field force and dried by solvent evaporation, ultra-fine polymer fibers are deposited on the opposite grounded collector. Synthesis procedures of non-precious TM-N-C catalysts are schematically depicted in Figure 5.1. Specifically, Fe and Co were chosen as two types of transition metal precursors in this comparative study. The procedures for synthesizing FeNC and CoNC catalysts are described below.

Polyacrylonitrile (PAN, M_w = 150,000 g·mol^{-1}, Sigma Aldrich) was dissolved in N,N-dimethylformamide (Sigma Aldrich) by stirring at 70 $\sim$ 80 °C for 10 hours to acquire solutions containing 10 wt.% PAN or 8 wt.% PAN respectively. The homogeneous precursor solutions were attained by mixing iron (II) phthalocyanine (FePc, $\sim$ 90 % dye content, Sigma Aldrich) with the 10 wt. % PAN solution while cobalt (II) phthalocyanine (CoPc, β-form, 97 % dye content, Sigma Aldrich) with the 8 wt. % PAN solution after stirring for 18 hours at 70 $\sim$ 80 °C. Thus, the precursor solutions contained the same molar content of FePc and CoPc. During nanofiber fabrication, the PAN solutions containing FePc and CoPc were injected

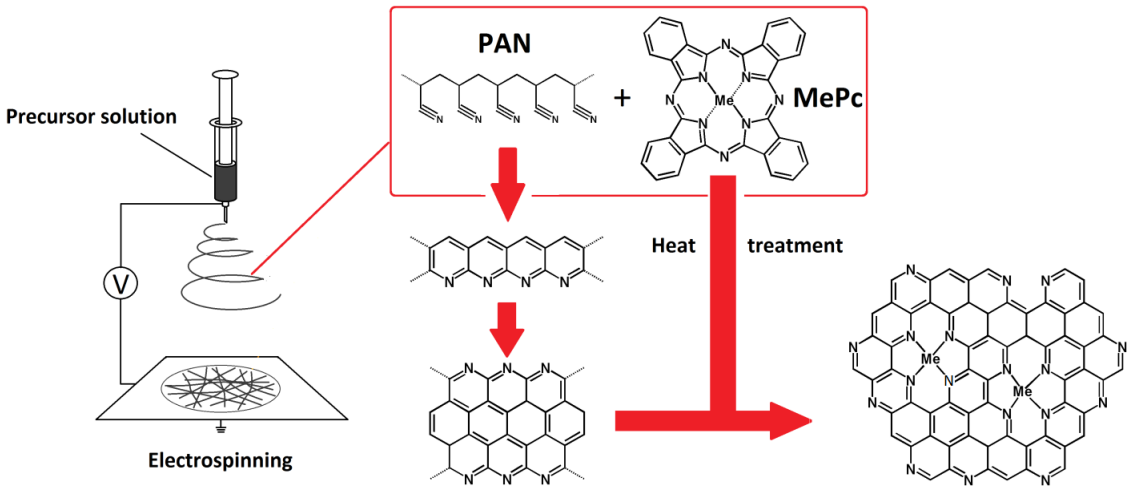

Figure 5.1: Scheme of the synthesis procedure of non-precious TM-N-C catalysts.

to a collector plate through a syringe connecting with a stainless steel nozzle at a flow rate of 1.0 mL/h and 0.8 mL/h, respectively. The distance between the nozzle and collector plate was fixed at 15 cm. The applied voltage was set to be 25 kV. Pyrolysis: The as-spun nanofibers were further pyrolyzed in a quartz tube furnace. The pyrolysis processing included pre-oxidation process in dry air at 250 °C for 2 hours and carbonization processes in N_2 atmosphere at 900 °C for 4 hours. The furnace was ramped up at 5 °C/min to target temperatures and then cooled to room temperature at each heat-treatment process.

5.1.2 Materials characterization

The morphology, surface area and surface chemical composition of prepared FeNC and CoNC catalysts were characterized by multiple techniques. A Philips XL-30 field emission gun scanning electron microscope (FEG SEM) was used for photography of as-spun nanofibers and pyrolyzed nanofibers (resolution 3.0 nm at 10.0 kV). An ASAP 2020 Physisorption Analyzer (Micromeritics Instrument) was used to measure nitrogen absorption curves, through which the specific area of each sample was calculated by the Brunauer-Emmett-Teller (BET) theory. An ESCALAB 250 XI with Al K_α line (1486.6 eV) as the X-ray source (Thermo

Scientific^{TM}) was used to collect X-ray photoelectron spectroscopy (XPS) spectra for each nanofiber sample. Thermo Scientific^{TM} Avantage Software was used to analyze the XPS survey and narrow scans.

5.1.3 Electrochemical measurements

Electrochemical measurements were performed using a bipotentiostat with a rotating ring-disk electrode system (WD20-RRDE, Pine instruments). In the setup, a rotating ring-disk electrode (Pine instrument) with a glassy carbon (GC) disk (0.196 cm^2) and Pt ring (0.11 cm^2) was used as working electrode, a coil platinum electrode as counter electrode, and a silver chloride electrode (Ag/AgCl/4 mol/kg KCl, 0.202 V *vs.* RHE) as reference electrode. The working electrode was prepared as follows: first, the GC disk and Pt ring were polished by 0.3 m alumina on a nylon cloth and subsequently by 0.05 m alumina on a microcloth; then, the GC disk and Pt ring were rinsed with deionized (DI) water, sonicated in DI water three times, and dried in N2 flow; and further the synthesized catalyst inks (20 L) were deposited on the GC disk. In catalyst ink preparation, the fabricated FeNC and CoNC catalysts were first ground into powder using mortar and pestle and mixed with pure ethanol and Nafion ethanol solution (5 wt. %). The acquired mixture had a concentration of 10 mg/mL catalyst and 1.5 mg/mL Nafion. The mixture was further homogenized through sonication for 30 mins and then deposited onto the GC disk, yielding a loading of 1 mg/cm^2 catalyst and 150 μg/cm^2 Nafion.

The RDE and RRDE measurements were performed in 0.5 M H_2SO_4 and 0.1 M KOH electrolytes separately at room temperature. Before data collection, the electrolyte was purged with either N_2 or O_2 gas for 30 mins. Before each cyclic voltammogram measurement, the GC disk (loaded with catalysts) and Pt ring were respectively activated by 20 cycles of rotating disk cyclic voltammetry from 1.23 to 0 V with a scan rate of 50 mV/s. Linear sweep voltammograms were recorded from 1.23 to 0 V with a scan rate of 5 mV/s at different rotating speed (100, 400, 900, 1600 rpm) in O_2-saturated electrolyte. The oxygen reduction current is determined by subtracting a background current (obtained from the measurements in N_2-saturated electrolyte) from the current measured in O_2-saturated electrolyte. The

electron transfer number per O_2 at a specific electrode potential can be acquired by linear regression of $1/J_k$ (inverse of kinetic current density) with respect to $\omega^{-1/2}$ (inverse of square root of electrode rotating speed) according to Equation 2.1. The H_2O_2 yield can be calculated by

$$H_2O_2\% = \frac{2I_{ring}}{N \times I_{disk} + I_{ring}} \times 100\% \tag{5.1}$$

in which I_{ring} and I_{disk} are the ring and disk current in the RRDE measurement, and N is collection efficiency. The disk current is obtained in the same way described above and the ring current is obtained by holding the ring electrode potential at 1.2 V during RRDE measurement. The collection efficiency (N) of the RRDE electrode is only determined by the electrode geometry. The value can be measured through ferricyanide/ferrocyanide redox reaction in which ferricyanide is reduced to ferrocyanide at the disk electrode (I'_{disk}) and generated ferrocyanide is partially oxidized back to ferricyanide at the ring electrode (I'_{ring}). The collection efficiency (N) is calculated by

$$N = -\frac{I'_{ring}}{I'_{disk}} \tag{5.2}$$

5.2 COMPUTATIONAL APPROACHES

5.2.1 Density functional theory calculation

Kohn-Sham DFT is a quantum mechanical modelling method to investigate the electronic structure of many-body systems. Kohn *et al.* prove that the ground-state wavefunction is uniquely determined by the ground-state electron density, *i.e.* the Kohn-Sham equations,

$$\left\{ -\frac{\hbar^2}{2m}\nabla^2 + V_{\text{ext}}(\vec{r}) + e^2 \int \frac{n(\vec{r}')}{|\vec{r} - \vec{r}'|} d\vec{r}' + V_{\text{xc}}[n(\vec{r})] \right\} \psi_i(\vec{r}) = \varepsilon_i \psi_i(\vec{r}) \tag{5.3}$$

with

$$n(\vec{r}) = \sum_i |\psi_i(\vec{r})|^2 \tag{5.4}$$

in which $\frac{\hbar^2}{2m}\nabla^2$ is the kinetic energy term; $V_{\text{ext}}(\vec{r})$ is the external potential, *i.e.* Coulomb potential between nuclei and electrons; $e^2 \int \frac{n(\vec{r'})}{|\vec{r}-\vec{r'}|} d\vec{r'}$ is Hartree potential which describes the interaction between electrons; $V_{\text{xc}}[n(\vec{r})]$ is the exchange-correlation potential; $\psi_i(\vec{r})$ is the effective single-electron wavefunction of the i-th electron; $n(\vec{r})$ is the electron density.

The external potential term is practically treated as the interaction between the ionic core (*i.e.* the nucleus with the frozen core electrons) and valence electrons instead of the interaction between the nucleus and all electrons. The pre-calculated potential of the effective ionic core is called a pseudopotential. Under the pseudopotential approximation, the eigenvalues of the system and the wavefunction beyond a threshold radius r_c are retained. There are three types of commonly used pseudopotentials, *i.e.* norm-conserving pseudopotentials (NCPP) [110, 111], ultra-soft pseudopotentials (USPP) [112–114] and projector augmented wave (PAW) potentials [115, 116]. USPP are the fastest while PAW potentials are the most accurate so that a suitable pseudopotential needs to be chosen to balance the efficiency and the accuracy.

The exchange-correlation potential term accounts for the energy difference between the exact ground-state energy and the energy calculated in a Hartree approximation and using the non-interacting kinetic energy. The actual form of this term is unknown, thus approximate functionals based upon the electron density must be introduced. The simplest approximation is the local density approximation (LDA) [117] which assumes that the exchange-correlation energy at a point $\vec{r}$ is equal to the exchange-correlation energy of a uniform electron gas that has the same density at the point $\vec{r}$. Consequently, the exchange functional is

$$E_X^{LDA}[n] = -\frac{3}{4}\left(\frac{3}{\pi}\right)^{\frac{1}{3}} \int n(\vec{r}^{\frac{4}{3}}) d\vec{r} \tag{5.5}$$

and the correlation functional is parameterized from quantum Monte Carlo simulations [118]. Furthermore, the generalised gradient approximation (GGA) attempts to incorporate the effects of inhomogeneities by including the gradient of the electron density. There are different proposed forms of GGA functional such as Becke-Lee-Yang-Parr (BLYP) [119, 120], Perdew-Wang 1991 (PW91) [121] and Perdew-Burke-Ernzerhof (PBE) [122]. It also needs to choose an appropriate exchange-correlation functional according to the simulation task.

The Hamiltonian of the Kohn-Sham equation (5.3) contains the unknown electron density to be determined, therefore the equation must be solved in a self-consistent manner. Specifically, the solution starts from stochastic wavefunctions $\psi_i^0(\vec{r})$ which can be expanded by a set of orthogonal bases with cut-off at $\phi_N(\vec{r})$ for a numerical solution

$$\psi_i^0(\vec{r}) = \sum_{j=1}^{N} C_j \phi_j(\vec{r}) \tag{5.6}$$

Then the wavefunctions are used to construct electron density $n^0(\vec{r})$ by equation 5.4, thus the initial Hamiltonian $H[n^0]$ is acquired. Subsequently, equation 5.3 with the initial Hamiltonian is solved iteratively through updating a guessed solution Ψ_1 by

$$\Psi_{n+1} = \Psi_n + \alpha(H\Psi_n - \varepsilon\Psi_n) \tag{5.7}$$

until convergence is achieved. After the solution for each band is obtained, a new electron density can be constructed. We repeat this process to get a self-consistent solution to the Kohn-Sham equation.

In this thesis, the spin-unrestricted DFT calculations for TM-N_4 macrocyclic complex molecules were performed using the DMol^3 module [123] of *Material Studio* from Accelrys (*Materials Studio* 6.0, DMol^3, Accelrys, San Diego, CA). The generalized gradient approximation (GGA) based on the Perdew-Wang formalism [124] was used to describe exchange and correlation. The double numeric basis with polarization (DNP) functions was chosen as the atomic basis set. Density functional semicore pseudopotentials were employed in our calculations. The energy convergence was set to be 1×10^{-5} eV for geometry optimization. The smearing was set to be 0.005 Ha, allowing electrons to be smeared out among all orbitals within a 0.005 Ha range of the Fermi level. On the other hand, the spin-polarized DFT calculations for TM-N_4 in carbon matrix were performed under periodic conditions using Vienna Ab-Initio Simulation Package (VASP) code. [125, 126] Projector augmented wave (PAW) potentials [115, 116] was used to describe the core electrons and a plane wave basis set with a kinetic energy cutoff of 400 eV was used to expand the wave functions. Electronic exchange and correlation are described within the framework of generalized gradient approximation (GGA) of Perdew, Burke and Ernzernhof (PBE) functional. [122] The Brillouin zone was

sampled using a Monkhorst-pack [127] $4\times4\times1$ k-point grid for active site FeN_4-C_{10}, $3\times3\times1$ for FeN_4-C_{12} and $4\times3\times1$ for FeN_4-C_8 (Figure 2.2). The atomic positions were optimized until the forces were below 0.02 eV/Å during structural optimization. The transition state of chemical reactions was located using the climbing image nudged elastic band (CI-NEB) method [128] with a convergence of 0.05 eV/Å for the force components both along and perpendicular to the tangent of the reaction path. Zero-point energy (ZPE) corrections were included in all the reported energies. ZPE corrections were calculated as

$$\mathrm{ZPE} = \sum_i \frac{1}{2} h\nu_i \tag{5.8}$$

where h is Plancks constant and ν_i is the frequency of the ith vibrational mode of binding molecules calculated by harmonic approximation.

5.2.2 Formation energy, adsorption energy, and free energy

The formation free energy of TM-N_4 active site was calculated by

$$\Delta G = E_{\mathrm{TM-N_4}} + x\mu_{\mathrm{C}} - E_{\mathrm{matrix}} - 4\mu_{\mathrm{N}} - \mu_{\mathrm{TM}} \tag{5.9}$$

in which, $E_{\mathrm{TM-N_4}}$ is the calculated total energy of TM-N_4 active site; E_{matrix} is the calculated total energy of corresponding carbon matrix before the TM-N_4 active site is embedded; μ_{C}, μ_{N}, and μ_{TM} are the chemical potentials of carbon, nitrogen, and transition metal respectively. The reference states are chosen to be perfect graphene for carbon, N_2 or NH_3 gas for nitrogen, and isolated atom in vacuum for transition metal. The chemical potentials for N_2 and NH_3 were calculated by the sum of electronic energy, ZPE, and entropy. The entropies of N_2 and NH_3 are obtained from chemistry handbook [129].

The adsorption energy of ORR species (denoted as A) on TM-N_4 active site was calculated by

$$E_{\mathrm{ad}} = E_{\mathrm{A-TM-N_4}} - E_{\mathrm{TM-N_4}} - E_{\mathrm{A}} \tag{5.10}$$

in which, E_{ad} is the adsorption energy; $E_{\mathrm{A-TM-N_4}}$ is the total energy of ORR species A adsorbed on the TM-N_4 active site; $E_{\mathrm{TM-N_4}}$ and E_{A} are the energy of TM-N_4 active site and species A respectively. The value of adsorption energy is usually negative. Lower

adsorption energy indicates stronger interaction between the adsorbate and the active site. On each TM-N_4 active site, the ORR species are considered to be only adsorbed on the top of central transition metal. The most stable adsorption configuration with the lowest adsorption energy is identified by comparing adsorption energies of different possible configurations. The examined adsorption configurations along those high symmetric directions are listed in Appendix A.

The free energy of each ORR intermediate was calculated using the computational hydrogen electrode method developed earlier by Nørskov *et al.* [130] Specifically, the free energy of $H^+ + e^-$ at standard state can be indirectly calculated by the free energy of $\frac{1}{2}H_2$ in gas phase at standard state according to the definition of reversible hydrogen electrode,

$$G(\mathrm{H}^+) + G(e^-) = G(\frac{1}{2}\mathrm{H}_{2(g)}), \mathrm{pH} = 0 \tag{5.11}$$

thus the free energy of ORR intermediate A (A = *OOH, *O, and *OH) in acid at pH = 0 can be calculated by

$$\Delta G_{\mathrm{ad}} = E_{\mathrm{A-TM-N_4}} - E_{\mathrm{TM-N_4}} + xG(\mathrm{H}_{2(g)}) + (-e)U_{vs.\mathrm{RHE}} - yG(\mathrm{H_2O}_{(aq)}) \tag{5.12}$$

in which $E_{\mathrm{A-TM-N_4}}$ includes electronic energy and ZPE; $G(\mathrm{H}_{2(g)})$ is the free energy of H_2 in gas phase at standard state; $G(\mathrm{H_2O}_{(aq)})$ is the free energy of H_2O in aqueous phase at standard state; e is the elementary charge; $U_{vs.\mathrm{RHE}}$ is the electrode potential with respect to the reversible hydrogen electrode; x and y are the coefficient balancing the chemical equation. The free energies of H_2 and H_2O were calculated by the sum of DFT calculated electronic energy, ZPE, and the entropy terms from Ref. [129, 130]. The free energy of $O_2(g)$ is calculated by the ORR thermodynamic potential which is 4.92 eV higher than $H_2O_(aq)$ at 0 V (*vs.* RHE).

5.2.3 Microkinetic model

The microkinetic model was employed to predict the polarization curves of ORR on TM-N_4 active sites based upon DFT calculated energy parameters. All the elementary reaction steps and rate equations are listed in Appendix B. Since the TM-N_4 active sites are isolated from each other, it was assumed no interaction between reactions on different active sites. The forward reaction rate constant was calculated by Arrhenius equation:

$$k_+ = Ae^{-\frac{E_a}{k_B T}} \tag{5.13}$$

in which A is the pre-exponential factor; E_a is the activation energy; k_B is the Boltzmann constant; and T is the temperature. The activation energies for O-O bond scission reactions (B.6, B.8, B.11) were calculated by DFT. The potential-dependent activation energies for proton-coupled electron transfer reactions (B.3, B.4, B.5, B.7, B.9, B.10) were calculated by

$$E_a(U) = E_a(U_0) + \beta e(U - U_0) \tag{5.14}$$

in which U is the electrode potential; U_0 is the reversible potential at which $\Delta G(U_0) = 0$; β is the symmetric factor; e is the elementary charge. $E_a(U_0)$ and β were assumed to be independent of reactions, so that values of 0.26 eV and 0.5 were adopted from ref [102, 131]. The pre-exponential factors were evaluated by the values for ORR on Pt surface [102], thus the Pt microkinetic simulation result could be used as a benchmark. The backward reaction rate constant was given by

$$k_- = \frac{k_+}{K} \tag{5.15}$$

where K is the equilibrium constant given by

$$K = e^{-\frac{\Delta G(U)}{k_B T}} \tag{5.16}$$

The O_2 diffusion flux from bulk electrolyte to double layer (B.1) could be estimated by linear approximation of Fick's first law [102]:

$$J_{O_2} = D_{O_2} A c_{H_2O} \frac{x_{O_{2(aq)}} - x_{O_{2(dl)}}}{2\delta} \tag{5.17}$$

in which D_{O_2} is diffusion coefficient; A is the cross-sectional area of two water molecules; c_{H_2O} is the mole concentration of water molecules; δ is the diffusion layer thickness. In the RDE method, the diffusion layer thickness is given by [58]

$$\delta = 1.61 D_{O_2}^{\frac{1}{3}} \nu^{\frac{1}{6}} \omega^{-\frac{1}{2}} \tag{5.18}$$

in which ν is the kinematic viscosity of electrolyte; ω is the rotating speed of electrode. Therefore, the rate constant in B.1 has the expression of

$$k_{1+} = k_{1-} = \frac{D_{O_2} A c_{H_2O}}{2\delta} \tag{5.19}$$

After the rate equations (Appendix B) were numerically solved at steady state, the current density was calculated by

$$j = e\sigma \mathrm{TOF}_{e^-} \tag{5.20}$$

in which σ is the surface catalytic site density; TOF_{e^-} is the turnover frequency of electrons which was calculated by

$$\mathrm{TOF}_{e^-} = r_3 + r_4 + r_5 + r_7 + r_9 + r_{10} \tag{5.21}$$

6.0 RESULTS AND DISCUSSIONS: EXPERIMENTAL PART

6.1 PHYSICAL AND CHEMICAL CHARACTERIZATIONS

6.1.1 SEM images of TM-N-C nanofibers

In this thesis, the CoNC and FeNC nanofiber catalysts were fabricated using the electrospinning and subsequent heat-treatment procedure described in Section 5.1.1. The morphologies of nanofiber catalysts were determined by analysis of SEM images. Figure 6.1 shows the SEM images of the as-spun (*i.e.*, before pyrolysis) CoPc/PAN and FePc/PAN fibers and the pyrolyzed CoNC and FeNC fibers. As seen from viewing these images, all the nanofibers have formed three-dimensional woven network structures. Compared to those of the as-spun fibers, the pyrolyzed fibers have network structures with more crosslinking (Figure 6.1b) and segmentation (Figure 6.1d). It was determined from these SEM images that the average diameter of the as-spun CoPc/PAN and FePc/PAN fibers were 349±79 nm (Figure 6.1a) and 389±50 nm (Figure 6.1c), respectively. Moreover, the average diameters of the pyrolyzed CoNC and FeNC fibers were measured to be 374±196 nm and 444±71 nm respectively, implying a larger specific area of the CoNC fibers than that of the FeNC fibers. Confirming our SEM observation, the BET surface area of the pyrolyzed CoNC fibers was measured to be 45.6 m^2/g which is three times larger than that (13.7 m^2/g) of the pyrolyzed FeNC fibers. It is noticeable that the diameters of the fibers increased by about 10% after heat-treatment. In addition, the diameter deviation of the pyrolyzed CoNC fibers is much larger than that of the as-spun CoPc/PAN fibers. This point can be visualized in Figure 6.1b that the pyrolyzed CoNC fibers have varying diameters even in different segments of a same fiber.

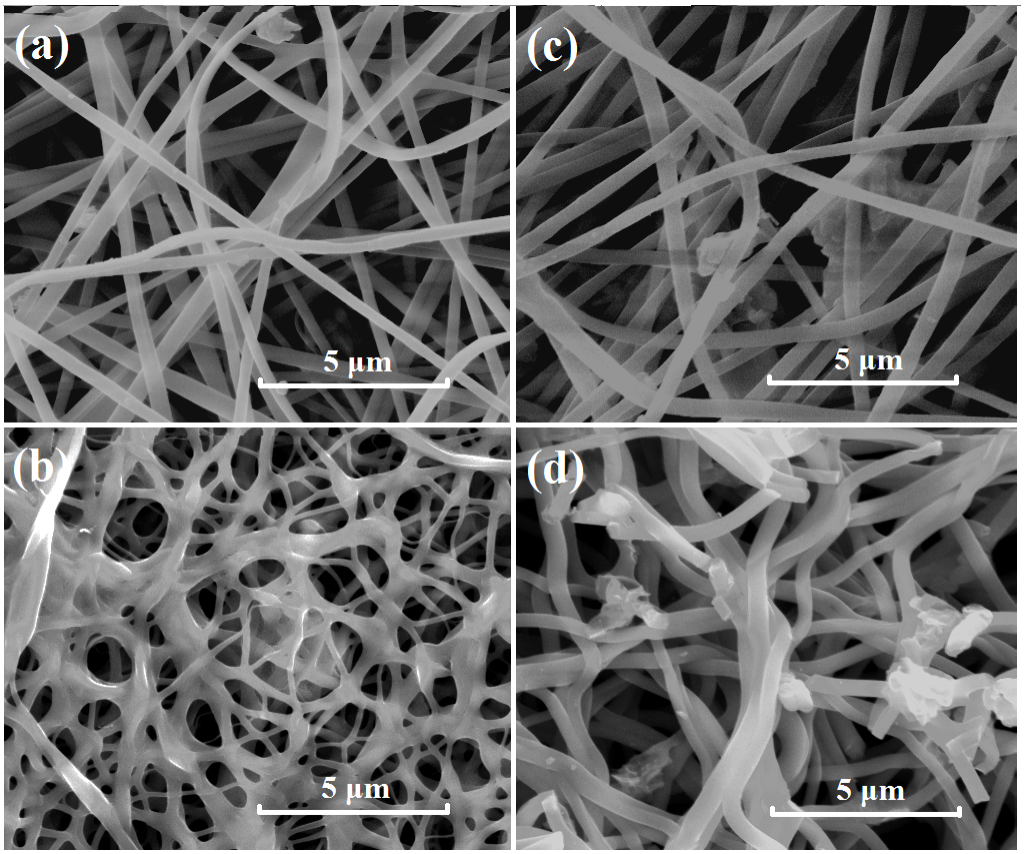

Figure 6.1: SEM images of (a) as-spun CoPc/PAN fibers, (b) pyrolyzed CoNC fibers, (c) as-spun FePc/PAN fibers, and (d) pyrolyzed FeNC fibers.

6.1.2 X-ray photoelectron spectroscopy

The results of elemental surface concentrations obtained from XPS for the pyrolyzed PAN, FeNC and CoNC fibers are given in Table 6.1. The overall N surface contents were found to be quite similar and range from 6.00 at.% to 7.76 at.% in all the three samples. The results indicate that there are about 0.44 at.% of Fe on the surface of the pyrolyzed FeNC fibers, about 0.51 at.% Co on the surface of the pyrolyzed CoNC fibers, but no metal contents on the surface of the pyrolyzed PAN fibers. Moreover, XPS measurements detected O species on the surface of all the three samples. These surface O species, whose content ranges from 2.15 at.% to 5.87 at.%, might be introduced onto the samples through exposure to air or the pre-oxidation process in the heat treatment. The surface O species has also been detected on pyrolyzed FeNC catalysts in a previous study. [52]

Table 6.1: Measured elemental surface concentrations (in unit of atomic percentage) from XPS for pyrolyzed PAN, FeNC and CoNC fibers.

	N_{total}	N1	N2	N3	N4	N5	C	O	Metal
PAN	7.76	2.57	-	3.64	0.39	1.17	90.09	2.15	-
FeNC	6.00	1.58	0.78	2.48	0.44	0.72	90.31	3.25	0.44
CoNC	6.47	1.65	1.13	2.43	0.49	0.78	87.15	5.87	0.51

Furthermore, narrow N 1s scans were analyzed to identify different N species on the sample surface (Figure 6.2). According to established procedures [52, 69], the N 1s spectrum was deconvoluted into five peaks corresponding to various nitrogen surface functionalities, namely, pyridinic nitrogen (N1), nitrile or/and TM-N_x (N2), pyrrolic nitrogen or/and secondary amine (N3), quarternary nitrogen (N4) and their oxidized forms (N5). It notes that the same constraints on the peak positions of N surface functionalities as those employed in Ref [69] were applied. The attained atomic percentages of various N species are presented in Table 6.1. The results show that the pyrrolic nitrogen or/and secondary amine (*i.e.* N3) are the main nitrogen surface species present in the pyrolyzed PAN, FeNC and CoNC samples. More importantly, the XPS study revealed that doping transition metal phthalocyanines

leads to additional nitrogen peak (N2) in the N 1s scans of the pyrolyzed FeNC and CoNC fibers. In stark contrast, this N2 peak is not observed in the N 1s scans of the pyrolyzed PAN fibers, indicating that the nitrile groups (–C≡N) in the PAN precursors have all been converted into other forms during the pyrolysis process. Consequently, the TM-N_x (FeN_x and CoN_x) clusters are believed to be the nitrogen functional groups present in the FeNC and CoNC fibers and responsible for appearance of the N2 peak. It is worth mentioning that the position of N2 peak was determined to be at 399.2 eV in the XPS spectra of the pyrolyzed FeNC and CoNC fibers and our result is in consistent with the peak position of TM-N_x reported before. [75, 132–134]

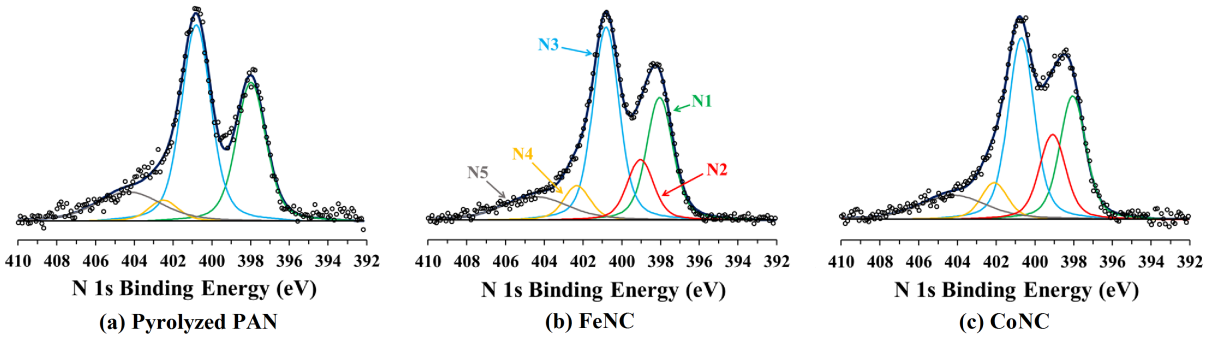

Figure 6.2: N 1s narrow scan spectra and deconvolutions for (a) pyrolyzed PAN fibers, (b) pyrolyzed FeNC fibers, and (c) pyrolyzed CoNC fibers.

Moreover, Figure 6.3 shows the narrow Fe 2p scan of the FeNC fibers and narrow Co 2p scan of the CoNC fibers. The Fe 2p scan shows a broad peak at 710.4 eV, suggesting that the surface irons are mainly in Fe(III) oxidation state [135]. These iron ions could possibly bound to nitrogen in the form of chelated FeN_x. Moreover, the Co 2p scan shows a broad peak at 780.4 eV, which is close to the known spectra of chelated CoN_x at 782.0 eV. [132, 133] With these experimental results, it is believed that the metal contents on the non-precious catalysts mainly exist in the form of TM-N_x rather than metallic clusters.

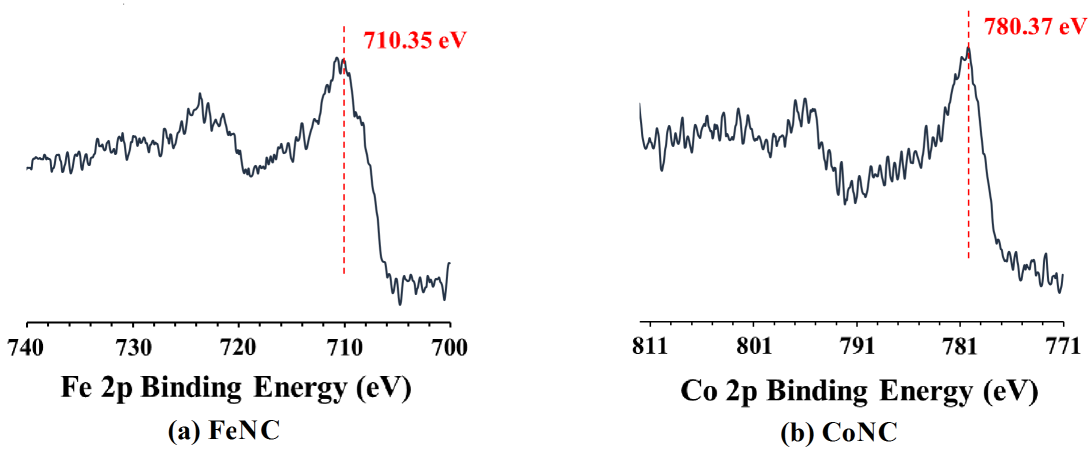

Figure 6.3: (a) Fe $2p$ narrow scan spectrum of the pyrolyzed FeNC fibers and (b) Co $2p$ narrow scan spectrum of the pyrolyzed CoNC fibers.

6.2 ELECTROCHEMICAL CHARACTERIZATIONS

6.2.1 RDE measurement

Important electrochemical reaction parameters (onset potential and number of electron transfer) for the ORR on the pyrolyzed CoNC and FeNC nanofiber catalysts in acid medium were obtained from the RDE measurement. For comparison, the RDE measurement was also performed for the ORR on Pt catalyst deposited on glassy carbon (GC) electrode with a loading of 1 mg/cm^2. The Pt catalyst employed in this study is fuel cell grade platinum black which was purchased from Sigma Aldrich.

In Figure 6.4a-c, the rotating disk polarization curves were showed at various rotation rates for ORR on an electrode coated with the pyrolyzed CoNC nanofiber (Figure 6.4a), the pyrolyzed FeNC nanofiber, (Figure 6.4 b) and the Pt black catalyst (Figure 6.4c) in a 0.5 M H_2SO_4 solution saturated with oxygen. From these plots, the onset potentials (defined as the potential at which 10% of the peak current value was reached) of the CoNC, FeNC, and Pt catalysts for ORR at a rotation rate of 1600 rpm are determined to be 0.68 V, 0.75 V and 0.91 V, respectively. The results show that the ORR onset potential of the CoNC catalyst is

more negative than that of the FeNC catalyst, concurring with previously published results that Co-based catalysts exhibited an ORR onset potential lower (by 0.12 V) than that of Fe-based ones in acid solution. [18]

Limited by mass transportation, the ORR on the Pt catalyst is observed to have a current plateau, for instance, at the potentials less than 0.6 V at 1600 rpm rotating rate (shown in Figure 6.4c). Unlike that of Pt catalyst, the RDE polarization curves of the pyrolyzed CoNC and FeNC catalysts (Figure 6.4a and b) do not display clear current plateaus in the high-polarization range, especially, at high rotating rates. This phenomenon has previously been observed for ORR on other non-precious metal catalysts [21, 136].

The number of electrons transferred during ORR on a catalyst can be computed from the slope of Koutechy-Levich plots in which the inverse of the measured current density at given potentials is depicted against the inverse square root of the electrode rotating rate [81]. The parameters in Levich Equation 2.1 were obtained from literatures: the diffusion coefficient of O_2 in the H_2SO_4 D_O is 1.9×10^{-5} cm^2/s [137]; the kinematic viscosity ν is 1.0×10^{-2} cm^2/s [138]; the concentration of oxygen in the 0.5 M H_2SO_4 electrolyte C_O is 1.1×10^{-6} mol/cm^3 [139]; In Figure 6.4d-f, the Koutecky-Levich plots (Equation 2.1) were presented for ORR on an electrode coated with the pyrolyzed CoNC nanofiber (Figure 6.4d), pyrolyzed FeNC nanofiber (Figure 6.4e), and Pt black catalyst (Figure 6.4f) at electrode potentials of 0.3 V, 0.2 V, and 0.1 V in a 0.5M H_2SO_4 solution saturated with oxygen. From the slopes of these Koutecky-Levich plots, the number of electrons transferred per O_2 molecule during ORR was calculated to be 4.1 on the Pt catalyst which is consistent with the well-known four-electron ($4e^-$) ORR on Pt catalysts. Furthermore, the electron transfer number is 3.3 for ORR on the FeNC catalyst but 2.5 on the CoNC catalyst in this study.

One the other hand, the rotating disk polarization curves in alkaline was also measured in a 0.1 M KOH solution for ORR on the pyrolyzed CoNC nanofiber (Figure 6.5a), the pyrolyzed FeNC nanofiber, (Figure 6.5 b) and the Pt black catalyst (Figure 6.5c). The onset potentials of the CoNC, FeNC, and Pt catalysts for ORR in alkaline at a rotation rate of 1600 rpm are 0.82 V, 0.86 V and 0.96 V, respectively. The results show that the order of ORR onset potential in alkaline is the same as that in acid. Moreover, all three catalysts deliver higher ORR onset potentials in alkaline than that in acid.

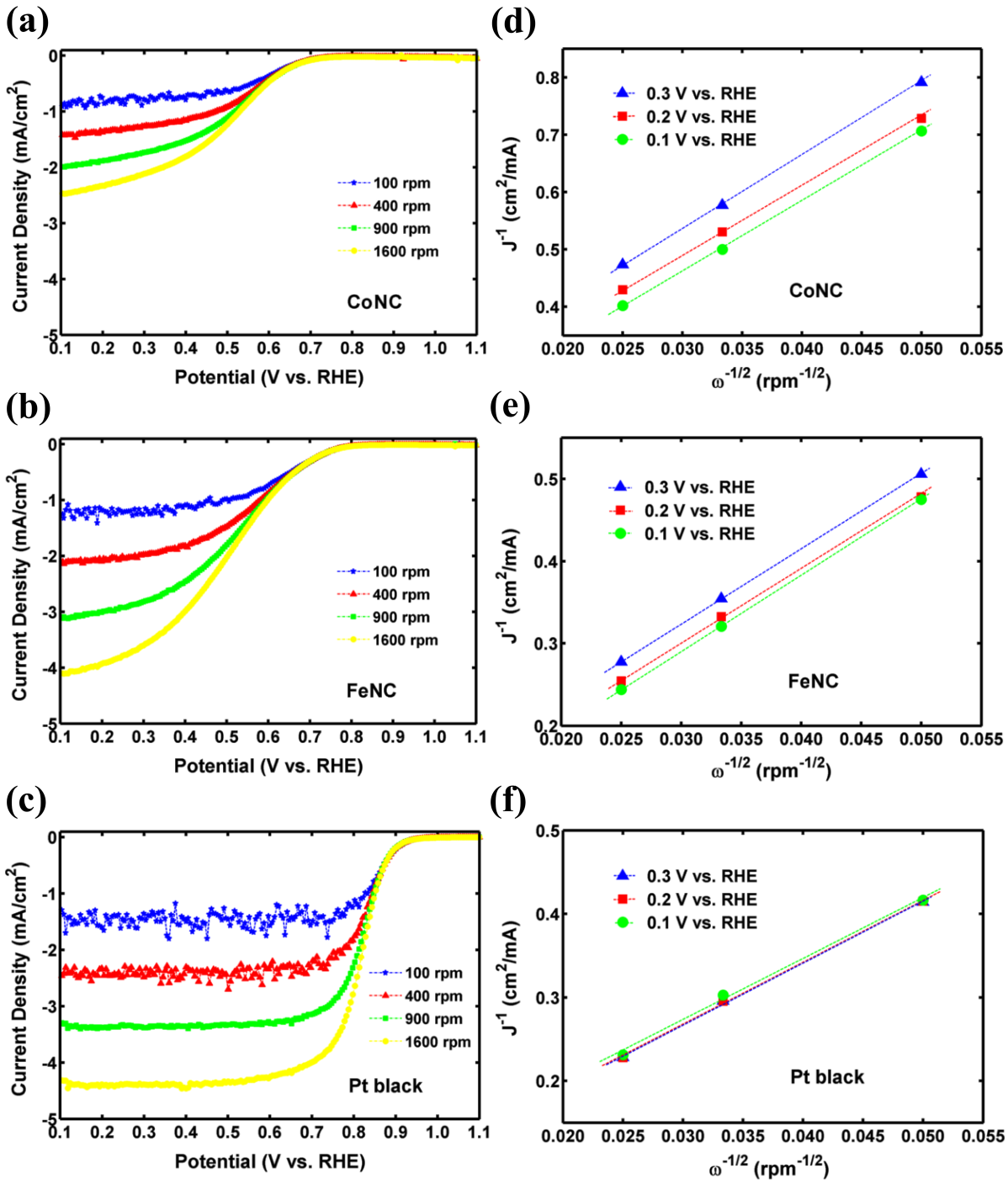

Figure 6.4: (a-c) RDE polarization curves at different rotation rates and (d-f) Koutecky-Levich plots at different electrode potentials for oxygen reduction on (a, d) pyrolyzed CoNC fibers, (b, e) pyrolyzed FeNC fibers, and (c, f) Pt black deposited glassy carbon (GC) electrode in a 0.5 M H_2SO_4 solution saturated with oxygen. GC disk area: 0.196 cm^2, scan rate: 5 mV/s, and room temperature.

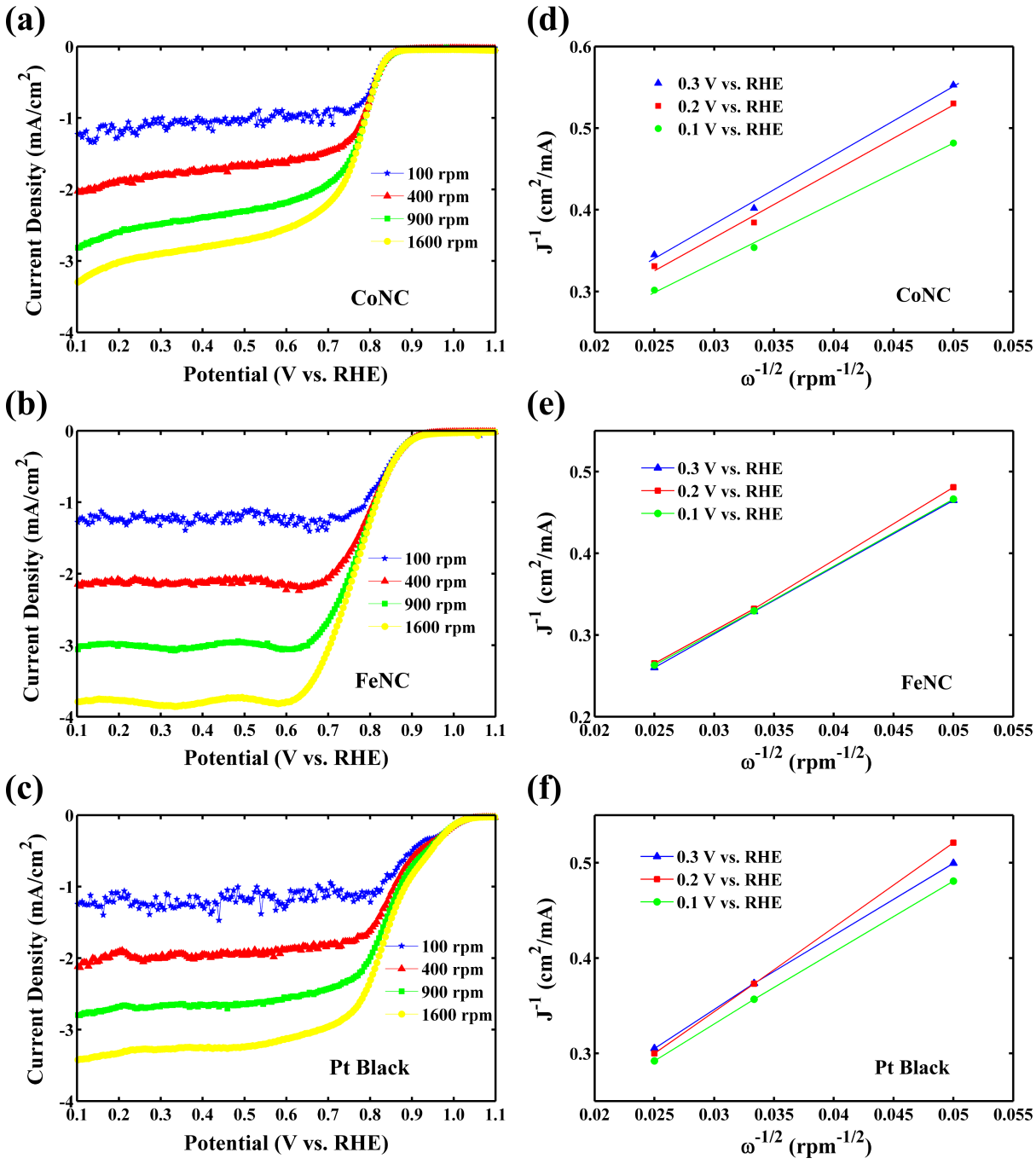

Figure 6.5: (a-c) RDE polarization curves at different rotation rates and (d-f) Koutecky-Levich plots at different electrode potentials for oxygen reduction on (a, d) pyrolyzed CoNC fibers, (b, e) pyrolyzed FeNC fibers, and (c, f) Pt black deposited glassy carbon (GC) electrode in a 0.1 M KOH solution saturated with oxygen. GC disk area: 0.196 cm^2, scan rate: 5 mV/s, and room temperature.

The electron transfer number for ORR in alkaline was also calculated using the corresponding parameters. Specifically, the concentration of oxygen in the 0.1 M KOH electrolyte was determined to be 1.20×10^{-6} mol/cm^3 [129] while the diffusion coefficient of O_2 and the kinematic viscosity used the same values as that in acid. In Figure 6.5d-f, the Koutecky-Levich plots (Equation 2.1) were presented for ORR on the pyrolyzed CoNC nanofiber (Figure 6.5d), pyrolyzed FeNC nanofiber (Figure 6.5e), and Pt black catalyst (Figure 6.5f) at electrode potentials of 0.3 V, 0.2 V, and 0.1 V in a 0.1M KOH solution. Concequently, the electron transfer number per O_2 molecule during ORR in alkaline is 3.7 on the Pt catalyst which is lower than that in acid. Moreover, the electron transfer number for ORR in alkaline is 3.4 on the FeNC catalyst but 3.6 on the CoNC catalyst, both of which are increased from that in acid especially for CoNC. The CoNC mainly catalyzes $2e^-$ ORR in acid while promotes $4e^-$ ORR in alkaline.

6.2.2 RRDE measurement

To compare the activity of the pyrolyzed PAN, FeNC, CoNC fibers and Pt catalysts, the polarization curves for ORR at a rotating rate of 1600 rpm are plotted in Figure 6.6a. The pyrolyzed FeNC and CoNC fibers exhibit significantly higher catalytic activities for ORR than the pyrolyzed PAN fibers. It is thus inferred that doped transition metal (Fe, Co) plays an important role in the formation of active sites for catalyzing ORR in the pyrolyzed FeNC and CoNC fibers.

Furthermore, the catalytic performance of the FeNC and CoNC fibers was found to be inferior as compared to that of Pt catalysts in acid. From the polarization curves in Figure 6.6a, it can be read that the Pt electrode (0.2 mg loading) outputs a current of 520 μA whereas the FeNC electrode (0.2 mg loading) outputs a much smaller current of 6.4 μA at electrode potential of 0.8 V. Thus, the mass activity of the Pt and the FeNC catalyst for ORR was calculated to be 2.6 A/g and 0.032 A/g at 0.8 V in this study. Moreover, the turnover frequency (TOF) [140] for ORR on the FeNC catalyst at this potential by assuming that the surface of the pyrolyzed FeNC catalyst has a structure of FeN_4 clusters embedded in a graphene layer. Using our measured values of 13.7 m^2/g for BET surface area and 0.78

at. % for N_2 surface species of the FeNC catalyst, the site density of the FeNC catalyst was estimated to be 1×10^{18} sites/g. Further, the TOF for ORR on the FeNC catalyst was estimated to be 0.2 e^-/s·site, which is close to 0.4 e^-/s·site reported for similar non-precious catalysts [34] but 125 times lower than the TOF value of 25 e^-/s·site for Pt nanoparticle catalysts [141]. These results suggest that the relatively inferior catalytic activity of the FeNC catalyst mainly results from low intrinsic activity of their active sites.

In contrast, the catalytic performance of the FeNC and CoNC fibers was found to be close to that of Pt catalysts in alkaline solution. The polarization curves in Figure 6.7a show that the Pt electrode (0.2 mg loading) outputs a current of 0.45 mA and the FeNC electrode (0.2 mg loading) outputs a close current of 0.25 mA at 0.8 V. Thus, the mass activity of the Pt and the FeNC catalyst for ORR was calculated to be 2.3 A/g and 1.3 A/g at 0.8 V. As a result, the activity of the FeNC catalyst in alkaline is 41 times higher than that in acid at 0.8 V. Similarly, the CoNC catalyst also shows significant ORR mass activity which is 0.73 A/g at 0.8 V in alkaline. The pyridinic nitrogen derived carbon in the FeNC and CoNC catalysts can serve as active sites for ORR in alkaline while becomes inert in acid, which accounts for the enhanced ORR activities for FeNC and CoNC catalysts in alkaline [142].

To further examine the ORR pathway selectivity on the synthesized CoNC and FeNC catalysts, RRDE measurement technique was used to detect the formation of H_2O_2 during the ORR process. The H_2O_2 yield can be calculated by Equation 5.1. The collection efficiency (N) of the RRDE system was suggested to be 0.246 through ferricyanide calibration [143]. The plot of calculated H_2O_2 yield *vs.* potential (inset of Figure 6.6b) reveals that no detectable amount of H_2O_2 is produced during the ORR on the Pt catalysts and very little H_2O_2 (˜5 %) is produced on the FeNC catalyst in acid. In contrast, the RRDE result indicates that a significant H_2O_2 yield rate (˜20%) has been observed for ORR on the CoNC catalyst in acid. Therefore, besides the RDE measurements (Koutecky-Levich plot), the RRDE measurements also qualitatively indicate that the ORR would proceed on the FeNC catalyst mostly through a $4e^-$ pathway, whereas the ORR could proceed on the pyrolyzed CoNC catalyst mainly through a $2e^-$ pathway in acid.

While in alkaline, the plot of calculated H_2O_2 yield *vs.* potential (inset of Figure 6.7b) reveals that 10 % H_2O_2 is produced during the ORR on the Pt catalysts, 36 % H_2O_2 is

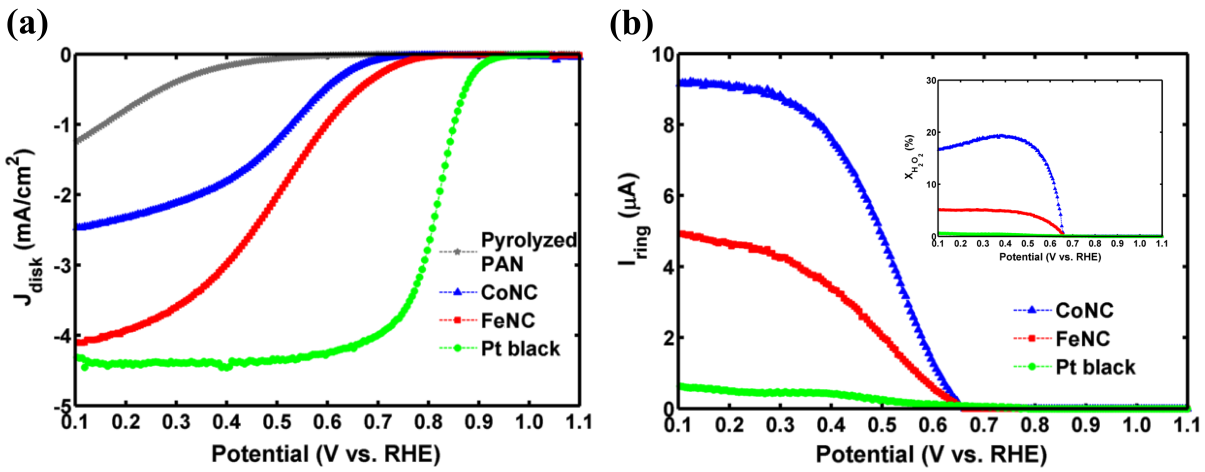

Figure 6.6: RRDE measurements of disk (a) and ring (b) current density for oxygen reduction reactions on pyrolyzed PAN, CoNC, FeNC nanofibers and Pt black deposited GC electrode with Pt ring at rotation rate of 1600 rpm in a 0.5 M H_2SO_4 solution saturated with oxygen. GC disk area: 0.196 cm2, Pt ring area: 0.11 cm2, scan rate: 5 mV/s, room temperature.

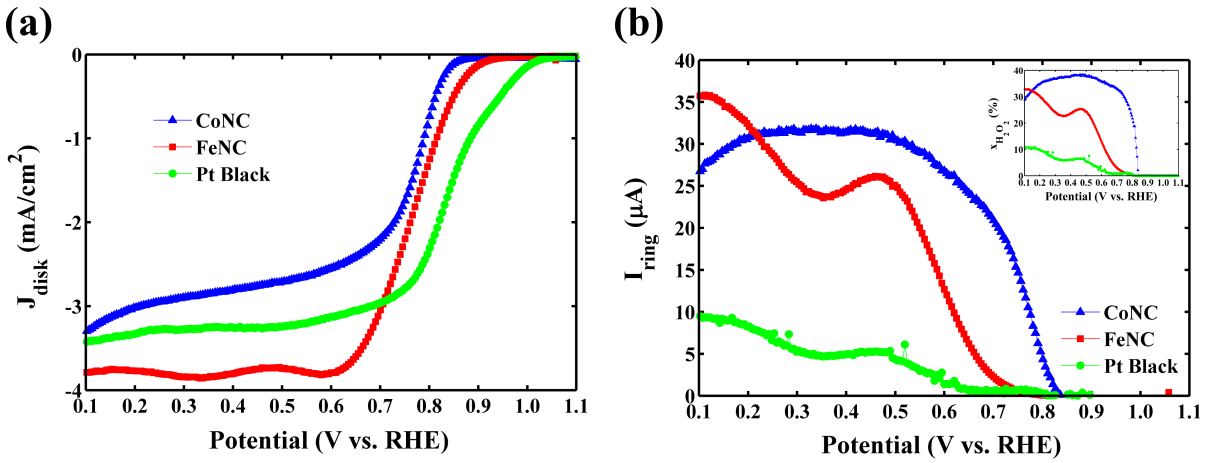

Figure 6.7: RRDE measurements of disk (a) and ring (b) current density for oxygen reduction reactions on pyrolyzed CoNC, FeNC nanofibers and Pt black deposited GC electrode with Pt ring at rotation rate of 1600 rpm in a 0.1 M KOH solution saturated with oxygen. GC disk area: 0.196 cm2, Pt ring area: 0.11 cm2, scan rate: 5 mV/s, room temperature.

produced on the FeNC catalyst, and 27 % % H_2O_2 is produced on the CoNC catalyst at 0.1 V. Quantitatively, the electron transfer number per O_2 molecule during ORR can be calculated by $4x_{H_2O_2} + 2(1 - x_{H_2O_2})$ which is 3.8 for Pt, 3.3 for FeNC, and 3.5 for CoNC at 0.1 V agreeing well with those derived from Levich plots. Concequently, both the FeNC and CoNC catalysts mainly promote $4e^-$ reduction of O_2 in alkaline. As explained above, the $4e^-$ ORR pathway in alkaline is probably adopted by the pyridinic nitrogen derived carbon active site which co-exists in the FeNC and CoNC catalysts [142].

7.0 RESULTS AND DISCUSSIONS: COMPUTATIONAL PART

7.1 O_2 ADSORPTION ON TM-N_4 COMPLEXES

7.1.1 Molecular structures of TM-N_4 macrocyclic complexes

The computational studies start from a simple case about the O_2 adsorption on TM-N_4 macrocyclic complexes. TM-N_4 macrocyclic complexes (FePc, CoPc) were used as precursors for synthesizing FeNC and CoNC catalysts in the experimental section, and the complexes have TM-N_4 centers which are analogues to the speculated active sites in the pyrolyzed TM-N-C catalysts. In this section, an investigation was conducted on two types of TM-N_4 macrocyclic complex molecules: transition metal porphyrins (TMP, structure shown in Figure 7.1) and transition metal phthalocyanines (TMPc, structure shown in Figure 7.1b). In both TMP and TMPc molecules, there are four pyrrolic nitrogen atoms chelated with the central TM atom. However, there are another four meso-position N atoms in a TMPc (but not in a TMP) molecule. In addition, a TMPc molecule always contains four benzo groups.

To investigate the effect of the central TM atom on O_2 adsorption, the DFT calculations were performed for a series of Cr-, Mn-, Fe-, Co-, and Ni- porphyrin and phthalocyanine molecules. As discussed in Ref. [144], the number of the electrons occupying the non-bonding *d*-type molecular orbitals would be 4, 5, 6, 7, and 8 in the Cr-, Mn-, Fe-, Co-, and Ni-N_4 macrocyclic complexes, respectively. To study the influence of the peripheral ligand groups on O_2 adsorption, the DFT calculations were also performed on Fe- (and Co-) tetraphenylporphyrins (FeTPP and CoTPP), Fe- (and Co-) fluorinated phthalocyanines ($FePcF_{16}$ and $CoPcF_{16}$), and Fe- (and Co-) chlorinated phthalocyanines ($FePcCl_{16}$ and

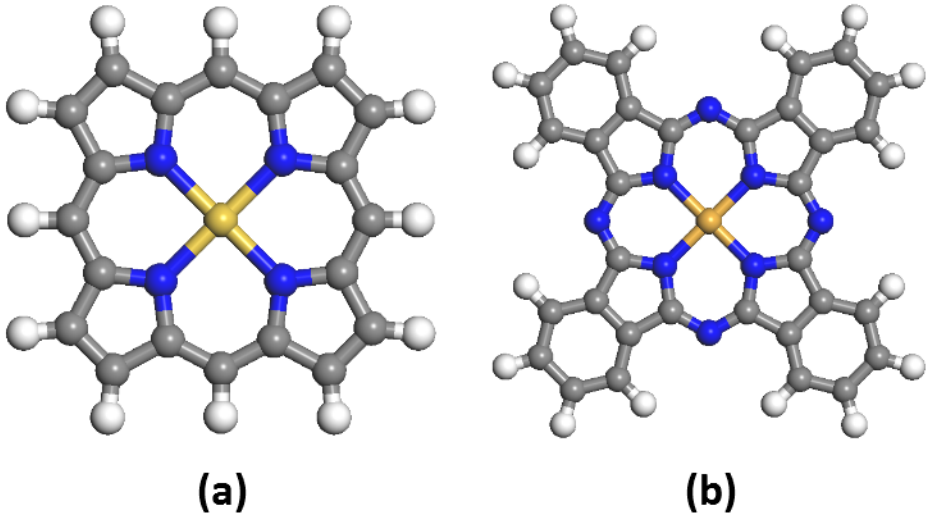

Figure 7.1: Molecular structures of (a) TMP and (b) TMPc macrocyclic complexes. In the figure, the central golden balls represent the TM atoms (here TM=Cr, Mn, Fe, Co, or Ni). The blue, gray, and white balls represent the nitrogen, carbon, and hydrogen atoms, respectively.

$CoPcCl_{16}$) molecules. In a TMTPP molecule, four phenyl groups substitute the four hydrogen atoms on the meso-position carbons in the corresponding TMP molecule. In a $TMPcF_{16}$ or $TMPcCl_{16}$ molecule, sixteen F or Cl atoms replace the sixteen H atoms in the benzo rings of the TMPc molecule. The previous DFT results indicated that the variation of these peripheral ligands affected appreciably the O_2 adsorption energy on the TM-N_4 macrocyclic complexes [86].

The molecular structures of these TM-N_4 macrocyclic complexes were fully relaxed using the DFT optimization method with specifying the proper spin multiplicity (see Appendix C) of the molecules. In all the optimized macrocyclic complexes, the central TM atom shares an exact plane with the four chelated N atoms. In Table 7.1, the calculated distance ($D_{\mathrm{TM-N}}$) between the central TM atom and the chelated N atoms was reported. It is notable that the predictions are in excellent agreement with those available values from literature [83, 84, 86, 145–150]. The results in Table 7.1 show clearly that in both the TMP and TMPc molecules the values of $D_{\mathrm{TM-N}}$ decrease systematically with an increasing atomic number of the central TM atom. In addition, the attained $D_{\mathrm{TM-N}}$ in a TMP molecule is always about 3% longer than that in the corresponding TMPc containing the same central TM atom. It can also be inferred from the results that a change in the peripheral ligands (specifically, addition of phenyl groups into TMP, and substitution H atoms with F or Cl atoms in TMPc) leads to only marginal variations in the value of $D_{\mathrm{TM-N}}$.

7.1.2 Electronic structures of TM-N_4 macrocyclic complexes

All the relaxed TM-N_4 macrocyclic complexes possess D4h symmetry and have square, planar TM-N_4 chelation configurations. Under this point group and taking the macrocyclic molecule to lie in the xy-plane, the $3d_{x^2+y^2}$, $4s$, $4p_x$, and $4p_y$ atomic orbitals of the central TM atom would form four metal-ligand bonding orbitals with the σ-hybrid orbitals from the four chelated N atoms, whereas the other four $3d$ orbitals of the central TM atom would mainly transform into four non-bonding d-type molecular orbitals (in specific, orbital a_{1g} from d_{z^2}, orbital b_{2g} from d_{xy}, and two degenerate orbitals e_g from d_{xz} and d_{yz}) [144]. Considering spin polarization (spin-up and spin-down), there will be eight non-bonding d-type molecular

Table 7.1: Calculated distance ($D_{\mathrm{TM-N}}$) between the central TM atom and its nearest neighboring N atom in the relaxed TM-N_4 macrocyclic complex molecules. For comparison, X-ray diffraction measurement data and other theoretical results are also included in the table.

	Multiplicity	$D_{\mathrm{TM-N}}$(Å)		
		This work	Exp.	Other works
CrP	Quintet	2.037		
MnP	Quartet	2.011	2.082 [145]	2.006 [84]
FeP	Triplet	1.994	1.970 [146]	1.999 [84]
FeTPP	Triplet	1.986	1.972 [146]	1.970 [149]
CoP	Doublet	1.985	1.950 [147]	1.987 [84]
CoTPP	Doublet	1.981	1.949 [147]	1.967 [149]
NiP	Singlet	1.967		1.974 [84]
CrPc	Quintet	1.980		
MnPc	Quartet	1.952		
FePc	Triplet	1.935	1.928 [148]	1.923 [83]
$FePcF_{16}$	Triplet	1.938		1.928 [83]
$FePcCl_{16}$	Triplet	1.948		1.945 [86]
CoPc	Doublet	1.930	1.910 [151]	1.917 [83]
$CoPcF_{16}$	Doublet	1.933		1.922 [83]
$CoPcCl_{16}$	Doublet	1.943		1.944 [86]
NiPc	Singlet	1.911		1.923 [150]

orbitals as the frontier orbitals of these TM-N_4 macrocyclic complexes. When a chemical species adsorbs on the TM-N_4 macrocyclic complexes, these non-bonding d-type molecular orbitals are believed to contribute most to the bond formation between the adsorbate and the macrocyclic molecule [152]. Hence, the energy levels and electron occupancy of these d-type molecular orbitals in the equilibrium TM-N_4 macrocyclic complexes were calculated using the DFT method. Figure 7.2 plots the calculated energies of the non-bonding d-type molecular orbitals with respect to that of the lowest unoccupied molecular orbital (LUMO) for the TMP (Figure 7.2a) and TMPc (Fig 7.2b) macrocyclic complexes. For a macrocyclic molecule, the d-type molecular orbitals will be fully occupied if their energies are below that of the LUMO and will be empty if their energies are above that of the LUMO.

As shown in Figure 7.2, the electron occupancy on the non-bonding d-type molecular orbitals of the TM-N_4 macrocyclic complexes is predicted as follows: 4 electrons occupy 4 spin-up d orbitals with an electronic configuration of $(b_{2g})^1(a_{1g})^1(e_g)^2$ in the Cr-N_4 molecules, 5 electrons occupy 4 spin-up and 1 spin-down d orbitals with an electronic configuration of $(b_{2g})^2(a_{1g})^1(e_g)^2$ in the Mn-N_4 molecules, 6 electrons occupy 4 spin-up and 2 spin-down d orbitals with an electronic configuration of $(b_{2g})^2(a_{1g})^1(e_g)^3$ in the Fe-N_4 molecules, 7 electrons occupy 4 spin-up and 3 spin-down d orbitals with an electronic configuration of $(b_{2g})^2(a_{1g})^1(e_g)^4$ in the Co-N_4 molecules, and 8 electrons occupy all 4 spin-up and 4 spin-down d orbitals with an electronic configuration of $(b_{2g})^2(a_{1g})^2(e_g)^4$ in the Ni-N_4 molecules. The analysis indicates that the two spin-down e_g orbitals of the Fe-N_4 molecules are both partially occupied (50 %) by valence electron. Consequently, it was considered that the highest occupied molecular orbital (HOMO) of the Fe-N_4 molecules to be energetically degenerate with their LUMO. It is also noticeable in Figure 7.2 that the spin-up and spin-down d-type molecular orbitals of the Ni-N_4 molecules are degenerate in energy. Using a different DFT software, previous theoretical study reported that the d electron configuration should be $(b_{2g})^2(a_{1g})^2(e_g)^2$ for the groundstate FeP and FePc molecules and $(b_{2g})^2(a_{1g})^2(e_g)^3$ for the groundstate CoP and CoPc molecules [149, 150]. It appears that the predictions about the electronic structure of the FePc and CoPc molecules are more consistent with experimental measurements [153].

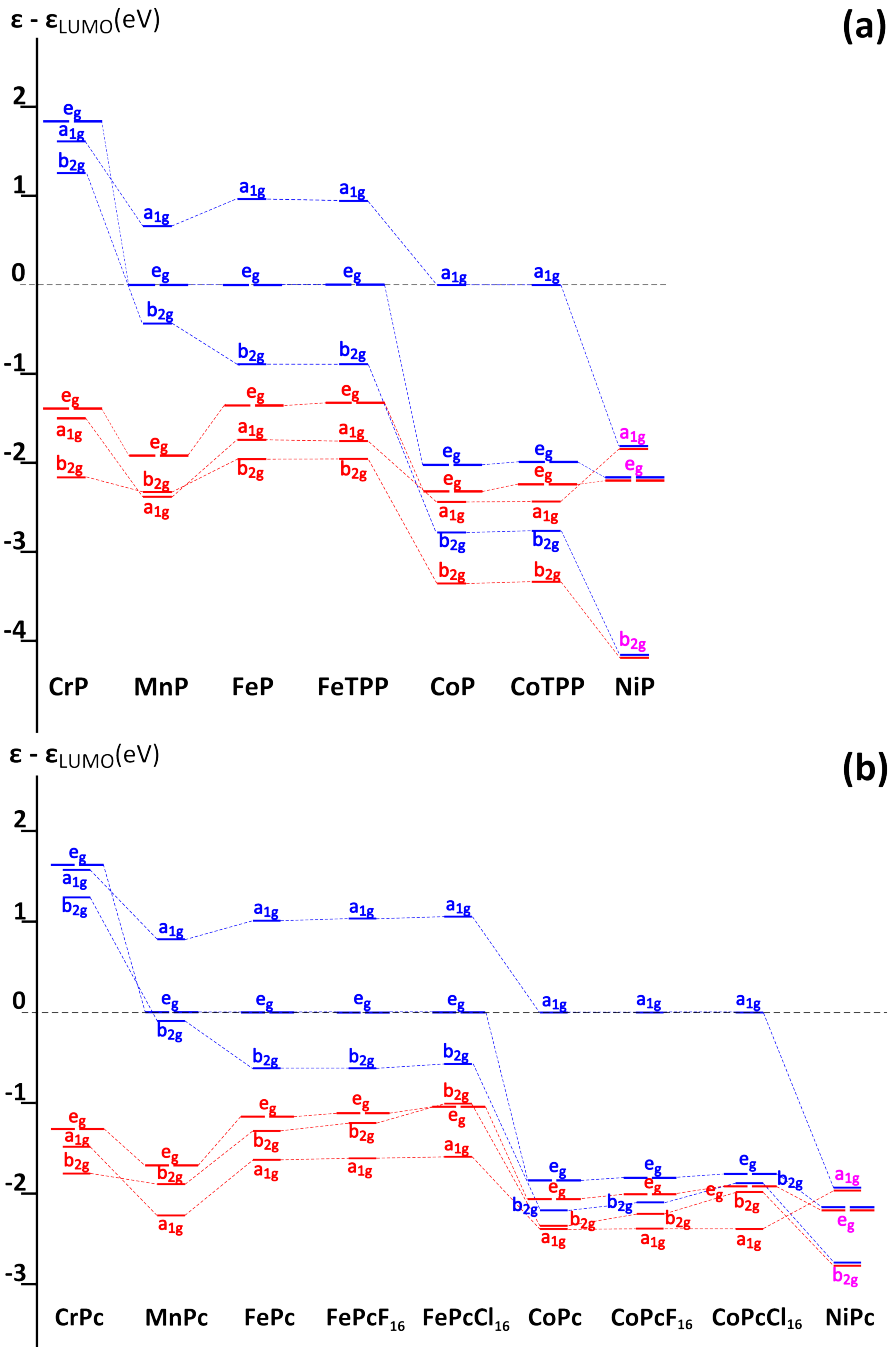

Figure 7.2: Calculated energy levels (relative to that of the LUMO) of the non-bonding d orbitals in (a) TMP and (b) TMPc macrocyclic complexes. In the figure, the red lines represent the spin-up non-bonding d orbitals, the blue lines represent the spin-down non-bonding d orbitals, the dashed lines are used to link the same molecular orbital in different macrocyclic molecules.

Furthermore, the orbital energy level diagrams in Figure 7.2 illustrate the effect of the central TM atom and peripheral ligand group on the electronic structure of the TM-N_4 macrocyclic complexes. Particularly, the average energy level of the eight non-bonding *d*-type molecular orbitals with respect to the LUMO energy (denoted as *d*-orbital center) was found to vary significantly with the change in the element type of the central TM atom. For both the TMP and TMPc molecules, the *d*-orbital center descends following the order of Cr (CrP: 0.01 eV, CrPc: 0.03 eV), Fe (FeP: -0.79 eV, FePc: -0.60 eV), Mn (MnP: -1.03 eV, MnPc: -0.85 eV), Co (CoP: -2.16 eV, CoPc: -1.84 eV), and Ni (NiP: -2.59 eV, NiPc: -2.27 eV) in terms of the type of the central TM atom. In contrast, the variation in the peripheral ligand groups induces comparatively small changes upon the *d*-orbital center of the TM-N_4 macrocyclic complexes. For example, it was predicted that adding phenyl groups at the meso-position carbons of the FeP (and CoP) mainly increase the energy level of the occupied spin-up orbital of e_g (corresponding to $3d_{xz}$ or $3d_{yz}$ orbitals of the TM atom) closer to the LUMO by 31 meV (and 80 meV) in the FeTPP (and CoTPP) molecules. Moreover, the substitution of peripheral hydrogen atoms by fluorine or chlorine atoms mainly shifts the occupied spin-up b_{2g} (corresponding to $3d_{xy}$ orbital of the TM atom) orbital of the FePc and CoPc molecules. As compared to that of the FePc, the energy level (relative to LUMO energy) of the spin-up b_{2g} orbital was found to increase by 87 meV in the $FePcF_{16}$ and by 267 meV in the $FePcCl_{16}$ molecules. As compared to that of the CoPc, the energy level (relative to LUMO energy) of the spin-up b_{2g} orbital was calculated to increase by 132 meV in the $CoPcF_{16}$ and by 373 meV in the $CoPcCl_{16}$ molecules.

7.1.3 O_2 adsorption molecular structures on TM-N_4 macrocyclic complexes

The adsorption of O_2 molecule on Fe-N_4 and Co-N_4 macrocyclic complexes have already been investigated using the DFT calculation method [83, 85]. In these studies, it has been identified that there are four possible stable configurations for the O_2 molecule to adsorb on the TM-N_4 macrocyclic molecules. Figures 7.3a and b show two end-on O_2 adsorption configurations in which one O atom lies above the central TM atom and the other O atom tilts away from the TM atom. Hence, the two O atoms of the end-on adsorbed O_2 molecule

have different distances to the TM atom. Figures 7.3c and d depict two side-on O_2 adsorption configurations in which the adsorbed O_2 molecule extends parallel to the TM-N_4 macrocyclic complexes and the two O atoms of the adsorbed O_2 molecule are in equal distance from the central TM atom. All the four O_2 adsorption configurations have been examined on each TM-N_4 macrocyclic complex (see Appendix C) and Table 7.2 shows the computed properties for the lowest-energy O_2 adsorption configuration on the TM-N_4 macrocyclic complexes. The listed properties include: adsorption configurations (shown in Figure 7.33), spin multiplicity, adsorption energy (ΔE_{ad}), distance ($D_{\mathrm{TM-O1}}$) between the central TM atom and the nearest neighboring O atom (O1), bond length $D_{\mathrm{O1-O2}}$) of the O-O bond, and angle ($\angle O_2O_1TM(^\circ)$) formed by the central TM atom with the two oxygen atoms.

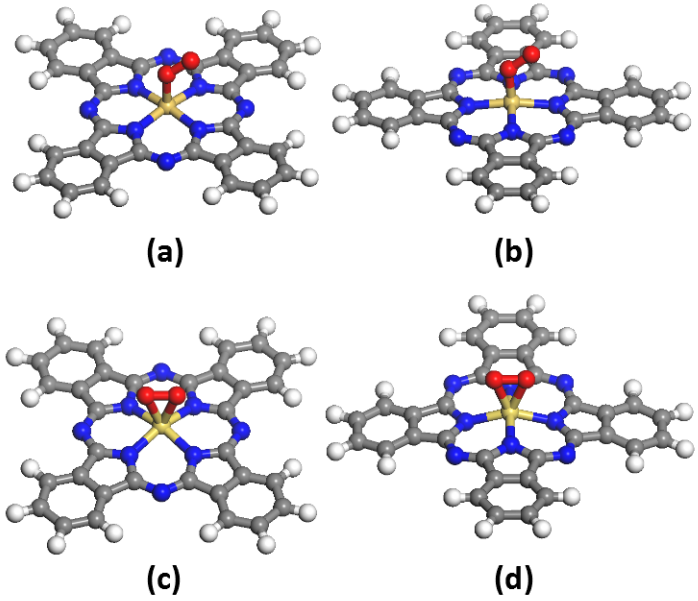

Figure 7.3: Four possible configurations of O_2 molecule adsorbed on TM-N_4 macrocyclic complexes. (a, b) end-on configuration; (c, d) side-on configuration. Here, the TMPc molecule is used as an example case representing the TM-N_4 macrocyclic molecules. In the figure, the central golden balls represent the TM atoms (here TM=Cr, Mn, Fe, Co, or Ni). The red, blue, gray, and white balls represent the oxygen, nitrogen, carbon, and hydrogen atoms, respectively.

Table 7.2: Calculated energetic and structural properties of O_2 molecule adsorption on TM-N_4 macrocyclic complexes.

	CrP	MnP	FeP	FeTPP	CoP	CoTPP
Configurations	Fig. 7.3d	Fig. 7.3d	Fig. 7.3a	Fig. 7.3a	Fig. 7.3b	Fig. 7.3b
Multiplicity	Triplet	Quartet	Singlet	Singlet	Doublet	Doublet
ΔE_{ad} (eV)	-1.218	-0.872	-0.906	-0.937	-0.582	-0.610
$D_{\mathrm{TM-O1}}$ (Å)	1.850	1.880	1.743	1.743	1.901	1.898
$D_{\mathrm{O1-O2}}$ (Å)	1.398	1.359	1.278	1.281	1.271	1.273
$\angle \mathrm{O_2O_1TM}(^\circ)$	67.80	68.80	121.52	121.56	118.69	118.64
	NiP	CrPc	MnPc	FePc	$\mathrm{FePcF_{16}}$	$\mathrm{FePcCl_{16}}$
Configurations	Fig. 7.3b	Fig. 7.3d	Fig. 7.3d	Fig. 7.3a	Fig. 7.3a	Fig. 7.3b
Multiplicity	Triplet	Triplet	Quartet	Singlet	Singlet	Singlet
ΔE_{ad} (eV)	-0.080	-1.211	-0.837	-0.818	-0.798	-0.876
$D_{\mathrm{TM-O1}}$ (Å)	2.752	1.850	1.883	1.758	1.762	1.770
$D_{\mathrm{O1-O2}}$ (Å)	1.238	1.398	1.361	1.279	1.276	1.275
$\angle \mathrm{O_2O_1TM}(^\circ)$	118.91	67.80	68.81	120.13	120.29	123.83
	CoPc	$\mathrm{CoPcF_{16}}$	$\mathrm{CoPcCl_{16}}$	NiPc		
Configurations	Fig. 7.3b	Fig. 7.3b	Fig. 7.3b	Fig. 7.3b		
Multiplicity	Doublet	Doublet	Doublet	Triplet		
ΔE_{ad} (eV)	-0.496	-0.465	-0.584	-0.057		
$D_{\mathrm{TM-O1}}$ (Å)	1.912	1.929	1.936	3.003		
$D_{\mathrm{O1-O2}}$ (Å)	1.268	1.264	1.264	1.233		
$\angle \mathrm{O_2O_1TM}(^\circ)$	117.11	118.64	119.36	115.15		

As listed in Table 7.2, it was predicted that the adsorbed O_2 molecule would prefer to assume a side-on configuration on the Cr- and Mn- macrocyclic complexes with a severely stretched O-O bond (*i.e.*, large value of D_{O1-O2}), but energetically favor an end-on configuration on the Fe-N_4, Co-N_4, and Ni-N_4 macrocyclic complexes. The binding strength between the adsorbed O_2 and the TM-N_4 macrocyclic molecules can be gauged by the calculated adsorption energy ΔE_{ad}. Negative adsorption energy implies that it is preferable for O_2 to be adsorbed on the TM-N_4 macrocyclic molecules. The more negative ΔE_{ad} is, the more strongly the O_2 molecule binds to the TM-N_4 macrocyclic molecules. Hence, the results in Table 7.2 indicate that the O_2 molecule would bind most strongly to the Cr- macrocyclic complexes whereas bind most weakly to the Ni- macrocyclic complexes. Our DFT calculations predicted for the O_2 molecule adsorption on the NiP and NiPc molecules nearly zero binding energy and significantly large separation D_{TM-O1} between the O atoms and the central Ni atom. Thus, our results imply that the O_2 molecule could not be chemisorbed on the Ni- macrocyclic complexes. Additionally, the results revealed that peripheral ligand groups could modulate the O_2 adsorption energy to some modest degree. For example, substituting end H atoms with Cl atoms causes the O_2 adsorption energy to be 0.088 eV stronger on the $CoPcCl_{16}$ than on the CoPc molecule.

7.1.4 O_2 adsorption electronic structures on TM-N_4 macrocyclic complexes

Furthermore, the analysis was conducted on the molecular orbitals around LUMO/HOMO of the O_2-TM-N_4 macrocyclic molecule adsorption systems in order to understand the electronic origin of the negative adsorption energy for these systems. In summary, it was found that the chemisorption between O_2 molecule and TM-N_4 macrocyclic complexes was primarily due to the formation of some bonding orbitals through the interaction of the π^* anti-bonding orbitals of the O_2 molecule and the non-bonding d-type molecule orbitals (*i.e.*, a_{1g} , b_{2g}, and e_g orbitals in Figure 7.2 of the TM-N_4 macrocyclic complexes. It is worth mentioning that in its triplet ground state, O_2 molecule has two unpaired electrons located in two degenerate π^* anti-bonding orbitals, four paired electrons located in two degenerate π bonding orbitals, and two paired electrons located in a σ bonding orbital (denoted as 'n' orbital).

It was predicted that the lowest-energy adsorption configuration for the O_2 adsorption on the Cr- and Mn- macrocyclic complexes is the side-on configuration (shown in Figure 7.3d). Regarding this chemisorption system, Griffith had proposed that the bonding between the O_2 and the TM-N_4 macrocyclic complexes consisted of both a σ-type bond and a π-type bond formed by the interaction of the π orbitals of the O_2 and the d orbitals of the central TM atom [90]. Confirming this theory, three occupied molecular orbitals of the side-on O_2-MnPc adsorption system (as a representative example) are shown in Figure 7.4. In the figure, Figure 7.4a depicts the formation of a σ-type bond through the interaction between the n-π hybrid orbital of the O_2 and the singly occupied a_{1g} (d_{z^2}) orbital of the MnPc, Figure 7.4b depicts the formation of a π-type bond by overlapping one occupied π^* anti-bonding orbital of the O_2 with the singly occupied e_g (d_{xz} or d_{yz}) orbital of the MnPc, and Figure 7.4c depicts the formation of a δ-type bond by overlapping the other occupied π^* anti-bonding orbital of the O_2 with the doubly occupied b_{2g} (d_{xy}) orbital of the MnPc.

The results in Table 7.2 also indicate that O_2 molecule would prefer to adopt an end-on configuration, in which the two O atoms and the central TM atom will form an angle close to 120° as suggested by Pauling [89], when be adsorbed on the Fe-N_4 and Co-N_4 macrocyclic complexes. The predictions are in good agreement with the previous crystallographic results about O_2 adduction on these metal complexes [154]. The O_2-$CoPcF_{16}$ adsorption system was chosen as a representative case to illustrate the bond formation in an end-on O_2 adsorption configuration. Figure 7.5 shows two occupied molecular orbitals of the end-on O_2-$CoPcF_{16}$ adsorption system. In the figure, Figure 7.5a plots the formation of a σ-type bond by overlapping one π^* anti-bonding orbital of the O_2 with the singly occupied a_{1g} (d_{z^2}) orbital of the $CoPcF_{16}$ and Figure 7.5b depicts the formation of a π-type bond by overlapping the other π^* anti-bonding orbital of the O_2 with the doubly occupied e_g (d_{xz} or d_{yz}) orbital of the $CoPcF_{16}$ molecule.

As observed above, with any adsorption configuration (Figure 7.3), the π^* anti-bonding orbitals of the adsorbed O_2 molecule would interact with the non-bonding d orbitals of the TM-N_4 macrocyclic complexes to form some new bonding orbitals with lower energies for the adsorption system. Consequently, the two unpaired electrons on the two π^* anti-bonding orbitals of the O_2 together with the unpaired electrons (if there are any) on the non-bonding

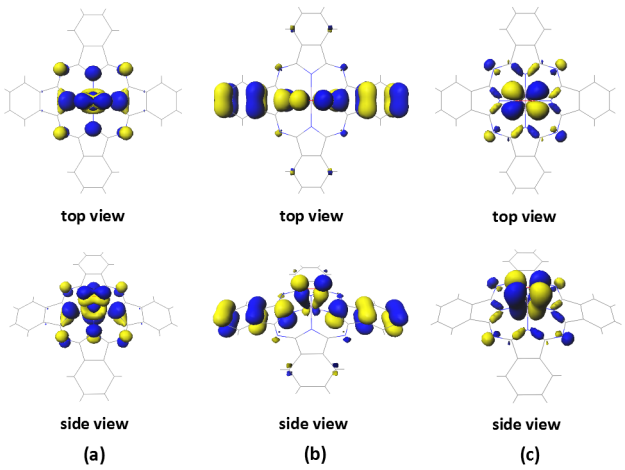

Figure 7.4: Some electronic orbitals of the O_2-MnPc system adopting the side-on configuration shown in Figure 7.3d: (a) d_{z^2} orbital, (b) d_{xz} or d_{yz} orbital, and (c) d_{xy} orbital of the central Mn atom in the MnPc molecule at an isovalue of ± 0.03 a.u. In the figure, the colors blue and yellow are used to represent the different signs of the wave functions.

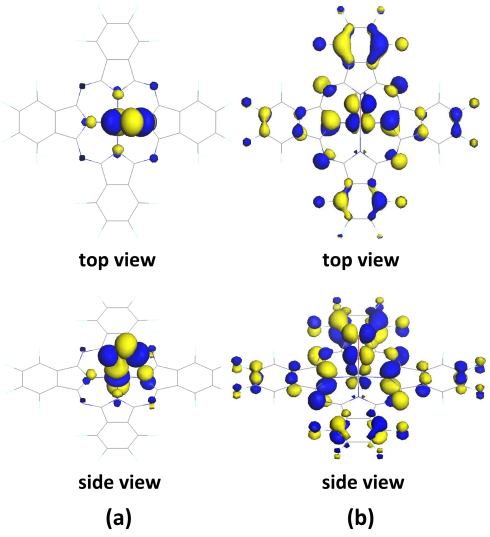

Figure 7.5: Some electronic orbitals of the O_2-$CoPcF_{16}$ system adopting the end-on configuration shown in Figure 7.3b: (a) d_{z^2} orbital and (b) d_{xz} or d_{yz} orbital of the central Co atom in the $CoPcF_{16}$ molecule at an isovalue of ± 0.03 a.u. In the figure, the colors blue and yellow are used to represent the different signs of the wave functions.

d orbitals of the TM-N_4 macrocyclic complexes could form pairs and favorably fill up the newly formed bonding orbitals of the adsorption system. In this way, the total energy of the adsorption system will be lowered and the negative chemisorption energy is thus induced. This understanding about the electronic origin of the O_2 adsorption energy explains why no O_2 chemisorption is found on the Ni-N_4 macrocyclic complexes. It is because that there are 8 electrons fully occupying all the non-bonding d orbitals of the Ni-N_4 macrocyclic complexes and no un-paired electron available for pairing up with the π^* electrons of the O_2 molecule in their O_2 adsorption systems.

7.1.5 Correlation between adsorption energy and electronic structure

Similar to the d-band theory for transition metal catalysts [79], a correlation between the calculated O_2 adsorption energy and the electronic structure of the TM macrocyclic complexes has been established. It states in the d-band theory that the adsorption energy of chemical species on transition metal surfaces is strongly correlated with the position of the d-band center of their outermost surface layer. The d-band center of transition metal surfaces is defined as the first-moment center of the density of states of the d-electrons with reference to the Fermi energy of the surfaces. The predictions from the d-band theory are in excellent agreement with theoretical computations [155] and experimental measurements [29]. In this study for O_2 adsorption on TM-N_4 macrocyclic complexes, it was proposed that the O_2 adsorption energy is related to the d orbital center ($\delta\varepsilon_d$), which is defined as the average energy of all the non-bonding d orbitals (a_{1g}, b_{2g}, and e_g orbitals in Figure 7.2) with respect to the energy value of the LUMO of the TM macrocyclic molecule. This proposition is based on the observation that the chemisorption of O_2 molecule on the TM macrocyclic complexes was primarily a result of the interaction of the π^* anti-bonding orbitals of the O_2 molecule and the non-bonding d-type molecular orbitals of the TM-N_4 macrocyclic complexes. Furthermore, the proposition was verified by plotting the calculated O_2 adsorption energy (ΔE_{ad}) as a function of the calculated d orbital center ($\delta\varepsilon_d$) of the TMP macrocyclic complexes in Figure 7.6a and the TMPc macrocyclic complexes in Figure 7.6b. Both plots show clearly

linear correlation between the O_2 adsorption energy on the TM macrocyclic molecule and the defined d orbital center of the same TM macrocyclic molecule.

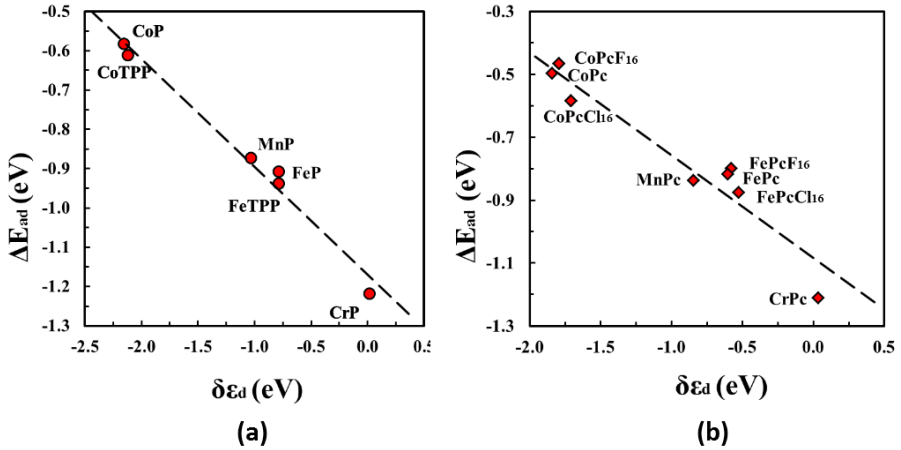

Figure 7.6: Variation of calculated O_2 adsorption energy (ΔE_{ad}) with respect to calculated non-bonding d orbital center ($\delta\varepsilon_d$) of (a) TMP and (b) TMPc macrocyclic complexes. In the figure, the red circles and diamonds represent our computation data and the dashed lines indicate the linear fitting of the data.

Because O_2 was found not adsorb chemically on the NiP or NiPc molecules, the results for these two macrocyclic complexes were not included in Figure 7.6. For the other TMP and TMPc macrocyclic complexes with chemisorbed O_2, the results in Figure 7.6 indicate that the O_2 adsorption energy becomes more negative (namely, stronger binding) with an up-shift of their d orbital center ($\delta\varepsilon_d$). Following this rule, the CrP and CrPc molecules with a d orbital center closest to their LUMOs would bind O_2 molecule most strongly. Corresponding to the intermediate positions of their d orbital centers, the Mn-N_4 and Fe-N_4 macrocyclic complexes bind O_2 with adsorption energy around -0.8 to -0.9 eV. Importantly, the results in Figure 7.6 reveal how the peripheral ligand groups affect the O_2 adsorption energy on the TM-N_4 macrocyclic complexes. As discussed in Section 7.1.2, adding phenyl groups at the meso-position carbons of the FeP (and CoP) can move the occupied spin-up e_g orbital closer to the LUMO and hence up-shift the d orbital center of the FeTPP (and CoTPP) molecule. Similarly, the substitution of peripheral hydrogen atoms by fluorine or chlorine atoms shifts

up the d orbital center of the $FePcF_{16}$, $FePcCl_{16}$, $CoPcF_{16}$, and $CoPcCl_{16}$ molecules by raising the occupied spin-up b_{2g} orbitals of the FePc and CoPc molecules. Indeed, the up-shift of the d orbital center leads to more negative adsorption energy of the O_2 adsorption on the FeTPP (and CoTPP) than on the FeP (and CoP), and on the $FePcCl_{16}$ and $CoPcCl_{16}$ than on the FePc and CoPc molecules. However, it was also observed exceptions in Figure 7.6 that the calculated O_2 adsorption energy on the $CoPcF_{16}$ and $FePcF_{16}$ was slightly less negative than on the CoPc and FePc molecule even though their d orbital center was predicted to be more closer to the LUMO.

7.1.6 Discussions

The four-electron ORR starts from the adsorption of O_2 on the catalyst surface and proceeds with the generation of various possible chemical intermediates such as O, OH, OOH, HOOH, and final product of H_2O [80, 99, 156]. It has been found that O_2 adsorption energies usually increase (or decrease) simultaneously with the increase (or decrease) in the adsorption energy of the ORR intermediates such as OH and H_2O_2 on the TM-N_4 macrocyclic complexes [86]. Consequently, the catalytic activity of the TM-N_4 macrocyclic complexes for ORR is expected to exhibit a volcano shape as a function of the O_2 adsorption energy. In other words, O_2 adsorption energy can be considered as a parameter indicating the ORR activity of the TM-N_4 macrocyclic complexes, as had been demonstrated for transition metals [130]. Therefore, the results in Figure 7.6 link actually the ORR activity and the electronic structure of the TM-N_4 macrocyclic complexes. It has been found experimentally that Fe-N_4 macrocyclic complexes had quite high ORR activity but degraded quickly in electrochemical environments whereas Co-N_4 macrocyclic complexes had comparably low ORR activity (assuming two-electron pathway) but good stability [81]. Hence, it was inferred that a desired TM macrocyclic molecule catalyst with good combination of the activity for ORR and durability might have the O_2 adsorption energy and d orbital center between those of the Fe-N_4 and Co-N_4 macrocyclic complexes. The DFT calculations in this section predicted that the Mn-N_4 macrocyclic complexes met such requirements. Indeed, some researchers reported

that MnPc and MnP could electrocatalyze the reduction of oxygen at low overpotentials following the four-electron ORR pathway [14, 157–159].

In this section, the d orbital center of the TM-N_4 macrocyclic complexes is identified as an important parameter indicating the binding strength between the O_2 molecule and these complexes and thus the ORR activity of the TM-N_4 macrocyclic complexes. A general trend is that the closer the d orbital center is to the LUMO, the more strongly the O_2 would bind to the TM-N_4 macrocyclic complexes. In addition, the results in Figure 7.6 revealed that the energy level (or position) of the d orbital center of the TM-N_4 macrocyclic complexes was dominantly determined by the element type of the central TM atoms and modestly modulated by the peripheral ligand groups. Thus, a guiding principle was suggested here about how to enhance their ORR catalytic performance through tuning the d orbital center of the TM-N_4 macrocyclic complexes. Previous study suggested that some optimal catalyst should have the O_2 adsorption energy between those of the Fe-N_4 and Co-N_4 macrocyclic complexes [81, 86]. To accomplish this objective, it can either down-shift the d orbital center of the Fe-N_4 macrocyclic complexes or up-shift the d orbital center of the Co-N_4 macrocyclic complexes through rational design of their peripheral ligand groups.

In the experimental Section 6, the FePc and CoPc were employed as the precursors for synthesizing the pyrolyzed FeNC and CoNC catalysts. Although TM-N_x clusters are still believed to be the active sites for ORR [18], these TM-N_x clusters in the heat-treated sample may have different structures than the planar TM-N_4 clusters studied in this section. Nevertheless, the results in this section could be helpful on understanding the ORR activity of the pyrolyzed TM-N-C catalysts. For example, the TM-N_4 cluster in the heat-treated catalysts may adopt non-planar trigonal bipyramid geometry (with C_{2v} symmetry) instead of planar structure (with C_{4v} symmetry). Such a C_{4v} to C_{2v} structural transformation could lead to one of the two originally degenerate e_g orbitals (d_{xz} and d_{yz}) more stabilized and the other one more diminished [153]. Thus, structural transformation of the TM-N_4 clusters could cause some shift of the d orbital center and hence their ORR activities. Moreover, it is possible that a fifth ligand (besides the four N- ligands) is attached to the central TM metal after pyrolysis [46]. This fifth ligand will raise up the energy of orbital a_{1g} (*i.e.* d_{z^2}) [153] and

hence up-shift the d orbital center to LUMO for stronger O_2 adsorption. Consequently, the insights attained in this section about the correlation between the O_2 adsorption energy and the d orbital center of TM-N_4 macrocyclic complexes should be useful for the development of high-performance non-precious ORR catalysts.

7.2 ORR ON TM-N-C CATALYSTS: EFFECT OF TM

7.2.1 Model of active sites

To date, the chemistry of the active sites in pyrolyzed TM-N-C catalysts for ORR has not been fully understood. In previous experimental studies, it has been suggested that the transition metals, such as Fe and Co, anchored with nitrogen atoms in carbon support act as ORR active sites in this type of catalysts [73, 160, 161]. Formation of Fe-N_x sites was further confirmed by a recent microscopic study that showed that Fe and N tended to stay adjacent to each other in a pyrolyzed FeNC catalyst based on graphenecarbon nanotube (CNT) complexes [19]. In this section, it was inferred from the electrochemical tests and XPS characterizations in Section 6 that the TM-N_x clusters present on the pyrolyzed FeNC and CoNC fiber surfaces are probably the active sites for catalyzing ORR.

In particular, planar TM-N_x sites embedded in carbon matrix are often suggested to be responsible for the ORR performance of TM-N-C catalysts [17, 73, 74, 162]. Complementary to experimental studies, the DFT calculation has been employed to theoretically examine the possibility of various TM-N_x clusters as ORR active sites [64, 93, 95, 101, 163–166]. Surveying these published DFT calculation results on FeN_x sites, it was noticed that the planar FeN_4 cluster embedded in monolayer graphene has been predicted to have the lowest formation energy among possible FeN_x sites [93], exhibit reasonably strong attraction to reactant O_2 molecule for ORR initiation, and bind H_2O molecule more weakly than the solvation stabilization energy of bulk water to allow ORR product removal [93]. Consequently, the model of CoN_4 (or FeN_4) clusters embedded in a monolayer graphene was adopted as the active sites of pyrolyzed CoNC (or FeNC) catalysts for ORR in this section.

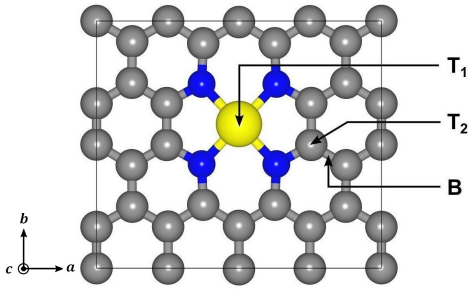

Figure 7.7: Atomic model of CoN_4 (or FeN_4) cluster embedded in monolayer graphene. In the figure, the gray, blue, and yellow balls represent C, N, and Co (or Fe) atoms, respectively. Letters T_1, T_2, and B mark the adsorption site on the top of metal Co (or Fe) atom, on the top of an adjacent C atom, bridging the two neighboring C atoms, respectively.

As shown in Figure 7.7, the active site of the pyrolyzed catalysts was modelled with a 32-atom graphene super cell with lattice parameters a = 9.84 Å, b = 8.52 Å and with periodic boundary conditions in three dimensions. The periodic images of the graphene layers were separated by a 14 Å vacuum in the c-direction to avoid the artificial interactions between the periodic images. Inside the graphene super cell, the central two C atoms were replaced by a transition metal TM (TM=Co or Fe) atom and the four C atoms surrounding the TM atom were substituted by four N atoms. It should be noted that the thermodynamic stability of other TM-N_x (x=0, 1, 2, 3, and 4) clusters embedded in a monolayer graphene was also examined and it was confirmed that the TM-N_4 cluster has the lowest formation energy among all the possible TM-N_x clusters.

7.2.2 Adsorption energy

The adsorption energies of possible ORR species (*i.e.*, O_2, H, O, OH, OOH, H_2O_2, and H_2O) adsorbed on the TM-N_4 (TM = Co or Fe) active sites were calculated by the DFT methode using VASP. The adsorption energy was calculated by Equation 5.10. Hence, negative adsorption energies indicate the extent of attraction between the catalytic active site and the ORR species adsorbed. Table 7.3 gives the calculation results of adsorption energies. The detailed atomistic structures of the relaxed adsorption configurations can be found in the previous publication for ORR on FeN_4 cluster embedded in graphene [93].

On both CoN_4 and FeN_4, the DFT calculations predicted that ORR reactant O_2 molecule could be favorably adsorbed on the central transition metal atom. The calculated adsorption energies of O_2 on these non-precious catalysts are comparable to those on Pt catalysts (-0.69 eV on Pt(111) [80] and -1.10 eV on Pt(100) [156]). Hence, the non-precious catalysts are predicted to be possible to initiate the ORR. Moreover, the DFT results showed that ORR product H_2O molecule would bind to the active sites rather weakly (less than 0.20 eV in energy gain). Since the solvation stabilization energy of bulk water is about 0.40 eV, the H_2O produced from the ORR is thus predicted to be more favorable to leave the active sites of the non-precious catalysts and move into electrolyte. Consequently, the DFT results

Table 7.3: Calculated adsorption energies (in units of eV) of ORR species adsorbed on CoN_4 and FeN_4 active sites. Notation of adsorption sites can be found in Figure 7.7.

ORR species	Adsorption sites	CoN_4	FeN_4
O_2	T_1	-0.67	-0.98
H_2O	T_1	-0.02	-0.18
OOH	T_1	-1.23	-1.76
H_2O_2	T_1	-0.04	-0.23
H	T_1	-2.27	-2.20
H	T_2	-1.46	-1.40
O	T_1	-3.18	-4.53
O	B	-2.75	-2.47
OH	T_1	-2.44	-2.80
OH	T_2	-1.41	-1.45

suggest that the CoN_4 and FeN_4 could be active sites for ORR. The results in Table 7.3 also indicate that OOH binds quite strongly but H_2O_2 binds very weakly on CoN_4. These DFT results imply that the ORR on CoN_4 could possibly end with a $2e^-$ pathway due to easy desorption of H_2O_2.

7.2.3 Free energy landscape

The dissociative mechanism and associative mechanism are two possible $4e^-$ pathways for ORR on the TM-N_4 clusters. The O-O bond scission would take place through the O_2 dissociation reaction in the dissociative mechanism whereas through OOH dissociation reaction in the associative mechanism. First, the activation energy (E_a) for the O_2 dissociation and OOH dissociation reactions was calculated on the CoN_4 and FeN_4 active sites by locating the transition state of the reactions using the CI-NEB method. Figure 7.8 shows the atomistic structures of the two dissociation reactions on the TM-N_4 sites attained from the DFT calculations. The DFT transition state calculation results indicate that the direct dissociation reaction of O_2 into two O species is more difficult than the dissociation of OOH on both the CoN_4 (with $E_a = 1.96$ eV) and FeN_4 (with $E_a = 1.19$ eV). Consequently, the dissociative mechanism is highly unfavorable on the CoN_4 and FeN_4 active sites. Hence, the subsequent calculations mainly focus on the associative mechanism of ORR.

Figure 7.9a plots the free energy evolution of the ORR associative pathway on the CoN_4 and FeN_4 active sites at temperature of 300 K. The free energy landscapes were calculated using the computational approach described in Section 5.2.2 The ORR associative pathway consists of a sequence of O_2 protonation reaction, OOH dissociation reaction, O protonation reaction and two OH protonation reactions.

Figure 7.9a shows that, when electrode potential (U) is zero, all the ORR steps in this $4e^-$ ORR pathway are thermodynamically favorable (*i.e.*, downhill in free energy) on the FeN_4 site. In contrast, it was found in Figure 7.9a that the step of *OOH dissociation into *O and *OH on the CoN_4 site requires an increase in free energy by 0.39 eV. In addition, the

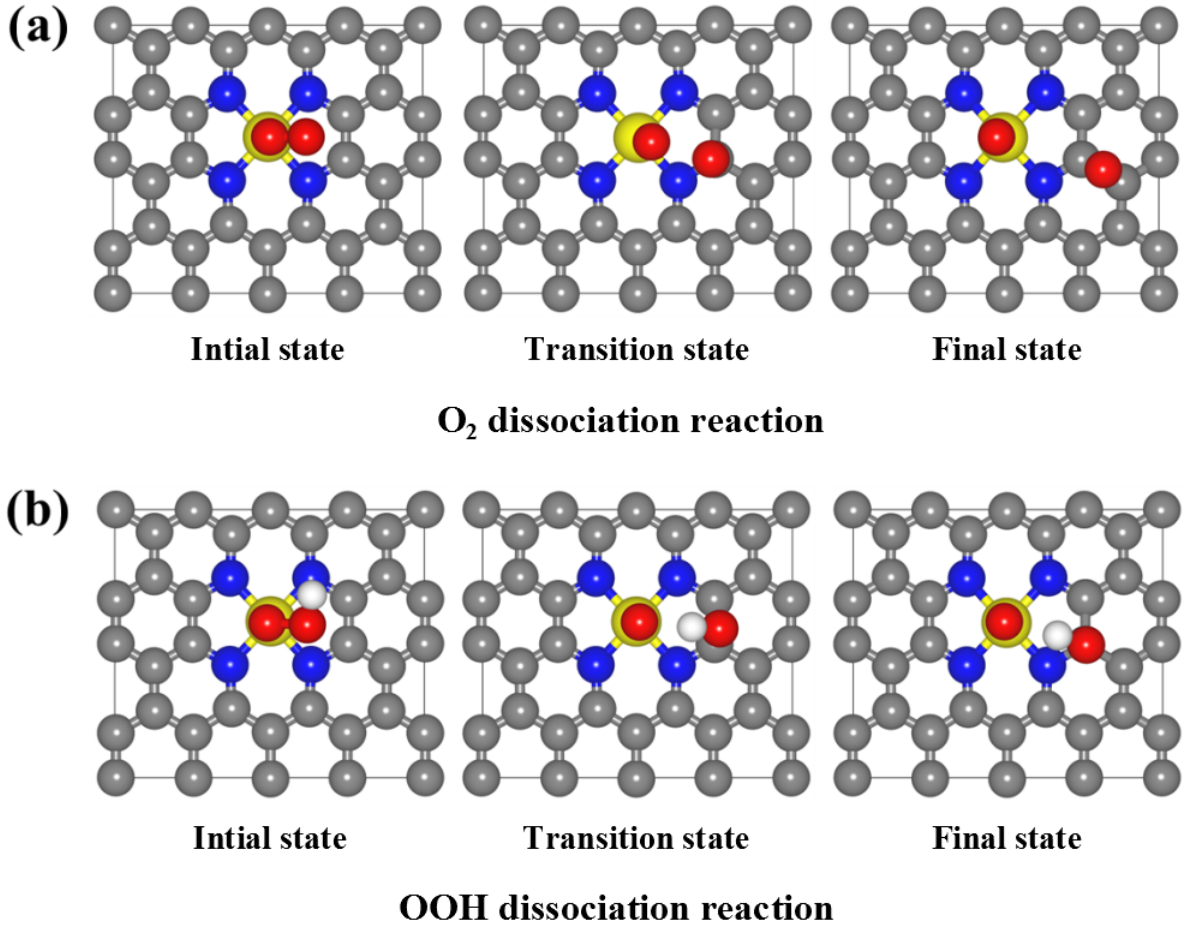

Figure 7.8: Atomic structures of the initial state, transition state, and final state for reactions (a) $*O_2(T_1) \rightarrow *O(T_1) + *O(B)$ and (b) $*OOH(T_1) \rightarrow *O(T_1)+*OH(T_2)$ on the CoN_4 (or FeN_4) active sites embedded in graphene. In the figure, the gray, blue, yellow, red, and white balls represent C, N, Co (or Fe), O, and H atoms, respectively.

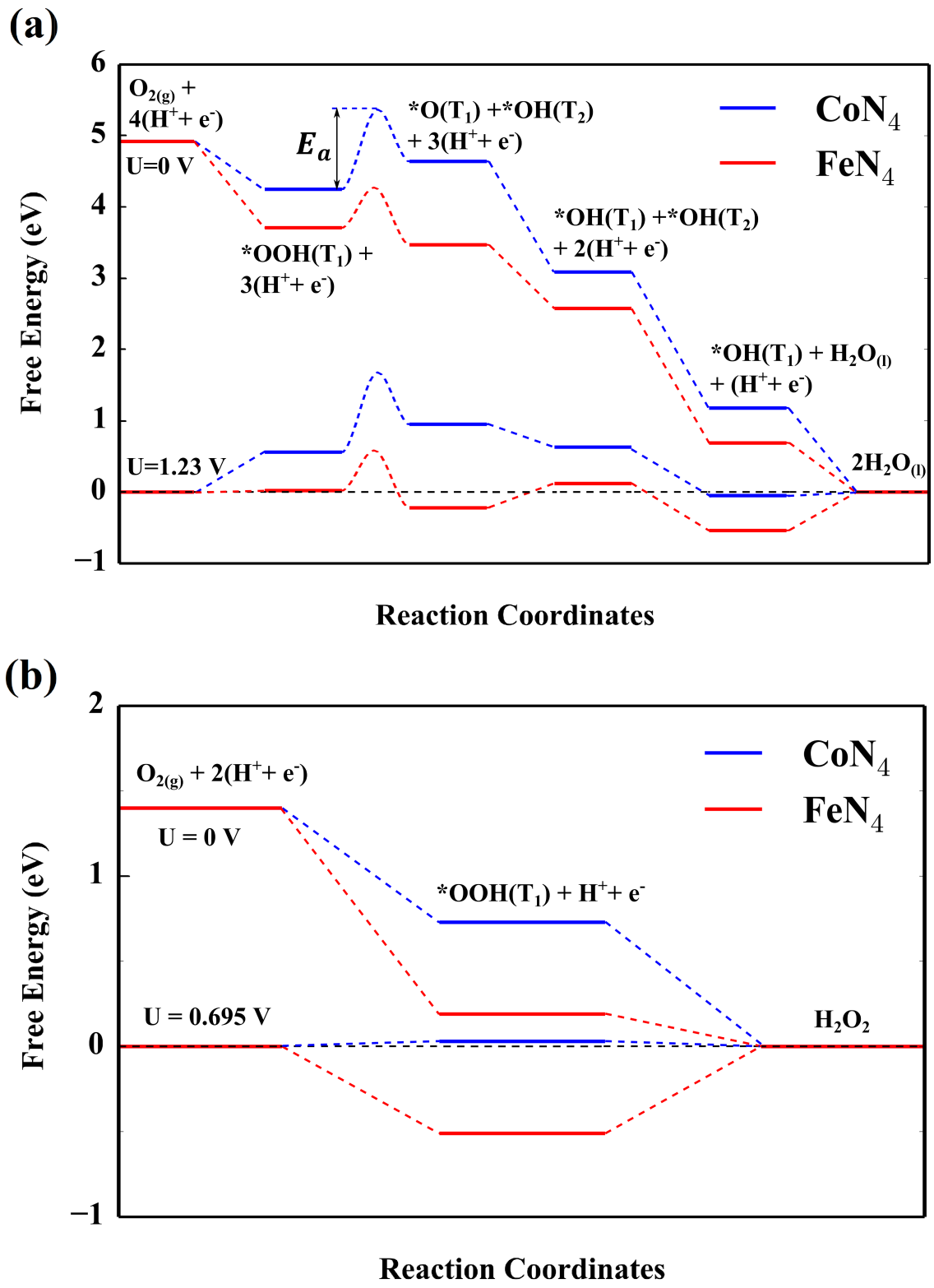

Figure 7.9: Free energy diagrams for (a) the O_2 reduction through $4e^-$ associative pathway to produced H_2O and (b) the O_2 reduction through $2e^-$ pathway to produce H_2O_2 on the CoN_4 and FeN_4 active sites in acid medium.

activation energy for the OOH dissociation reaction was predicted to be 1.11 eV on the CoN_4 site as compared to 0.56 eV on the FeN_4 site. Assuming that pre-exponential factor has a typical surface vibrational frequency 10^{13}, it was thus estimated that the reaction constant of this OOH dissociation reaction could be as low as 2×10^{-6}/s on the CoN_4 site whereas 3900/s on the FeN_4 site at 300 K. Hence, it can be inferred that the $4e^-$ ORR associative pathway is feasible on the FeN_4, whereas the same pathway is kinetically impractical for ORR on the CoN_4 site. When electrode potential U is above 0.69 V, the free energy change for the OH protonation reaction on the FeN_4 site becomes positive. Consequently, the DFT calculations predicted that the $4e^-$ ORR pathway shown in Figure 7.9a is active on the FeN_4 up to a limiting potential of 0.69 V. The predicted limiting potential (0.69 V) lies in between the onset potential (0.75 V) and half-wave potential (0.55 V) measured for ORR on the FeNC catalyst in Section 6.2.1.

It has been noted that the DFT calculated free energies of *OH and *OOH bound on various metal and oxide surfaces differ by a constant amount of about 3.2 eV [167]. In this section, it was found that the free energy difference between *OH and *OOH was 3.02 eV on the FeN_4 and 3.07 eV on the CoN_4 sites. Both values are within the error of 0.2 eV to the reported scaling constant of 3.2 eV [168, 169]. It appears that the universal scaling relation between *OH and *OOH still holds true for oxygen reduction electrocatalysis on non-precious TM-N_4 based catalysts.

Alternative to $4e^-$ ORR pathways, the oxygen could be reduced to hydrogen peroxide, which has a standard electrode potential of 0.695 V [58], through a $2e^-$ pathway. Figure 7.9b plots the free energy evolution diagram on the FeN_4 and CoN_4 sites for oxygen reduction to H_2O_2 through a sequence of O_2 protonation reaction and OOH protonation reaction steps [170]. It is shown in Figure 7.9b that, all the ORR steps in this $2e^-$ ORR pathway are thermodynamically favorable (*i.e.*, downhill in free energy) on both the FeN_4 and CoN_4 sites under low electrode potential. In particular, the free energy calculation results indicated that the limiting potential would be 0.67 V (limited by O_2 protonation step) for the ORR on the CoN_4 site following this $2e^-$ pathway. Therefore, instead of overcoming the high energy barrier (1.11 eV) for the OOH dissociation reaction along the $4e^-$ ORR pathway, the ORR could proceed through the $2e^-$ ORR pathway on the CoN_4 site. It is worth noting that the

theoretical value of the limiting potential for the $2e^-$ ORR on the CoN_4 site is close to the measured ORR onset potential of 0.68 V on the pyrolyzed CoNC catalyst in Section 6.2.1.

7.2.4 Pyridinic nitrogen derived active site

Metal-free nitrogen doped carbon (N-C) materials has also been reported to have ORR activity in alkaline before [171–173]. Regarding the ORR active sites in metal-free N-C catalysts, many suspected that pyridinic nitrogen and/or quaternary nitrogen moieties doped in carbon matrix play active role for catalyzing the ORR [171, 172, 174–176]. One recent study examined the ORR activity of the N-C catalysts containing well-controlled nitrogen species and further pointed out that the carbon atoms activated by neighboring pyridinic nitrogen were the actual ORR active sites in these metal-free N-C catalysts [177]. The pyridinic nitrogen derived carbon site also exists in the pyrolyzed TM-N-C catalysts as shown in Section 6.1.2, thus the thermodynamics of ORR on the pyridinic nitrogen derived carbon active site was studied by DFT method in this section. In acid electrolytes, the pyridinic N will be protonated to form pyridinic NH due to the strong interaction between the positively charged protons and the lone-pair electrons of the pyridinic N, which is speculated to account for the inferior activity of the TM-N-C catalysts for ORR in acid than in alkaline [55, 56, 178]. Therefore, the pyridinic N derived carbon (C-pyri-N) active site was modeled as the C atoms adjacent to un-protonated (in alkaline) and protonated (in acid) pyridinic N doped on the zigzag edge of the graphene nanoribbon (Figure 7.10a).

The adsorption energies of major chemical species (*i.e.* O_2, OOH, O and OH) involved in the ORR on C-pyri-N and C-pyri-NH active sites are presented in Table 7.4. The DFT calculations predicted that the adsorption energies of O_2 on the C-pyri-N and C-pyri-NH sites are higher than -0.1 eV, indicating weak O_2 binding to these active sites. These calculation results are consistent with those from the previous study by Choi *et. al.* [68, 179] Thus, the result implies that these metal-free C-pyri-N sites could not attract O_2 gas molecule. Furthermore, the DFT calculations predicted that the OOH adsorption energy on the C-pyri-N site is close to those on the TM-N_4 sites (Table 7.3). These results suggest that the ORR on the non-protonated C-pyri-N sites might take place following a process of long-

range electron transfer to non-adsorbed O_2 at the outer Helmholtz plane (so-called ET-OHP mechanism) [174, 180] in which O_2 undergoes a hydrogenation reaction in the electrolytes and subsequently product OOH is adsorbed on the catalysts to complete the remaining steps of ORR. However, the OOH adsorption on the protonated C-pyri-NH site is rather weak and thus even the ET-OHP mechanism of ORR could be very difficult for ORR to occur on these C-pyri-NH sites.

Table 7.4: Calculated adsorption energies (in units of eV) of ORR species (O_2, OOH, O and OH) adsorbed on C-pyrid-N (in alkaline) and C-pyrid-NH (in acid) sites.

ΔE_{ad}	C-pyri-N	C-pyri-NH
O_2	-0.025	-0.076
OOH	-1.37	-0.39
O	-2.85	-3.24
OH	-2.61	-1.65

Figure 7.10b plots the free energy evolutions along the ORR associative pathway on the C-pyri-N and C-pyri-NH sites at temperature of 300 K. It shows that all the ORR steps in the associative pathway are thermodynamically favorable (*i.e.*, downhill in free energy) on the C-pyri-N site at 0.75 V. Above 0.75 V, the last step of OH protonation reaction becomes thermodynamically unfavorable. In contrast, the free energy of *OOH on the C-pyri-NH site is so high that the ORR cannot be activated even under potential lower than 0.75 V. Thus, the DFT results indicate that the metal-free non-protonated C-pyri-N site could catalyze the ORR through the ET-OHP mechanism with a limiting potential of 0.75 V. Moreover, the metal-free protonated C-pyri-NH site would become inactive for ORR if pyridinic N is protonated, since the calculated corresponding limiting potential is 0.09 V. As a result, the computational predictions above provide a reasonable explanation to the experimental observation that the ORR on the TM-N-C catalysts has significantly lower activities in acid than that in alkaline (Section 6.2.1).

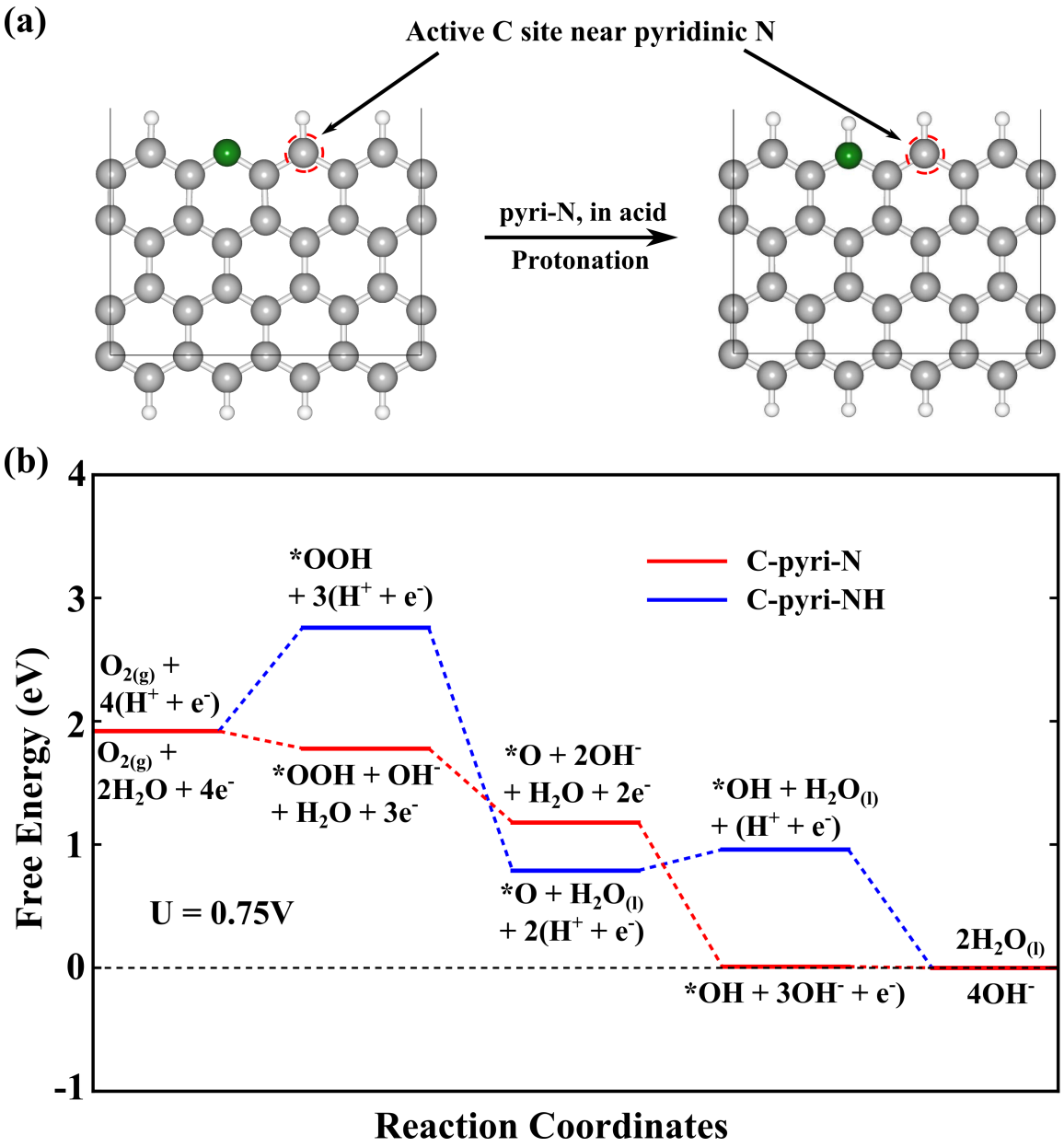

Figure 7.10: DFT calculation results of ORR on C-pyri-N (in alkaline) and C-pyri-NH (in acid) sites. (a) Atomic models of C-pyri-N in alkaline medium and protonated pyridinic N in acid medium. The white, gray and blue balls represent H, C and N atoms, respectively. (b) Free energy diagrams of O_2 reduction through the $4e^-$ associative pathway on C-pyri-N and C-pyri-NH sites.

7.2.5 Discussions

The RDE results in Figure 6.4 revealed that ORR would mainly proceed through a $4e^-$ pathway (3.3 electron transfer) on the FeNC catalyst whereas mainly through a $2e^-$ pathway (2.5 electron transfer) on the pyrolyzed CoNC catalyst. Furthermore, the RRDE measurements in Figure 6.6 confirmed the generation of H_2O_2 during the ORR on the pyrolyzed CoNC nanofibers. In consistent with these experimental results, the DFT results in Figure 7.9 suggested that the $4e^-$ ORR associative pathway could be activated on the FeN_4 active site. Regarding the ORR on the CoN_4 site, the DFT calculations predicted that the $4e^-$ associative pathway requires high activation energy (1.11 eV) for the OOH dissociation reaction and hence could be kinetically difficult to occur. Instead, the alternative OOH protonation reaction to form H_2O_2 could proceed on the CoN_4 site. The results in Table 7.3 further show extremely weak adsorption of H_2O_2 on the CoN_4. Consequently, the DFT calculations also predicted that the ORR might most possibly proceed to the formation and desorption of H_2O_2 and thus give a $2e^-$ pathway on the CoN_4 site.

To date, the exact chemistry of the active sites is not known for ORR on the pyrolyzed TM-N-C catalysts in acidic medium. In this section, it was proposed that the planar TM-N_4 clusters embedded in carbon matrix are the active sites to promote the ORR in the pyrolyzed TM-N-C catalysts. The electrochemical measurements show that the pyrolyzed FeNC and CoNC fibers exhibit catalytic activity for ORR whereas the pyrolyzed PAN fibers synthesized in the same way does not. The XPS characterization results indicate that species TM-N_x exist on the surface of the pyrolyzed FeNC and CoNC fibers but not on the pyrolyzed PAN fibers. Consequently, it could be inferred that some type of the TM-N_x clusters embedded in carbon support is the active sites for ORR on the pyrolyzed TM-N-C catalysts. Moreover, the model (Figure 7.7) explains well the observed ORR activity of the pyrolyzed FeNC and CoNC catalysts. Therefore, it deserves further investigations with advanced characterization techniques to examine if the planar TM-N_4 clusters are truly the active sites for ORR in pyrolyzed TM-N-C catalysts. The study in Section 7.1 on TM-N_4 macrocyclic molecules have revealed that the catalytic activity of the TM-N_4 clusters for ORR could be optimized by tuning the non-bonding d orbital levels of the central transition metal atom through varying

the TM element or peripheral groups. These knowledge could help us to rationally design the chemistry of TM-N_4 active sites and optimize the performance of pyrolyzed TM-N-C catalysts for ORR.

7.3 ORR ON TM-N-C CATALYSTS: EFFECT OF CARBON STRUCTURE

7.3.1 Model of active sites

Several models involving FeN_4 moieties embedded in carbon have been proposed to explain the activity of the Fe-N-C catalysts for ORR in acid [93, 99]. In Section 7.2.3, it was predicted that the four-electron OOH dissociation pathway is both thermodynamically and kinetically favorable on the FeN_4 site embedded in an otherwise intact graphitic layer and surrounded by ten carbon atoms (denoted as FeN_4-C_{10}, Figure 7.11a). In this section, this FeN_4-C_{10} site was used to study the ORR activity of the Fe-N-C catalysts in the region far away from micropores. Regarding the active sites hosted by micropores, there are two models: one is FeN_4-C_{12} site (Figure 7.11b) near mircopores and with a FeN_4 moiety bridging two adjacent zigzag graphitic edges with a porphyrin-like architecture, and the other is FeN_4-C_8 site (Figure 7.11c) on the edge of micropores and with a FeN_4 moiety bridging two adjacent armchair-like graphitic edges. It is noted that FeN_4-C_{12} was identified as the primary active site in the Fe-N-C catalysts by Jaouen *et. al.* from their analysis of X-ray absorption near edge structure (XANES) results [74], whereas FeN_4-C_8 was proposed to be the ORR active site by Dodelet *et. al.* based on X-ray photoelectron and diffraction characterization results [17, 62]. Recent XANES studies indicated that the catalytic activity of the Fe-N-C catalysts varied with the amount of the three different types of FeN_4 moieties in the sample [70, 74, 181].

7.3.2 Adsorption energy

The adsorption energies of the ORR species (O_2, OOH, O, OH and H_2O) on the three FeN_4-type active sites were calculated. It should be emphasized that, for each ORR species, there

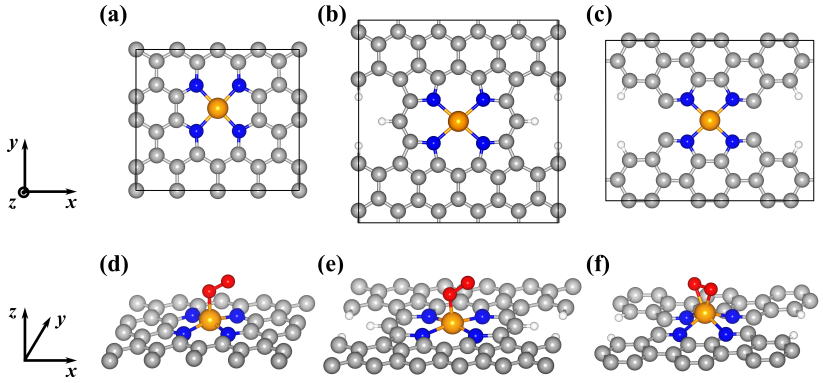

Figure 7.11: Atomistic structures of ORR active site (a) FeN_4-C_{10}, (b) FeN_4-C_{12}, (c) FeN_4-C_8, and O_2 adsorption with (d) an end-on configuration on FeN_4-C_{10}, (e) an end-on configuration on FeN_4-C_{12}, (f) a side-on configuration on FeN_4-C_8. In the figure, the gray, blue, orange, red, and white balls represent C, N, Fe, O, and H atoms, respectively.

are several different adsorption configurations on the FeN_4-type active site (Appendix A). The most stable adsorption configuration (Figure 7.12) was located for each adsorption system. Correspondingly, the predicted lowest adsorption energy is reported in Table 7.5.

Figures 7.11d-f show the optimized atomistic structures of the lowest-energy configuration of the adsorption of O_2 on FeN_4-C_{10}, FeN_4-C_{12}, and FeN_4-C_8 sites, respectively. It can be seen that O_2 adopts an end-on adsorption configuration with bent Fe-O-O geometry on FeN_4-C_{10} and FeN_4-C_{12}, whereas a side-on adsorption configuration with O-O lying along the N-Fe-N bonding direction on FeN_4-C_8. The DFT calculations predicted that the adsorption energy for O_2 is -0.63 eV on FeN_4-C_{12}, -0.95 eV on FeN_4-C_{10}, and -1.67 eV on FeN_4-C_8, suggesting a trend that the binding strength of O_2 to the FeN_4-type active sites becomes stronger with less number of local carbon atoms around FeN_4 moiety. Indeed, it was found that the Fe-O bonding orbital in the O_2-FeN_4-C_8 adsorption system was much deeper below the Fermi energy than those of the O_2 adsorption on the other two FeN_4 sites surrounded by more carbon atoms (Figure D1 in Appendix D). These predicted O_2 adsorption energies are also found to be comparable to those predicted for O_2 on Pt catalysts (-0.69 eV on Pt(111) [80] and -1.10 eV on Pt(100) [156]. Moreover, the DFT results in Table 7.5 indicate that the

Table 7.5: Predicted adsorption energies of various ORR species on the three FeN_4 active sites. Negative value of adsorption energy indicates attractive interaction between the ORR species and ORR active sites.

ΔE_{ad} (eV)	FeN_4-C_{10}	FeN_4-C_{12}	FeN_4-C_8
O_2	-0.95	-0.63	-1.67
OOH	-1.71	-1.41	-1.97
O	-4.12	-3.89	-4.37
OH	-2.69	-2.38	-2.83
H_2O	-0.13	-0.27	-0.21

binding of H_2O on the FeN_4-type active sites is all weaker than the solvation stabilization energy of bulk water about 0.40 eV. Consequently, it was predicted here that FeN_4-C_{10}, FeN_4-C_{12}, and FeN_4-C_8 active sites are able to attract reactant O_2 to initiate the ORR as well as release product H_2O to complete the ORR.

7.3.3 Free energy landscape

Following four-electron pathways of ORR, the O-O bond in the adsorbed O_2 must be broken through either the direct dissociation of O_2 or the dissociation of OOH which is after O_2 is protonated. It is noted that this O-O bond breaking process is not influenced by the external electrode potential. Table 7.6 lists calculated activation energies for the two types of O-O bond breaking reactions (O_2 *vs.* OOH) on the three FeN_4-type active sites. The results show that the activation energy for the direct O_2 dissociation reaction is always higher than that for the OOH dissociation reaction on the FeN_4 sites. It is thus inferred that the OOH dissociation pathway would be kinetically more feasible than the O_2 dissociation pathways for ORR on the FeN_4-type active sites.

The calculation results in Table 7.6 also indicate that the OOH dissociation reaction on FeN_4-C_8 requires an activation energy of only 0.20 eV which is appreciably lower by at least

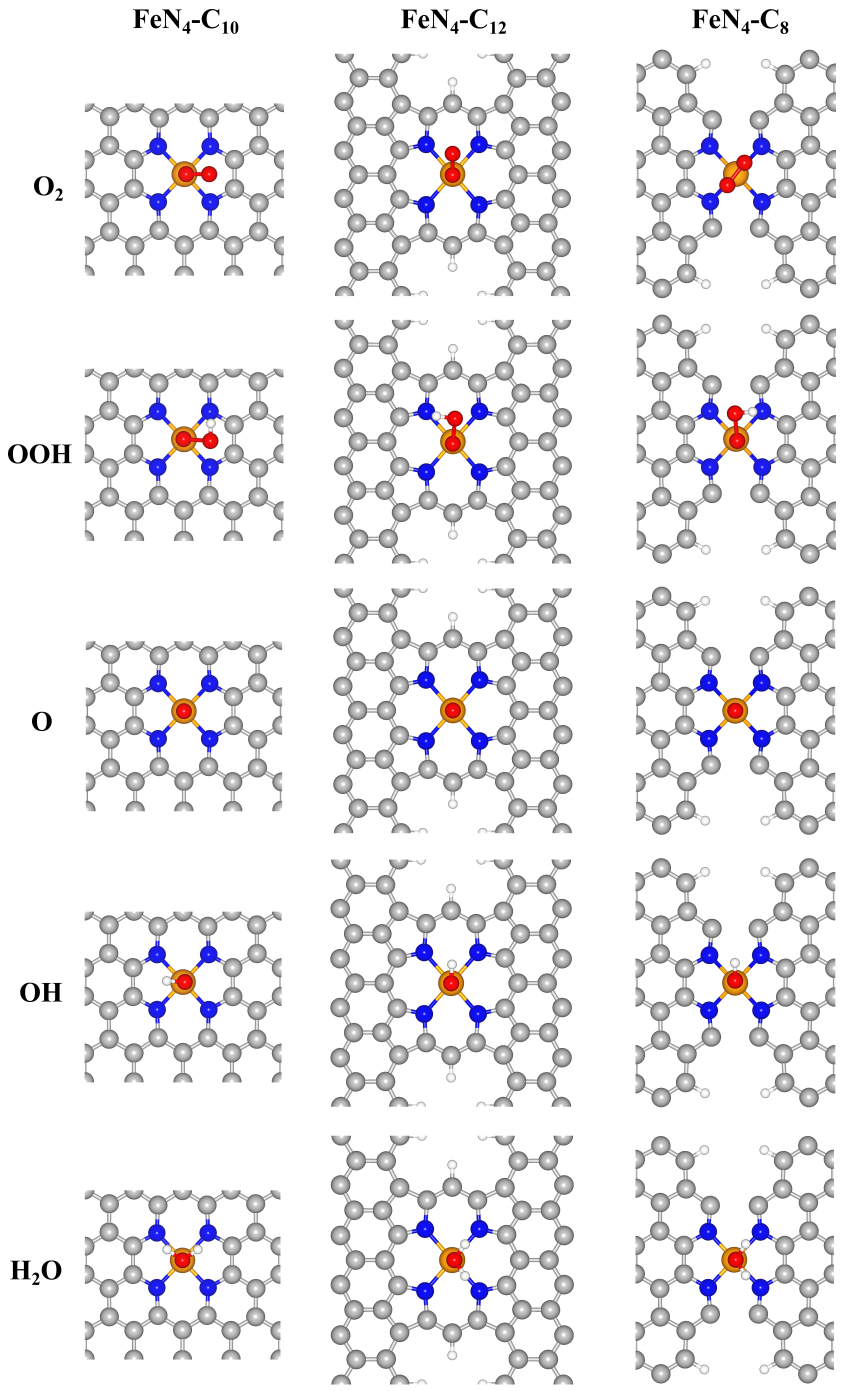

Figure 7.12: Atomistic structures of the optimized configurations of various ORR species adsorbed on the three FeN_4-type active sites. Column 1-3: FeN_4-C_{10}, FeN_4-C_{12}, and FeN_4-C_8; Row 1-5: O_2, OOH, O, OH, and H_2O. In this figure, the gray, blue, orange, red, and white balls represent C, N, Fe, O, and H atoms, respectively.

0.36 eV than those on the other two FeN_4-type active sites. In addition, it was found that the central Fe of FeN_4-C_8 is fully capable of breaking the OOH molecule into O and OH on itself (Figure 7.13c). In contrast, the OOH dissociation reaction on both FeN_4-C_{10} and FeN_4-C_{12} is predicted to require the transportation of product OH to the top of adjacent carbon (Figure 7.13a-b). Consequently, the DFT calculations predicted the O-O bond breaking of ORR is fairly easier on FeN_4-C_8 than on FeN_4-C_{10} and FeN_4-C_{12} sites, apparently relating to the relatively stronger O_2 adsorption on FeN_4-C_8 than the other sites.

Table 7.6: Calculated activation energies for O_2 dissociation and OOH dissociation on the FeN_4 active sites.

E_a (eV)	FeN_4-C_{10}	FeN_4-C_{12}	FeN_4-C_8
O_2 dissociation	1.19	1.39	0.94
OOH dissociation	0.56	0.72	0.20

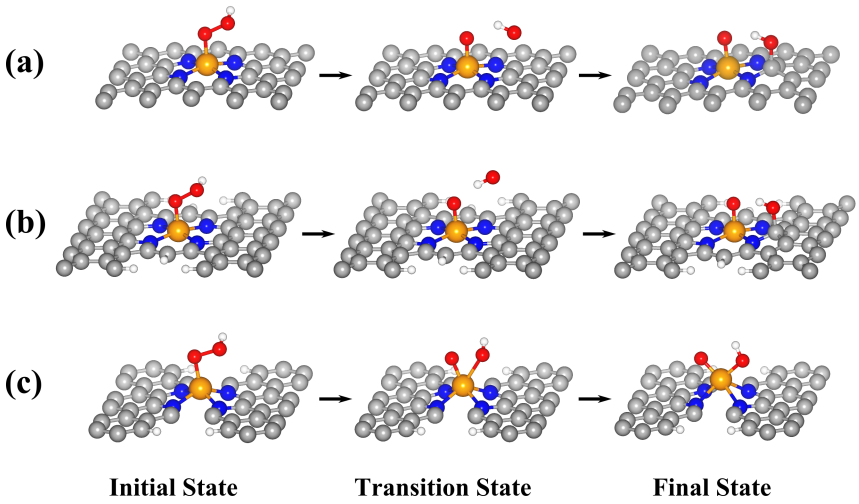

Figure 7.13: Atomistic structures of the initial state, transition state, and final state for OOH dissociation reaction on (a) FeN_4-C_{10}, (b) FeN_4-C_{12}, and (c) FeN_4-C_8 active sites. In the figure, the gray, blue, yellow, red, and white balls represent C, N, Fe, O, and H atoms, respectively.

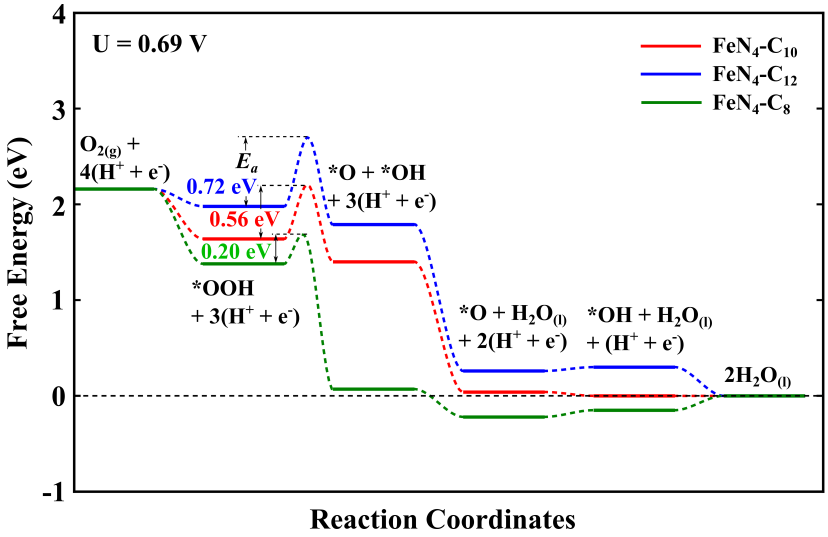

Figure 7.14: Calculated free energy evolution diagrams for the O_2 reduction through an OOH dissociation pathway on active site FeN_4-C_{10}, FeN_4-C_{12} and FeN_4-C_8 at temperature of 300 K and under electrode potential of 0.69 V in acid medium.

Besides the potential-independent O-O bond breaking reaction, the four-electron pathways of ORR include several protonation reactions (such as, O_2 protonation, OH protonation, and O protonation) whose activation energies vary with external electrode potential. The free energy evolution following the OOH dissociation ORR pathway on the three FeN_4-type active sites was calculated to examining this effect of electrode potential on ORR. The results indicate that all the elementary ORR reactions will be exergonic and thus thermodynamically favorable below a limiting electrode potential whereas some reactions involving charge-transfer will become endergonic above this limiting electrode potential. Figure 7.14 plots the free energy evolution for ORR under an electrode potential of 0.69 V. It can be seen that under this electrode potential the last OH protonation reaction has a zero change in free energy, but all the other ORR steps are still exergonic on FeN_4-C_{10}. Consequently, the thermodynamic limiting potential for ORR on FeN_4-C_{10} is 0.69 V. Figure 7.14 also shows that, under 0.69 V, the O protonation reaction requires an increase in free energy by 0.04 eV on FeN_4-C_{12} and the OH protonation reaction has an increase in free energy by 0.15 eV

on FeN_4-C_8. Thus, the thermodynamic limiting potential for ORR is 0.65 V and 0.54 V on FeN_4-C_{12} and FeN_4-C_8 sites, respectively. It should be pointed out that the predictions on the ORR limiting potential for the three FeN_4-type active sites are close to previous theoretical prediction of 0.64 V for FeN_4 cluster [182].

Therefore, the DFT calculations predicted that, although all the three FeN_4-type active sites are able to catalyze the four-electron ORR under their respective thermodynamic limiting electrode potentials, the OOH dissociation pathway requires the lowest activation energy (about 0.20 eV) on FeN_4-C_8 which lies on the edge of micropores in graphitic layer whereas the highest activation energy (about 0.72 eV) on FeN_4-C_{12} which has a porphyrin-like structure. These theoretical predictions agree well with previous experimental finding that the Fe-N-C catalysts containing the FeN_4-C_{10} and/or FeN_4-C_8 moieties exhibited enhanced catalytic activity for ORR than the sample containing mainly the porphyrin-like FeN_4-C_{12} moieties [181].

7.3.4 Electronic structure

In order to understand the predicted local carbon structure-dependent ORR activity, the geometric and electronic structures of the three FeN_4-type active sites were further analyzed. All the three FeN_4 moieties were found to have a planar structure embedded in a graphene layer and with a nearly square ligand field (as shown in Figure 7.11a-c). In their fully optimized structures, the lengths of Fe-N bond in FeN_4-C_{10} and FeN_4-C_8 are calculated to be 1.90 Å, which is about 6 % shorter than the Fe-N bond length of 2.02 Å in FeN_4-C_{12}. It notes that the Fe-N bond length in FeN_4-C_{12} site is very close to 1.99 Å predicted for isolated Fe-porphyrin molecule in Section 7.1.1. In such a square, planar ligand field of FeN_4 moieties [144], the $3d_{xy}$, $4s$, $4p_x$, and $4p_y$ orbitals of the central Fe would participate in the formation of four Fe-N bonding orbitals with the hybrid $2p$ orbitals of the surrounding N, whereas the other four $3d$ orbitals ($d_{x^2-y^2}$, d_{yz}, d_{yz}, and d_{z^2}) of Fe would transform into four non-bonding d-type orbitals and interact with the electronic orbitals of adsorbates. Illustrating this point, Figure 7.15 plots the partial density of states (pDOS) for the elements

in the three FeN_4 active sites. It can be seen in the upper panels of Figure 7.15 that N $2p$ orbitals mainly overlap Fe $3d_{xy}$ orbital to form the Fe-N bonds in the clean FeN_4 active sites.

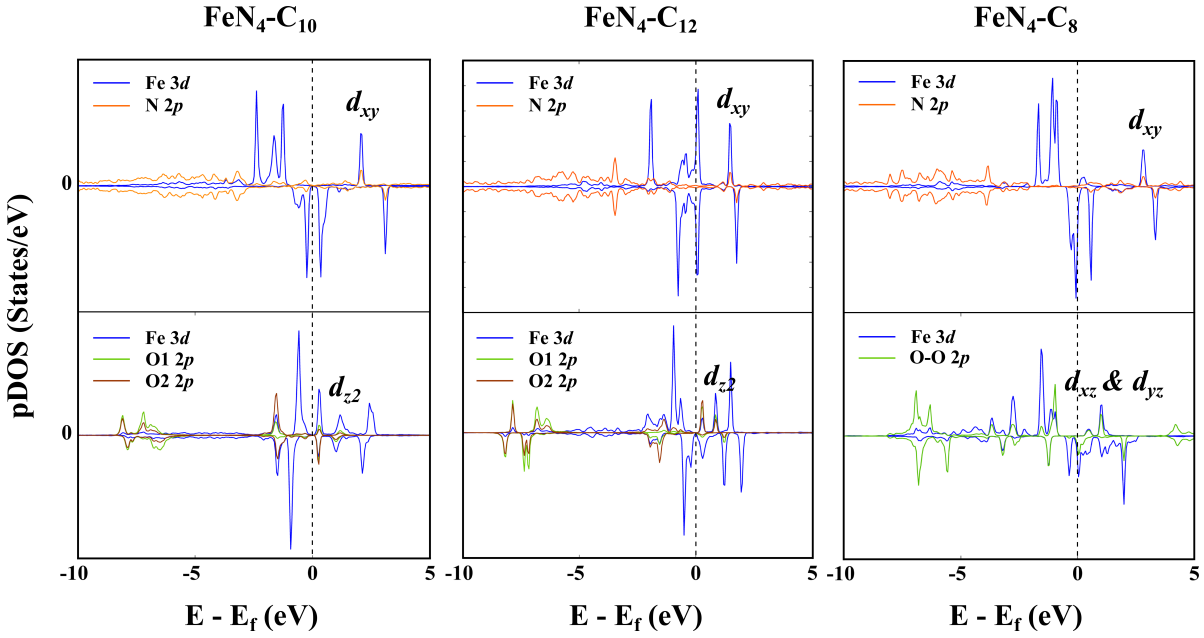

Figure 7.15: Calculated partial density of states (pDOS) for Fe, N, and O in the relaxed FeN_4-C_{10}, FeN_4-C_{12} and FeN_4-C_8 sites (upper panels) and the adsorption of O_2 molecule on these three FeN_4type active sites (lower panels). In the lower panels, O1 refers to the O atom close to the Fe atom whereas O2 refers to the other O atom away from the Fe atom in an end-on O_2 adsorption configuration; the two O atoms are equivalent in a side-on O_2 adsorption configuration.

More interestingly, it can be observed in the lower panels of Figure 7.15 that the $2p$ orbitals of O_2 mainly overlap with the $3d_{z^2}$ orbital of the central Fe when O_2 adsorbed with an end-on adsorption configuration on FeN_4-C_{10} and FeN_4-C_{12}, but overlap with the $3d_{xz}$ and/or $3d_{yz}$ orbitals of the central Fe when O_2 adsorbed with a side-on adsorption configuration on FeN_4-C_8. The results of the decomposed pDOS (Figure D2 in Appendix D) show that the Fe $3d_{z^2}$ orbital is close to the Fermi energy in FeN_4-C_{10} and FeN_4-C_{12} whereas the Fe $3d_{xz}$ and/or $3d_{yz}$ are near the Fermi energy in FeN_4-C_8. Hence, it appears that the

orientation of the Fe non-bonding *d*-type orbitals near their Fermi energy affects the binding strength and adsorption configuration of O_2 (or other ORR species) on the FeN_4 active sites.

Furthermore, the binding strength and optimized configurations of OOH adsorption affect the activation energy for O-O bond breaking on the FeN_4 active sites. The DFT calculations predicted that the adsorbed OOH binds to FeN_4-C_8 the most strongly among the three FeN_4 sites (see results in Table 7.5) and adopts a configuration with the two O atoms nearly parallel to the graphene plane (the angle O-O-Fe is about 100° in Figure 7.13c). As a result, it was found that the O-O bond in the adsorbed OOH (with initial bond length of 1.48 Å) can be broken fairly easily (with an activation energy of 0.20 eV and final O-O separation of 2.53 Å) on the central Fe atom of FeN_4-C_8, which is thus predicted to possess enhanced ORR activity than other possible active sites. This result confirms the previous proposal that the side-on adsorption configuration of O_2 and OOH would favor easy O-O bond scission on FeN_4 macrocyclic complexes [85, 86].

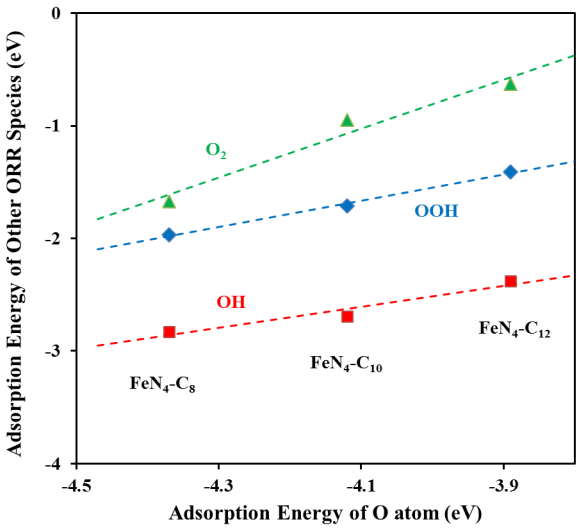

Figure 7.16: Linear scaling relation of the calculated adsorption energy of ORR species (O_2, OOH, and OH) with respect to the calculated adsorption energy of O atom on different FeN_4-type active sites.

Comparing the calculated binding strength of various ORR species on the three FeN_4type active sites, it was established a linear scaling relation between the adsorption energy of

ORR species and the number of local carbon atoms immediately adjacent to FeN_4 moiety (Figure 7.16). The finding here is in support of previous proposition that the position of the non-bonding Fe $3d$ orbitals could be tuned by the degree of π-electron delocalization on the carbon plane with sp^2-hybridized graphitic carbon atoms and is related to the adsorption energy of ORR species [68]. In this section, it was found that the less number of local carbon atoms around a FeN_4 moiety (*i.e.*, the FeN_4-C_8 on the edge of micropores) results in Fe $3d_{xz}$ and/or $3d_{yz}$ orbital near to the Fermi energy, strong binding of ORR species, easy O-O bond breaking, and thus enhanced ORR activity.

7.3.5 Microkinetic analysis

In order to interpret the catalytic activity easily with the predicted polarization curves of FeN_4 active sites, microkinetic analysis was performed using the calculated energy parameters in section 7.3.3. Some previous studies [102, 183] also included water in the DFT models to get more accurate energy parameters since the ORR intermediates are stablized by interacting with water molecules via hydrogen bonds. In order to evaluate the effect of water layer, the energy parameters for ORR on FeN_4-C_{10} with a water layer above the catalytic surface were calculated (Figure 7.17a shows the OOH adsorption on FeN_4-C_{10} covered by a water layer). The water layer consists of a two-dimensional hexagonal ice-like hydrogen bond network with half of water molecules lying parallel to the carbon sheet and the other half with one hydrogen pointing to the carbon sheet, similar to that on Pt(111) surface reported before [102, 183]. The ORR on Pt(111) surface was also investigated as a catalytic benchmark for microkinetic analysis since the predicted polarization curves may not reproduce the experiment results. The energy parameters for ORR on Pt(111) were calculated using a $2 \times \sqrt{3}$ rectangular slab model including a water layer (Figure 7.17b shows the OOH adsorption on Pt(111) covered by a water layer). The calculated free energy diagram including the activation energy for OOH dissociation through the associative mechanism on both FeN_4-C_{10} and Pt(111) surfaces are shown in Figure 7.17c.

It can be observed that the ORR intermediates on FeN_4-C_{10} are stablized by the added water layer that the OOH dissociation has an energy barrier of 0.42 eV which is 0.14 eV

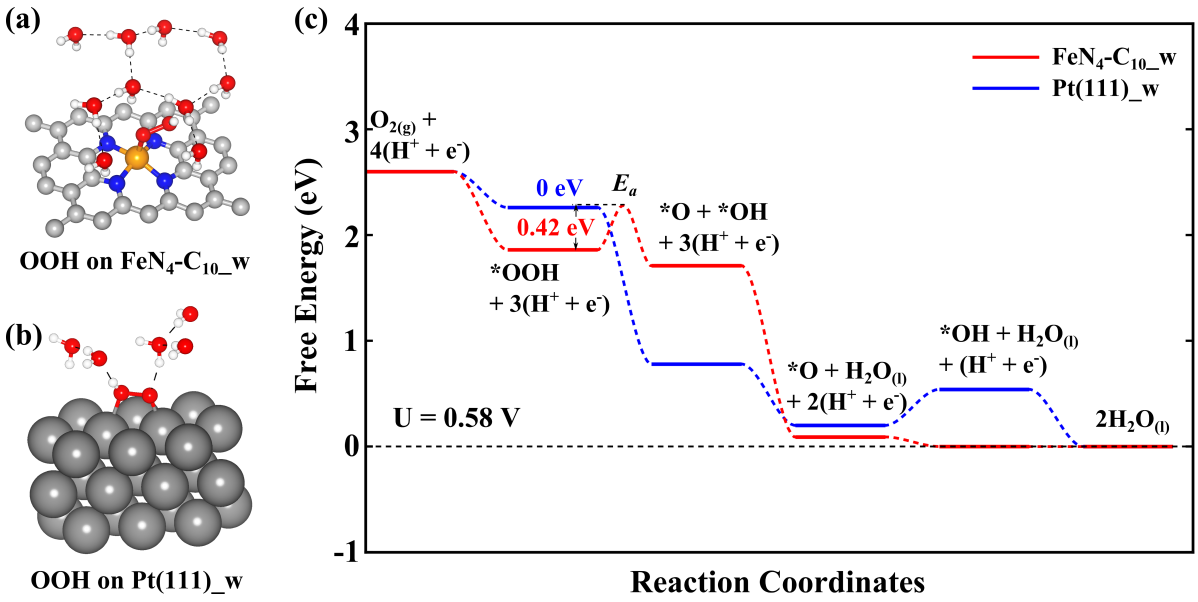

Figure 7.17: Free energy diagram for ORR on FeN_4-C_{10} and Pt(111) surface with a water bilayer. (a) OOH adsorption on FeN_4-C_{10}; (b) OOH adsorption on Pt(111); and (c) free energy diagram for ORR under electrode potential of 0.58 V in acid medium. In this figure, the gray, blue, orange, red, white, and dark gray balls represent C, N, Fe, O, H, and Pt atoms, respectively.

lower than that without a water layer. Moreover the adsorbed OH is also stabalized that the limiting potential (by the OH protonation reaction) is lowered from 0.69 V (Figure 7.14) to 0.58 V (Figure 7.17). For ORR on Pt(111) surface, the OOH dissociation is barrier free close to the previously reported low energy barrier of 0.05 eV calculated in vacuum [80]. However, the O protonation reaction is still endergonic at 0.58 V which is thermodynamically unfavorable suggesting that the protonation of O is the limiting step. In the previous study [80], an extremely high activation energy barrier of 0.79 eV for O hydrogenation on Pt(111) surface was obtained by DFT calculation. Therefore, the O protonation is the rate determining step for ORR on Pt(111) surface in either thermodynamic or kinetic perspective.

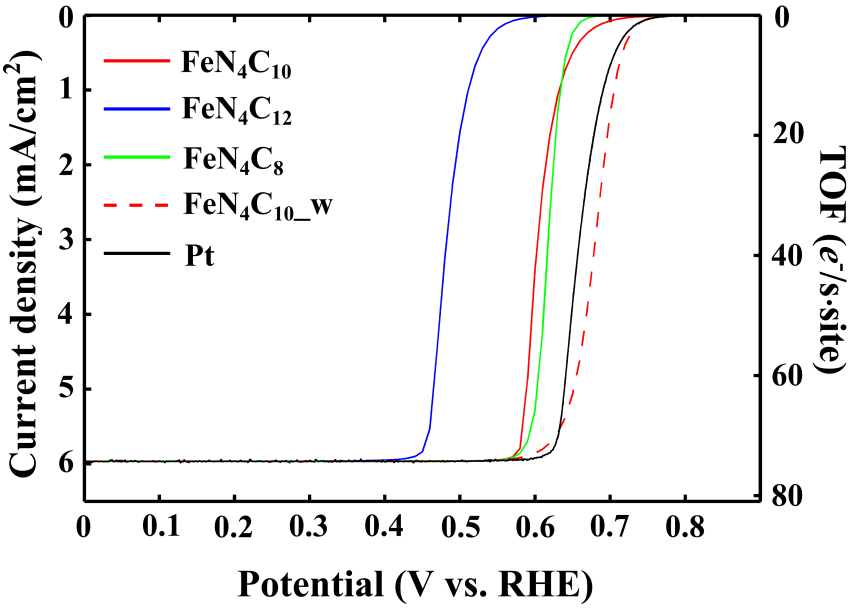

Figure 7.18: Simulated polarization curves on FeN_4-C_{10} (with and without a water layer), FeN_4-C_{12}, and FeN_4-C_8 at 1600 rpm rotation speed. Previous simulated polarization curves on Pt(111) [102] are shown for comparison.

Figure 7.18a shows the predicted polarization curves for ORR on the three FeN_4 active sites using the calculated energy parameters in section 7.3.3 comparing with that on water-layer covered FeN_4-C_{10} and Pt(111) surface. The Pt(111) surface is predicted to catalyze ORR with a half-wave potential of 0.66 V while an experimental value of 0.85 V was reported before [184]. As a result, the prediction is assumed to underestimate the half-wave potential

by 0.19 V. For ORR on the three FeN_4 active sites, the half-wave potentials are predicted to be 0.48 V (FeN_4-C_{12}), 0.60 V (FeN_4-C_{10}), and 0.62 V (FeN_4-C_8) respectively, indicating the catalytic activity trend is the same as analyzed based upon the free energy diagram. With a water layer added on the FeN_4-C_{10} site, the predited half-wave potential is improved to be 0.68 V, which is even higher than that for Pt(111). The predicted polarization curves suggest that both the FeN_4-C_{10} and FeN_4-C_8 active sites can exhibit catalytic activity close to that of platinum. Moreover, the inclusion of water above the catalytic surface in the DFT models can stabilize the ORR intermediates on the active sites, thus improving the microkinetic predictions.

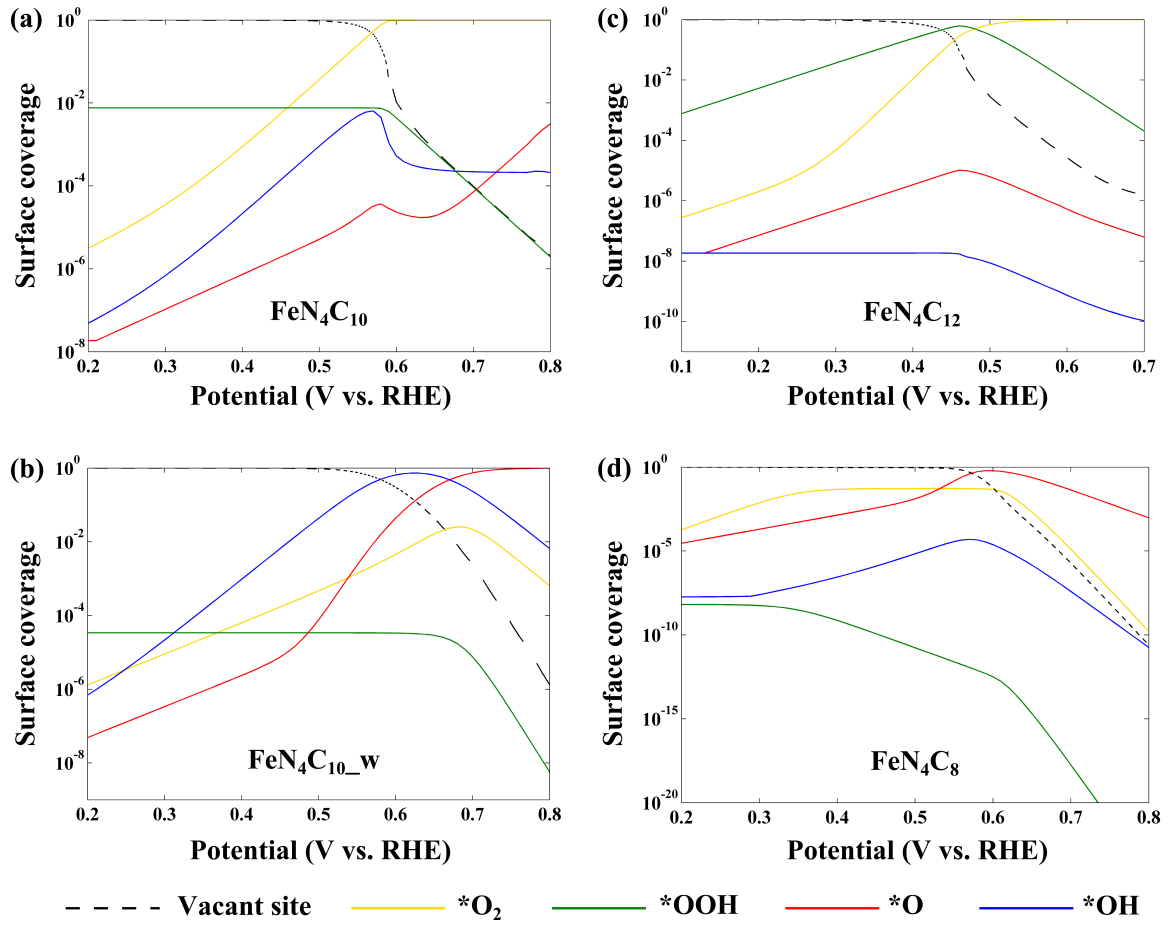

Figure 7.19: Surface coverage of ORR intermediates vs. electrode potential U on FeN_4-C_{10} (a), FeN_4-C_{10} with a water layer (b), FeN_4-C_{12} (c), and FeN_4-C_8 (d) at steady states.

The calculated coverage of each intermediate on the three FeN_4 active sites over the ORR potential range is shown in Figure 7.19. It can be observed that the O_2 is the major intermediate occupying the FeN_4-C_{10} and FeN_4-C_{12} sites under the high potential range, indicating that the first protonation step is the limiting step. After a water layer is added over the FeN_4-C_{10} site, the O_2 can be protonated easily since OOH is stablized and the subseqent O and OH protonation reactions become the limiting steps. Therefore, it can be observed that the major surface species becomes O on FeN_4-C_{10} with a covered water layer and changes to OH as the electrode potential decreases. FeN_4-C_8 active site has relatively high binding energy with ORR intermediates so that the O_2 protonation is initiated easily while the reaction is stuck at O protonation under high electrode potentials.

7.3.6 Discussions

The investigation on the local carbon structures around the FeN_4 active sites shows that the peripheral structure can also affect the catalytic activity through tuning the electronic structure of the active site indirectly. This finding allows researchers to improve the TM-N-C catalysts not only through optimizing the transition metal and nitrogen precursors, but also through tailoring the carbon matrix. The calculation results suggest that the $3d_{xz}$ and/or $3d_{yz}$ orbitals are located around the Fermi level when introducing micropores adjacent to the FeN_4 center, thus resulting in a side-on configuration for O_2 and strong binding for ORR intermediates. It is shown that the activity of FeN_4 site is enhanced if the binding strength becomes stronger. It has been reported that the chemical doping of Fe ions into zeolitic imidazolate framework networks followed by one-step thermal activation can introduce rich micropores and enhance the catalytic performance [185]. Moreover, the calculation result also suggests that for those transition metal dopings with too strong binding strength, creating a porphyrin-like architechture may improve the activity since it may tune down the binding strength.

8.0 CONCLUSIONS AND PROSPECTS

8.1 CONCLUSIONS

In summary, the electrocatalytic activity of non-precious transition metal TM (TM=Fe and Co)/nitrogen doped carbon catalysts for ORR in acid and alkaline medium has been investigated using the electrochemical experiments and DFT calculations. In the experimental part, the non-precious TM-N-C catalysts were synthesized by electrospinning a mixture of TMPc and PAN into nanofibers, and subsequently heat-treating the nanofibers in N_2 atmosphere. The synthesized non-precious Fe-N-C catalyst exhibits an ORR activity higher than the Co-N-C catalyst, but appreciably lower than Pt catalyst in terms of mass activity. Moreover, the electrochemical measurements indicate that the pyrolyzed Fe-N-C catalyst promotes mainly $4e^-$ ORR whereas the pyrolyzed Co-N-C catalyst promotes mainly $2e^-$ ORR in acid medium. While in alkaline electrolyte, both the Fe-N-C and Co-N-C catalysts exhibit higher catalytic activity.

For the computational investigations, the molecular and electronic structures of TM macrocyclic complexes and the adsorption of O_2 molecule on these complexes were studied first by the DFT calculation method. The investigated TM macrocyclic complexes include CrP, MnP, FeP, FeTPP, CoP, CoTPP, NiP, CrPc, MnPc, FePc, $FePcF_{16}$, $FePcCl_{16}$, CoPc, $CoPcF_{16}$, $CoPcCl_{16}$, and NiPc molecules, all being predicted to have the planar TM-N_4 chelation structures. The DFT calculations revealed that the origin of the O_2 adsorption on the TM macrocyclic complexes is the interaction between the π^* anti-bonding orbitals of O_2 with the non-bonding d-type orbitals of the TM macrocyclic complexes. Hence, the energy levels of these non-bonding d orbitals (orbital a_{1g} (d_{z^2}), orbital b_{2g} (d_{xy}), and orbitals e_g (d_{xz} and d_{yz})) of the TM macrocyclic complexes are found to be pertinent to the binding strength

of O_2 molecule. Specifically, a linear relation has been established between the adsorption energy of O_2 and the non-bonding d orbitals center (defined as the average energy of the non-bonding d orbitals with respect to the LUMO energy level) of the TM macrocyclic molecule. On the other hand, the adsorption energy of O_2 on the catalysts can be regarded as a simple parameter indicating the activity of the catalysts for ORR. An optimal ORR catalyst should bind O_2 molecule neither too strongly nor too weakly. Consequently, the catalytic activity of the TM macrocyclic complexes for ORR should be closely related to the energy levels of the non-bonding d-electron orbitals of their central TM atoms.

Furthermore, the first-principles DFT calculations were performed using the planar TM-N_4 (i.e., FeN_4 and CoN_4) clusters embedded in monolayer graphene models. The DFT calculations demonstrate that the FeN_4 and CoN_4 active sites are energetically favorable to be formed and the theoretical predictions with respect to the ORR pathways are in consistence with the experimental observations. In particular, the DFT calculations predict that it is thermodynamically and kinetically feasible for the ORR to proceed following the $4e^-$ associative pathway on the planar FeN_4 active sites in agreement with the electrochemical measurements showing that the pyrolyzed Fe-N-C catalyst promotes $4e^-$ ORR. The DFT results also indicate that the O-O bond scission on the CoN_4 active site requires rather high activation energy no matter through the dissociative mechanism or the associative mechanism. Hence, the $4e^-$ ORR pathway on the CoN_4 active site is kinetically sluggish. Alternatively, the OOH could undergo a protonation reaction on the CoN_4 and form H_2O_2 which can easily be desorbed from the active sites. Thus, the theoretical studies suggest that the CoN_4 active sites could favorably promote $2e^-$ ORR. Consistent with the calculation results, the electrochemical measurements show that the pyrolyzed Co-N-C nanofibers promote the ORR mainly through a $2e^-$ pathway with the production of H_2O_2. Moreover, the DFT calculations were performed to predict the free energy evolution of ORR on the C-pyri-N active sites. The DFT calculation results revealed that the protonation of pyridinic nitrogen can cause ORR activity loss on the C-pyri-NH active sites. This theoretical prediction explains the observed inferior activity of the TM-N-C catalysts in acid versus in alkaline.

The effect of local carbon structures on the catalytic activity of the FeN_4 active sites was also investigated. The adsorption energies of ORR species, activation energy for O-O bond breaking, and free-energy evolution of ORR on three FeN_4-type moieties with different local carbon structures were calculated. The results showed that the FeN_4-C_8 sites hosted by micropores could favorably promote the four-electron ORR below a limiting electrode potential of 0.54 V and break the O-O bond in the adsorbed OOH with a pretty low activation energy of 0.20 eV. Microkinetic analysis was also performed to generate the polarization curves for ORR on the FeN_4 active sites based upon the calculated energy parameters. The predicted half-wave potential of FeN_4-C_8 is higher than that of FeN_4-C_{10} active site and close to that of Pt(111) surface. Consequently, the theoretical study suggests that introduction of micropores in the non-precious Fe-N-C catalysts could enhance their intrinsic catalytic activity for ORR through generating the FeN_4-C_8 active sites with high specific activity. All in all, the combination of experimental and computational study provides useful guidance to the rational design and controlled synthesis of non-precious metal and nitrogen derived carbon electrocatalysts.

8.2 PROSPECTS

Current experimental and computational studies shed some light on the ORR catalyzing mechanism of novel TM-N-C catalysts. With understanding of the structural and electronic effects on the catalytic activity, researchers can play with many synthesis parameters. For example, other transtion metal elements, such as manganese, are worth investigation since it has moderate interaction with ORR species according to the calculation result in section 7.1. In some recent study, manganese has been reported as a promising transition metal candidate for synthesizing TM-N-C catalysts [186] since it exhibits outstanding activity and enhanced stability. On the other hand, adopting metal organic framework enables the creation of well-dispersed atomic Fe sites embedded into porous carbon exhibiting improved catalytic activity [185]. The calculation results in section 7.3 suggest this enhancement comes not

only from the increasing of the surface area but also from improving the specific activity of the active sites. These advances provide new research directions in developing more effecient and more stable TM-N-C catalysts.

There are still a lot of challenges in the TM-N-C catalysts development, especially in the computational modelling. One of the biggest challenges is that it is difficult to compare the DFT calculated energy parameters, such as free energy and activation energy, with the experiment measured current-voltage curves directly. The present study in this thesis demonstrates that microkinetic model could be a useful tool to connect the gap between the compuational and experimental studies. However, it is difficult to reproduce the polarization curves perfectly using the microkinetic analysis and the deviations could be caused by any links involved in the model. For example, the DFT calculation of the energy parameters is worth further improvement and more accurate functionals needs to be developed specifically for the heterogeneous catalyst study. Moreover, advanced models are necessary to describe the electrode-electrolyte interface, especially the solvation effect and the double layer accurately. Furthermore, the modelling of electron transfer coupled surface reaction processes (such as protonation reactions) is difficult thus it demands new techniques to calculate the potential dependent activation energy of these reaction steps. The future advances of these techniques can not only promote the development of non-precious catalyst for ORR, but also facilitate the research of other heterogeneous catalysis systems.

APPENDIX A

EXAMINED ADSORPTION CONFIGURATIONS FOR ORR SPECIES

For O_2, OOH, O, OH adsorption, only the central Fe was considered as the adsorption site. The examined adsorption configurations along those high symmetric directions of TM-N_4-C_x (FeN_4-C_{12} as an example) are listed in Figure A1.

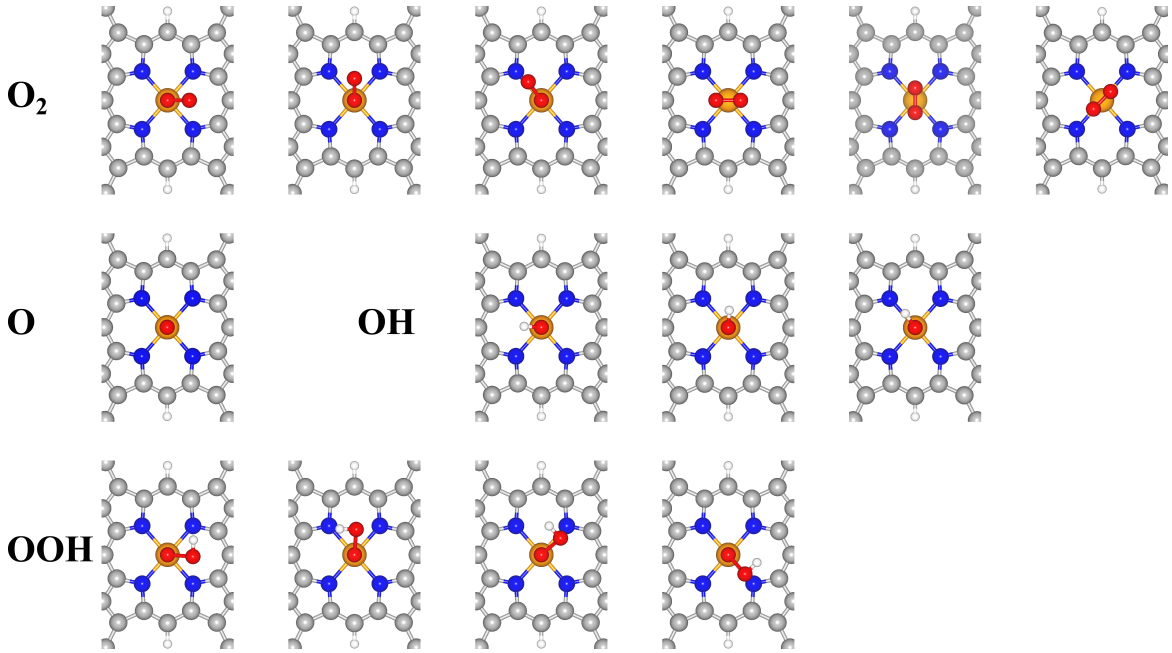

Figure A1: Atomistic structures of investigated possible adsorption configurations for O_2, OOH, O, OH on FeN_4-C_{12}. In this figure, the gray, blue, orange, red, and white balls represent C, N, Fe, O, and H atoms, respectively.

APPENDIX B

ELEMENTARY STEPS, RATE EQUATIONS, AND PARAMETERS IN MICROKINETIC MODEL

The elementary steps with their reaction rates in the microkinetic model are listed below. In these equations, * represents the active site; x and θ refer to mole fraction and surface concentration respectively; r is the net reaction rate; k_+ and k_- are forward and backward reaction rate constant.

Initially, the dissolved O_2 molecules diffuse from the bulk electrolyte to the catalyst-electrolyte interface (i.e. double layer)

$$O_{2(aq)} \leftrightarrow O_{2(dl)}, r_1 = k_{+1} x_{O_{2(aq)}} - k_{-1} x_{O_{2(dl)}} \tag{B.1}$$

Then the O_2 molecule in the double layer is adsorbed on the vacant active site

$$O_{2(dl)} + * \leftrightarrow *O_2, r_2 = k_{+2} x_{O_{2(dl)}} \theta_* - k_{-2} \theta_{O_2} \tag{B.2}$$

Once adsorbed on the active site, O_2 can be reduced to H_2O through a series of proton-coupled electron transfer steps (B.3, B.4, B.5, B.7, B.9, B.10) and O-O bond scission steps (B.6, B.8, B.11) involving many intermediate species (*O, *OH, *etc.*). It is worth noting that O–O and O–OH denote dissociated O_2 and OOH respectively. These equations are listed below:

$$*O_2 + H^+ + e^- \leftrightarrow *OOH, r_3 = k_{+3} \theta_{O_2} - k_{-3} \theta_{OOH} \tag{B.3}$$

$$*\mathrm{O} + \mathrm{H}^+ + e^- \leftrightarrow *\mathrm{OH}, r_4 = k_{+4}\theta_{\mathrm{O}} - k_{-4}\theta_{\mathrm{OH}} \tag{B.4}$$

$$*\mathrm{OH} + \mathrm{H}^+ + e^- \leftrightarrow \mathrm{H_2O}_{(aq)} + *, r_5 = k_{+5}\theta_{\mathrm{OH}} - k_{-5}\theta_{*} \tag{B.5}$$

$$*\mathrm{O_2} \leftrightarrow *\mathrm{O\text{–}O}, r_6 = k_{+6}\theta_{\mathrm{O_2}} - k_{-6}\theta_{\mathrm{O\text{–}O}} \tag{B.6}$$

$$*\mathrm{O\text{–}O} + \mathrm{H}^+ + e^- \leftrightarrow *\mathrm{O\text{–}OH}, r_7 = k_{+7}\theta_{\mathrm{O\text{–}O}} - k_{-7}\theta_{\mathrm{O\text{–}OH}} \tag{B.7}$$

$$*\mathrm{OOH} \leftrightarrow *\mathrm{O\text{–}OH}, r_8 = k_{+8}\theta_{\mathrm{OOH}} - k_{-8}\theta_{\mathrm{O\text{–}OH}} \tag{B.8}$$

$$*\mathrm{O\text{–}OH} + \mathrm{H}^+ + e^- \leftrightarrow *\mathrm{O} + \mathrm{H_2O}_{(aq)}, r_9 = k_{+9}\theta_{\mathrm{O\text{–}OH}} - k_{-9}\theta_{\mathrm{O}} \tag{B.9}$$

$$*\mathrm{OOH} + \mathrm{H}^+ + e^- \leftrightarrow *\mathrm{H_2O_2}, r_{10} = k_{+10}\theta_{\mathrm{OOH}} - k_{-10}\theta_{\mathrm{H_2O_2}} \tag{B.10}$$

$$*\mathrm{H_2O_2} \leftrightarrow *\mathrm{O} + \mathrm{H_2O}_{(aq)}, r_{11} = k_{+11}\theta_{\mathrm{H_2O_2}} - k_{-11}\theta_{O} \tag{B.11}$$

The $\mathrm{H_2O_2}$ can possibly take off from the active site ending up with the $2e^-$ reaction pathway

$$*\mathrm{H_2O_2} \rightarrow \mathrm{H_2O_{2(aq)}} + *, r_{12} = k_{+12}\theta_{\mathrm{H_2O_2}} \tag{B.12}$$

These reaction rates are coupled with each other through rate equations describing the time variation of the surface species concentration:

$$\frac{\partial x_{\mathrm{O_{2(dl)}}}}{\partial t} = r_1 - r_2 \tag{B.13}$$

$$\frac{\partial \theta_{\mathrm{O_2}}}{\partial t} = r_2 - r_3 - r_6 \tag{B.14}$$

$$\frac{\partial \theta_{\mathrm{OOH}}}{\partial t} = r_3 - r_8 - r_{10} \tag{B.15}$$

$$\frac{\partial \theta_{\mathrm{O}}}{\partial t} = -r_4 + r_9 + r_{11} \tag{B.16}$$

$$\frac{\partial \theta_{\mathrm{OH}}}{\partial t} = r_4 - r_5 \tag{B.17}$$

$$\frac{\partial \theta_{\mathrm{H_2O_2}}}{\partial t} = r_{10} - r_{11} - r_{12} \tag{B.18}$$

$$\frac{\partial \theta_{\mathrm{O\text{-}O}}}{\partial t} = r_6 - r_7 \tag{B.19}$$

$$\frac{\partial \theta_{\mathrm{O\text{-}OH}}}{\partial t} = r_7 + r_8 - r_9 \tag{B.20}$$

Meanwhile, the site conservation on the catalyst surface must be satisfied:

$$\theta_{\mathrm{O_2}} + \theta_{\mathrm{OOH}} + \theta_{\mathrm{O}} + \theta_{\mathrm{OH}} + \theta_{\mathrm{H_2O_2}} + \theta_{\mathrm{O\text{-}O}} + \theta_{\mathrm{O\text{-}OH}} + \theta_* = 1 \tag{B.21}$$

These above equations can be solved numerically at steady state where the surface concentration of each species is invariant with respect to time. The parameters involved in these equations are summarized in Table B1. The molar fraction of O_2 in bulk electrolyte is chosen to be $x_{\mathrm{O_2}(aq)} = 2.34 \times 10^{-5}$ corresponding to 1 atm $\mathrm{O_{2(g)}}$ in equilibrium with $\mathrm{O_{2(aq)}}$ [102].

Table B1: The parameters used in microkinetic rate equations. The pre-factors (ν_f) are from Ref. [102]; the energy parameters (activation energy E_a and free energy change ΔG in unit of eV) are from DFT calculations in Section 7.3. The potential-dependent activation energies for protonation reations are reported at 0.8 V. In calculations, E_a is determined as the maximum of 0, E_a, and ΔG.

		FeN_4C_{10}		FeN_4C_{10}-w		FeN_4C_{12}		FeN_4C_8	
	$\nu_f(s^{-1})$	E_a	ΔG	E_a	ΔG	E_a	ΔG	E_a	ΔG
B.1	8×10^5	0	0	0	0	0	0	0	0
B.2	1×10^8	0	-0.98	0	-0.74	0	-0.63	0	-1.01
B.3	1×10^9	0.43	0.34	0.41	0.3	0.42	0.32	0.34	0.16
B.4	1×10^9	0.30	0.07	0.33	0.13	0.34	0.15	0.49	0.46
B.5	1×10^9	0.32	0.12	0.37	0.22	0.17	-0.19	0.26	-0.01
B.6	6.21×10^{12}	1.19	0.6	N/A		1.39	0.58	0.61	-0.49
B.7	1×10^9	0.01	-0.5	N/A		0.04	-0.44	-0.08	-0.68
B.8	6.21×10^{12}	0.56	-0.24	0.42	-0.15	0.72	-0.19	0.21	-1.33
B.9	1×10^9	-0.18	-0.88	-0.24	-0.99	-0.22	-0.96	0.35	0.18
B.10	1×10^9	0.88	1.23	0.89	1.25	0.63	0.73	-0.32*	-1.15*
B.11	6.21×10^{12}	0.01	-2.36	0	-2.38	0.04	-1.88	*B.10+B.11	
B.12	1×10^8	0.23	0.23	0.09	0.09	0.31	0.31	N/A	

APPENDIX C

DETERMINING GROUNDSTATE MULTIPLICITY FOR TM-N_4 COMPLEXES AND THEIR O_2 ADSORPTION SYSTEMS

The groundstate multiplicity for TM-N_4 complexes and their O_2 adsorption systems were determined by comparing the energies of each structure with different multiplicity as shown in Table C1 and C2.

Table C1: Calculated energy (eV, with respect to ground state) of different spin multiplicity for Cr, Mn, and Fe complexes.

	CrP		MnP		FeP	
Ground state	Quintet	0	Quartet	0	Triplet	0
Alternative state	Triplet	1.038	Doublet	0.781	Singlet	0.610
	CrPc		MnPc		FePc	
Ground state	Quintet	0	Quartet	0	Triplet	0
Alternative state	Triplet	0.723	Doublet	0.777	Singlet	1.100

Table C2: Calculated energy (eV, with respect to ground state) of combinations of different oxygen adsorption configurations and different spin multiplicity for CrP, MnP and FePc

	CrP		CrPc		MnP		MnPc	
	Singlet	Triplet	Singlet	Triplet	Doublet	Quartet	Doublet	Quartet
End45	N/A	0.230	N/A	0.252	0.043	0.400	0.112	0.414
End0	N/A	0.242	N/A	0.270	0.060	N/A	0.113	N/A
Side45	0.747	0.404	0.267	0.383	0.287	0.450	0.306	0.416
Side0	0.500	0	0.416	0	0.158	0	0.190	0
	FeP		FePc		CoP		CoPc	
	Singlet	Triplet	Singlet	Triplet	Doublet	Quartet	Doublet	Quartet
End45	0	0.270	0	0.274	0.053	N/A	0.097	N/A
End0	0.045	0.241	0.027	0.206	0	N/A	0	N/A
Side45	0.630	0.686	0.718	0.659	N/A	N/A	N/A	N/A
Side0	0.547	0.416	0.641	0.413	N/A	N/A	N/A	N/A

APPENDIX D

PARTIAL DENSITY OF STATES FOR FEN$_4$-C$_X$ SYSTEMS

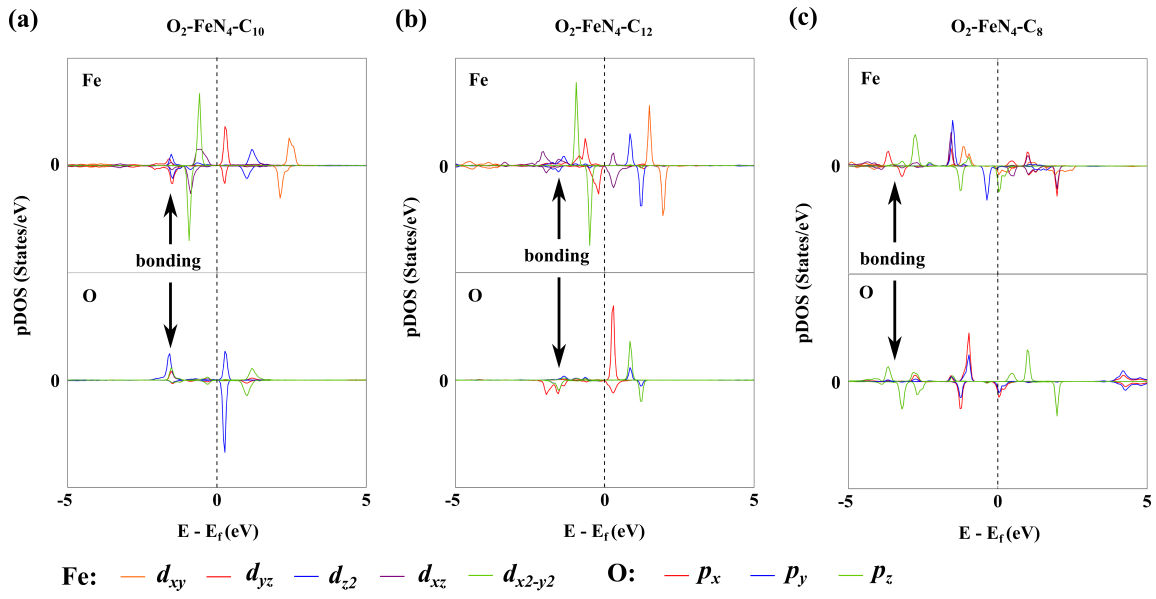

Figure D1: Partial density of states (pDOS) for decomposed d orbitals of Fe and p orbitals of the nearest O in O_2-FeN_4 adsorption systems. (a) O_2-FeN_4-C_{10}, (b) O_2-FeN_4-C_{12} and (c) O_2-FeN_4-C_8. The bonding orbital of Fe-O is marked as electronic state in which Fe $3d$ orbitals overlap with O $2p$ orbitals below Fermi energy.

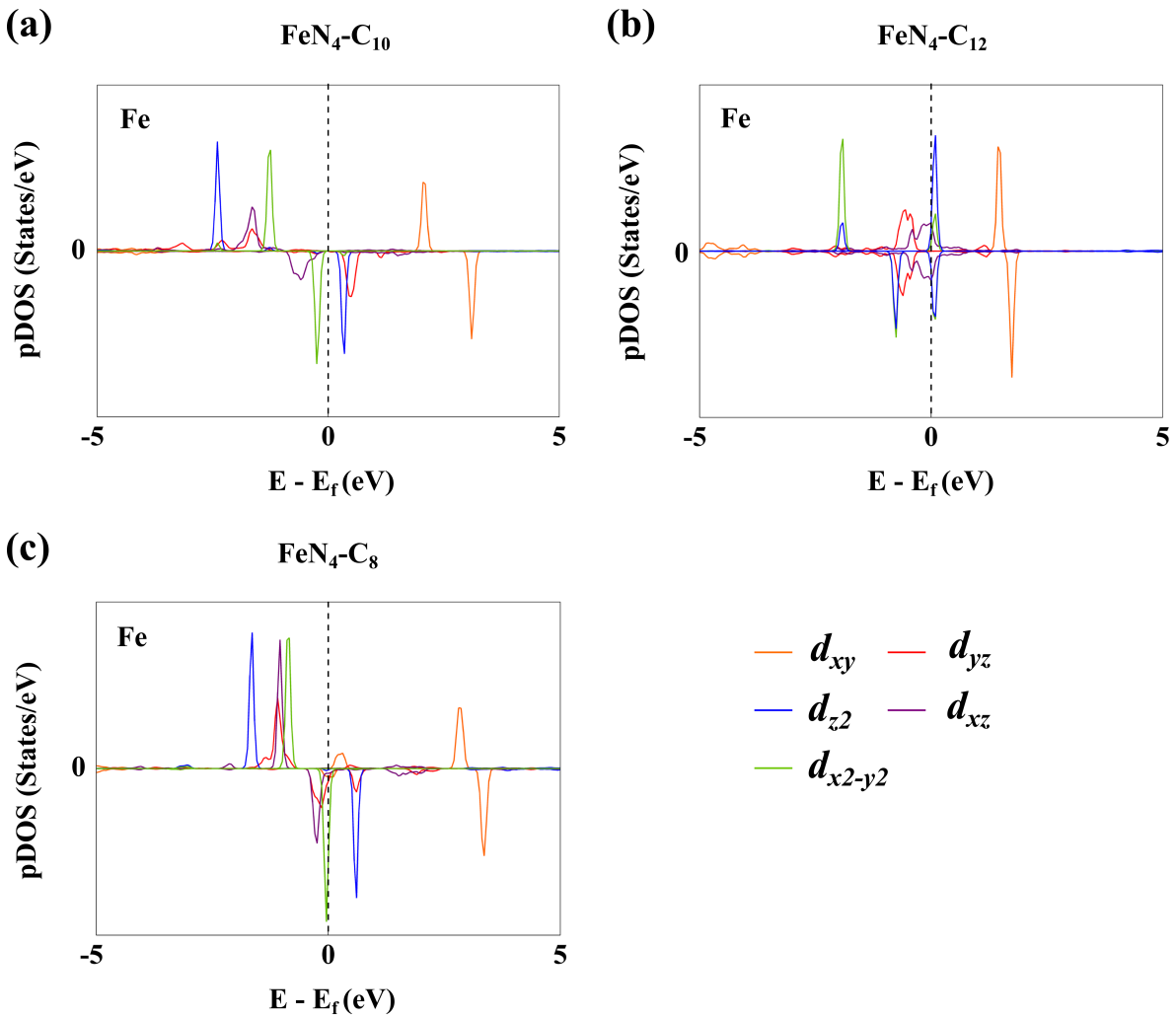

Figure D2: Partial density of states (pDOS) for decomposed d orbitals of Fe in the FeN_4-type active sites. (a) FeN_4-C_{10}, (b) FeN_4-C_{12} and (c) FeN_4-C_8.

BIBLIOGRAPHY

[1] Ali Mirchi, Saeed Hadian, Kaveh Madani, Omid M Rouhani, and Azadeh M Rouhani. World energy balance outlook and opec production capacity: implications for global oil security. *Energies*, 5(8):2626–2651, 2012.

[2] A Kirubakaran, Shailendra Jain, and RK Nema. A review on fuel cell technologies and power electronic interface. *Renewable and Sustainable Energy Reviews*, 13(9):2430–2440, 2009.

[3] Ross A Lemons. Fuel cells for transportation. *Journal of Power Sources*, 29(1-2):251–264, 1990.

[4] B. C. H. Steele and A. Heinzel. Materials for fuel-cell technologies. *Nature*, 414(6861):345–352, 2001.

[5] M. K. Debe. Electrocatalyst approaches and challenges for automotive fuel cells. *Nature*, 486(7401):43–51, 2012.

[6] Mufan Li, Zipeng Zhao, Tao Cheng, Alessandro Fortunelli, Chih-Yen Chen, Rong Yu, Qinghua Zhang, Lin Gu, Boris V Merinov, Zhaoyang Lin, et al. Ultrafine jagged platinum nanowires enable ultrahigh mass activity for the oxygen reduction reaction. *Science*, 354(6318):1414–1419, 2016.

[7] Xiaoqing Huang, Zipeng Zhao, Liang Cao, Yu Chen, Enbo Zhu, Zhaoyang Lin, Mufan Li, Aiming Yan, Alex Zettl, Y Morris Wang, et al. High-performance transition metal–doped pt3ni octahedra for oxygen reduction reaction. *Science*, 348(6240):1230–1234, 2015.

[8] Sungeun Yang, Jiwhan Kim, Young Joo Tak, Aloysius Soon, and Hyunjoo Lee. Single-atom catalyst of platinum supported on titanium nitride for selective electrochemical reactions. *Angewandte Chemie International Edition*, 55(6):2058–2062, 2016.

[9] Sungeun Yang, Young Joo Tak, Jiwhan Kim, Aloysius Soon, and Hyunjoo Lee. Support effect in single-atom platinum catalyst for electrochemical oxygen reduction. *ACS Catalysis*, 2016.

[10] Raymond Jasinski. A new fuel cell cathode catalyst. *Nature*, 201(4925):1212–1213, 1964.

[11] Raymond Jasinski. Cobalt phthalocyanine as a fuel cell cathode. *Journal of the Electrochemical Society*, 112(5):526–528, 1965.

[12] J-P Randin. Interpretation of the relative electrochemical activity of various metal phthalocyanines for the oxygen reduction reaction. *Electrochimica Acta*, 19(2):83–85, 1974.

[13] Horst Jahnke, Manfred Schönborn, and Georg Zimmermann. Organic dyestuffs as catalysts for fuel cells. In *Physical and chemical applications of dyestuffs*, pages 133–181. Springer, 1976.

[14] Justus Masa and Wolfgang Schuhmann. Systematic selection of metalloporphyrin-based catalysts for oxygen reduction by modulation of the donor–acceptor intermolecular hardness. *Chemistry–A European Journal*, 19(29):9644–9654, 2013.

[15] Zhongwei Chen, Drew Higgins, Aiping Yu, Lei Zhang, and Jiujun Zhang. A review on non-precious metal electrocatalysts for pem fuel cells. *Energy & Environmental Science*, 4(9):3167–3192, 2011.

[16] Rajesh Bashyam and Piotr Zelenay. A class of non-precious metal composite catalysts for fuel cells. *Nature*, 443(7107):63–66, 2006.

[17] Michel Lefèvre, Eric Proietti, Frédéric Jaouen, and Jean-Pol Dodelet. Iron-based catalysts with improved oxygen reduction activity in polymer electrolyte fuel cells. *science*, 324(5923):71–74, 2009.

[18] Gang Wu, Karren L More, Christina M Johnston, and Piotr Zelenay. High-performance electrocatalysts for oxygen reduction derived from polyaniline, iron, and cobalt. *Science*, 332(6028):443–447, 2011.

[19] Yanguang Li, Wu Zhou, Hailiang Wang, Liming Xie, Yongye Liang, Fei Wei, Juan-Carlos Idrobo, Stephen J Pennycook, and Hongjie Dai. An oxygen reduction electrocatalyst based on carbon nanotube-graphene complexes. *Nature nanotechnology*, 7(6):394–400, 2012.

[20] Hoon T Chung, Jong H Won, and Piotr Zelenay. Active and stable carbon nanotube/nanoparticle composite electrocatalyst for oxygen reduction. *Nature communications*, 4:1922, 2013.

[21] Khaled Parvez, Shubin Yang, Yenny Hernandez, Andreas Winter, Andrey Turchanin, Xinliang Feng, and Klaus Mullen. Nitrogen-doped graphene and its iron-based composite as efficient electrocatalysts for oxygen reduction reaction. *Acs Nano*, 6(11):9541–9550, 2012.

[22] Hai-Wei Liang, Wei Wei, Zhong-Shuai Wu, Xinliang Feng, and Klaus Mullen. Mesoporous metal–nitrogen-doped carbon electrocatalysts for highly efficient oxygen reduction reaction. *Journal of the American Chemical Society*, 135(43):16002–16005, 2013.

[23] Mei-Qing Wang, Wei-Hua Yang, Hong-Hui Wang, Chi Chen, Zhi-You Zhou, and Shi-Gang Sun. Pyrolyzed fe–n–c composite as an efficient non-precious metal catalyst for oxygen reduction reaction in acidic medium. *ACS Catalysis*, 4(11):3928–3936, 2014.

[24] Zhi-Yu Yang, Yu-Xia Zhang, Lin Jing, Yu-Fei Zhao, Yi-Ming Yan, and Ke-Ning Sun. Beanpod-shaped fe–c–n composite as promising orr catalyst for fuel cells operated in neutral media. *Journal of Materials Chemistry A*, 2(8):2623–2627, 2014.

[25] Jian Zhang, Daping He, Hao Su, Xu Chen, Mu Pan, and Shichun Mu. Porous polyaniline-derived fenxc/c catalysts with high activity and stability towards oxygen reduction reaction using ferric chloride both as an oxidant and iron source. *Journal of Materials Chemistry A*, 2:1242–1246, 2014.

[26] Jens K Nørskov, Frank Abild-Pedersen, Felix Studt, and Thomas Bligaard. Density functional theory in surface chemistry and catalysis. *Proceedings of the National Academy of Sciences*, 108(3):937–943, 2011.

[27] K Honkala, Anders Hellman, IN Remediakis, Ashildur Logadottir, A Carlsson, Søren Dahl, Claus H Christensen, and Jens Kehlet Nørskov. Ammonia synthesis from first-principles calculations. *Science*, 307(5709):555–558, 2005.

[28] Martin P Andersson, Thomas Bligaard, Arkady Kustov, Kasper E Larsen, Jeffrey Greeley, Tue Johannessen, Claus H Christensen, and Jens K Nørskov. Toward computational screening in heterogeneous catalysis: Pareto-optimal methanation catalysts. *Journal of Catalysis*, 239(2):501–506, 2006.

[29] Vojislav R Stamenkovic, Bongjin Simon Mun, Matthias Arenz, Karl JJ Mayrhofer, Christopher A Lucas, Guofeng Wang, Philip N Ross, and Nenad M Markovic. Trends in electrocatalysis on extended and nanoscale pt-bimetallic alloy surfaces. *Nature materials*, 6(3):241–247, 2007.

[30] AMTP Van Der Putten, A Elzing, W Visscher, and E Barendrecht. Oxygen reduction on pyrolysed carbon-supported transition metal chelates. *Journal of electroanalytical chemistry and interfacial electrochemistry*, 205(1-2):233–244, 1986.

[31] K Wiesener, D Ohms, V Neumann, and R Franke. N_4 macrocycles as electrocatalysts for the cathodic reduction of oxygen. *Materials chemistry and physics*, 22(3-4):457–475, 1989.

[32] R Franke, D Ohms, and K Wiesener. Investigation of the influence of thermal treatment on the properties of carbon materials modified by N_4-chelates for the reduction of oxygen in acidic media. *Journal of electroanalytical chemistry and interfacial electrochemistry*, 260(1):63–73, 1989.

[33] S Gupta, D Tryk, I Bae, W Aldred, and E Yeager. Heat-treated polyacrylonitrile-based catalysts for oxygen electroreduction. *Journal of applied electrochemistry*, 19(1):19–27, 1989.

[34] Frédéric Jaouen and Jean-Pol Dodelet. Average turn-over frequency of O_2 electroreduction for Fe/N/C and Co/N/C catalysts in PEFCs. *Electrochimica Acta*, 52(19):5975–5984, 2007.

[35] Stéphane Ruggeri and Jean-Pol Dodelet. Influence of structural properties of pristine carbon blacks on activity of Fe/N/C cathode catalysts for PEFCs. *Journal of The Electrochemical Society*, 154(8):B761–B769, 2007.

[36] Frédéric Jaouen, Michel Lefèvre, Jean-Pol Dodelet, and Mei Cai. Heat-treated Fe/N/C catalysts for O_2 electroreduction: are active sites hosted in micropores? *The Journal of Physical Chemistry B*, 110(11):5553–5558, 2006.

[37] Juan Herranz, Michel Lefèvre, Nicholas Larouche, Barry Stansfield, and Jean-Pol Dodelet. Step-by-step synthesis of non-noble metal electrocatalysts for O_2 reduction under proton exchange membrane fuel cell conditions. *The Journal of Physical Chemistry C*, 111(51):19033–19042, 2007.

[38] So Jeong Kim, Kee Suk Nahm, and Pil Kim. High electrocatalytic performance of NH_3-activated iron-adsorbed polyaniline for oxygen reduction reactions. *Catalysis letters*, 142(10):1244–1250, 2012.

[39] Thomas E Wood, Zhongshu Tan, Alison K Schmoeckel, David ONeill, and Radoslav Atanasoski. Non-precious metal oxygen reduction catalyst for PEM fuel cells based on nitroaniline precursor. *Journal of Power Sources*, 178(2):510–516, 2008.

[40] Ja-Yeon Choi, Drew Higgins, Gaopeng Jiang, Ryan Hsu, Jinli Qiao, and Zhongwei Chen. Iron-tetracyanobenzene complex derived non-precious catalyst for oxygen reduction reaction. *Electrochimica Acta*, 162:224–229, 2015.

[41] Ulrike I Koslowski, Irmgard Abs-Wurmbach, Sebastian Fiechter, and Peter Bogdanoff. Nature of the catalytic centers of porphyrin-based electrocatalysts for the ORR: a correlation of kinetic current density with the site density of Fe-N_4 centers. *The Journal of Physical Chemistry C*, 112(39):15356–15366, 2008.

[42] C Medard, M Lefevre, JP Dodelet, Frédéric Jaouen, and Göran Lindbergh. Oxygen reduction by Fe-based catalysts in PEM fuel cell conditions: activity and selectivity of the catalysts obtained with two Fe precursors and various carbon supports. *Electrochimica Acta*, 51(16):3202–3213, 2006.

[43] Fanny Charreteur, Frédéric Jaouen, and Jean-Pol Dodelet. Iron porphyrin-based cathode catalysts for PEM fuel cells: Influence of pyrolysis gas on activity and stability. *Electrochimica Acta*, 54(26):6622–6630, 2009.

[44] Frédéric Jaouen and Jean-Pol Dodelet. Non-noble electrocatalysts for O_2 reduction: how does heat treatment affect their activity and structure? Part I. Model for carbon black gasification by NH_3: parametric calibration and electrochemical validation. *The Journal of Physical Chemistry C*, 111(16):5963–5970, 2007.

[45] Frédéric Jaouen, Alessandra Maria Serventi, Michel Lefèvre, Jean-Pol Dodelet, and Patrick Bertrand. Non-noble electrocatalysts for O_2 reduction: how does heat treatment affect their activity and structure? Part II. Structural changes observed by electron microscopy, Raman, and mass spectroscopy. *The Journal of Physical Chemistry C*, 111(16):5971–5976, 2007.

[46] Ruiguo Cao, Ranjit Thapa, Hyejung Kim, Xiaodong Xu, Min Gyu Kim, Qing Li, Noejung Park, Meilin Liu, and Jaephil Cho. Promotion of oxygen reduction by a bio-inspired tethered iron phthalocyanine carbon nanotube-based catalyst. *Nature communications*, 4(2076), 2013.

[47] Thorsten Schilling, Ayodele Okunola, Justus Masa, Wolfgang Schuhmann, and Michael Bron. Carbon nanotubes modified with electrodeposited metal porphyrins and phenanthrolines for electrocatalytic applications. *Electrochimica Acta*, 55(26):7597–7602, 2010.

[48] Rui Zhang, Yingxiang Peng, Zhipan Li, Kai Li, Jie Ma, Yi Liao, Lirong Zheng, Xia Zuo, and Dingguo Xia. Oxygen electroreduction on heat-treated multi-walled carbon nanotubes supported iron polyphthalocyanine in acid media. *Electrochimica Acta*, 147:343–351, 2014.

[49] Yuanyuan Jiang, Yizhong Lu, Xiangyu Lv, Dongxue Han, Qixian Zhang, Li Niu, and Wei Chen. Enhanced catalytic performance of pt-free iron phthalocyanine by graphene support for efficient oxygen reduction reaction. *ACS Catalysis*, 3(6):1263–1271, 2013.

[50] Xia Gao, Jingfang Wang, Zhao Ma, and Jianshan Ye. Iron tetrasulfophthalocyanine functionalized graphene nanosheets for oxygen reduction reaction in alkaline media. *Electrochimica Acta*, 130:543–550, 2014.

[51] Nobuyoshi Nakagawa, Mohammad Ali Abdelkareem, Daiki Takino, Takayuki Ishikawa, and Takuya Tsujiguchi. PAN based carbon nanofibers as an active ORR catalyst for DMFC. *ECS Transactions*, 41(1):2219–2229, 2011.

[52] Joshua P McClure, Christina K Devine, Rongzhong Jiang, Deryn Chu, Jerome J Cuomo, Gregory N Parsons, and Peter S Fedkiw. Oxygen electroreduction on Ti- and Fe-containing carbon fibers. *Journal of The Electrochemical Society*, 160(8):F769–F778, 2013.

[53] Dan Li and Younan Xia. Electrospinning of nanofibers: reinventing the wheel? *Advanced Materials*, 16(14):1151–1170, 2004.

[54] Hui Meng, Frédéric Jaouen, Eric Proietti, Michel Lefèvre, and Jean-Pol Dodelet. ph-effect on oxygen reduction activity of Fe-based electro-catalysts. *Electrochemistry communications*, 11(10):1986–1989, 2009.

[55] Xuguang Li, Gang Liu, and Branko N Popov. Activity and stability of non-precious metal catalysts for oxygen reduction in acid and alkaline electrolytes. *Journal of Power Sources*, 195(19):6373–6378, 2010.

[56] Kai Wan, Zhi-peng Yu, Xiao-hua Li, Ming-yao Liu, Gang Yang, Jin-hua Piao, and Zhen-xing Liang. ph effect on electrochemistry of nitrogen-doped carbon catalyst for oxygen reduction reaction. *ACS Catalysis*, 5(7):4325–4332, 2015.

[57] Xiao-Zi Yuan, Hui Li, Shengsheng Zhang, Jonathan Martin, and Haijiang Wang. A review of polymer electrolyte membrane fuel cell durability test protocols. *Journal of Power Sources*, 196(22):9107–9116, 2011.

[58] Allen J Bard, Larry R Faulkner, Johna Leddy, and Cynthia G Zoski. *Electrochemical methods: fundamentals and applications*. Wiley New York, 2nd edition, 1980.

[59] Shengsheng Zhang, Xiaozi Yuan, Haijiang Wang, Walter Mérida, Hong Zhu, Jun Shen, Shaohong Wu, and Jiujun Zhang. A review of accelerated stress tests of mea durability in pem fuel cells. *International journal of hydrogen energy*, 34(1):388–404, 2009.

[60] Héctor R Colón-Mercado and Branko N Popov. Stability of platinum based alloy cathode catalysts in pem fuel cells. *Journal of Power Sources*, 155(2):253–263, 2006.

[61] Sadia Kabir, Kateryna Artyushkova, Boris Kiefer, and Plamen Atanassov. Computational and experimental evidence for a new TM-N_3/C moiety family in non-PGM electrocatalysts. *Physical Chemistry Chemical Physics*, 17(27):17785–17789, 2015.

[62] Fanny Charreteur, Frédéric Jaouen, Stéphane Ruggeri, and Jean-Pol Dodelet. Fe/N/C non-precious catalysts for PEM fuel cells: Influence of the structural parameters of pristine commercial carbon blacks on their activity for oxygen reduction. *Electrochimica acta*, 53(6):2925–2938, 2008.

[63] Urszula Tylus, Qingying Jia, Kara Strickland, Nagappan Ramaswamy, Alexey Serov, Plamen Atanassov, and Sanjeev Mukerjee. Elucidating oxygen reduction active sites in pyrolyzed metal–nitrogen coordinated non-precious-metal electrocatalyst systems. *The Journal of Physical Chemistry C*, 118(17):8999–9008, 2014.

[64] Edward F Holby, Gang Wu, Piotr Zelenay, and Christopher D Taylor. Structure of fe–n x–c defects in oxygen reduction reaction catalysts from first-principles modeling. *The Journal of Physical Chemistry C*, 118(26):14388–14393, 2014.

[65] Edward F Holby and Christopher D Taylor. Activity of N-coordinated multi-metal-atom active site structures for Pt-free oxygen reduction reaction catalysis: Role of $*$OH ligands. *Scientific reports*, 5, 2015.

[66] Dehui Deng, Xiaoqi Chen, Liang Yu, Xing Wu, Qingfei Liu, Yun Liu, Huaixin Yang, Huanfang Tian, Yongfeng Hu, Peipei Du, et al. A single iron site confined in a graphene matrix for the catalytic oxidation of benzene at room temperature. *Science advances*, 1(11):e1500462, 2015.

[67] Qing Li, Gang Wu, David A Cullen, Karren L More, Nathan H Mack, Hoon T Chung, and Piotr Zelenay. Phosphate-tolerant oxygen reduction catalysts. *ACS Catalysis*, 4(9):3193–3200, 2014.

[68] Nagappan Ramaswamy, Urszula Tylus, Qingying Jia, and Sanjeev Mukerjee. Activity descriptor identification for oxygen reduction on nonprecious electrocatalysts: Linking surface science to coordination chemistry. *Journal of the American Chemical Society*, 135(41):15443–15449, 2013.

[69] Frédéric Jaouen, Juan Herranz, Michel Lefevre, Jean-Pol Dodelet, Ulrike I Kramm, Iris Herrmann, Peter Bogdanoff, Jun Maruyama, Toru Nagaoka, Arnd Garsuch, et al. Cross-laboratory experimental study of non-noble-metal electrocatalysts for the oxygen reduction reaction. *ACS applied materials & interfaces*, 1(8):1623–1639, 2009.

[70] Ulrike I Kramm, Michel Lefèvre, Nicholas Larouche, Dieter Schmeisser, and Jean-Pol Dodelet. Correlations between mass activity and physicochemical properties of Fe/N/C catalysts for the ORR in PEM fuel cell via ^{57}Fe Mössbauer spectroscopy and other techniques. *Journal of the American Chemical Society*, 136(3):978–985, 2014.

[71] Ulrike I Kramm, Juan Herranz, Nicholas Larouche, Thomas M Arruda, Michel Lefèvre, Frédéric Jaouen, Peter Bogdanoff, Sebastian Fiechter, Irmgard Abs-Wurmbach, Sanjeev Mukerjee, et al. Structure of the catalytic sites in Fe/N/C-catalysts for O_2-reduction in PEM fuel cells. *Physical Chemistry Chemical Physics*, 14(33):11673–11688, 2012.

[72] Deepika Singh, Kuldeep Mamtani, Christopher R Bruening, Jeffrey T Miller, and Umit S Ozkan. Use of H_2S to probe the active sites in FeNC catalysts for the oxygen reduction reaction (ORR) in acidic media. *Acs Catalysis*, 4(10):3454–3462, 2014.

[73] Magali Ferrandon, A Jeremy Kropf, Deborah J Myers, Kateryna Artyushkova, Ulrike Kramm, Peter Bogdanoff, Gang Wu, Christina M Johnston, and Piotr Zelenay. Multitechnique characterization of a polyaniline–iron–carbon oxygen reduction catalyst. *The Journal of Physical Chemistry C*, 116(30):16001–16013, 2012.

[74] Andrea Zitolo, Vincent Goellner, Vanessa Armel, Moulay-Tahar Sougrati, Tzonka Mineva, Lorenzo Stievano, Emiliano Fonda, and Frédéric Jaouen. Identification of catalytic sites for oxygen reduction in iron-and nitrogen-doped graphene materials. *Nature materials*, 14(9):937–942, 2015.

[75] Svitlana Pylypenko, Sanjoy Mukherjee, Tim S Olson, and Plamen Atanassov. Non-platinum oxygen reduction electrocatalysts based on pyrolyzed transition metal macrocycles. *Electrochimica Acta*, 53(27):7875–7883, 2008.

[76] Pierre Hohenberg and Walter Kohn. Inhomogeneous electron gas. *Physical review*, 136(3B):B864, 1964.

[77] Walter Kohn and Lu Jeu Sham. Self-consistent equations including exchange and correlation effects. *Physical review*, 140(4A):A1133, 1965.

[78] Jens Kehlet Nørskov, Thomas Bligaard, Jan Rossmeisl, and Claus Hviid Christensen. Towards the computational design of solid catalysts. *Nature chemistry*, 1(1):37–46, 2009.

[79] B Hammer and JK Nørskov. Why gold is the noblest of all the metals. *Nature*, 376(6537):238, 1995.

[80] Zhiyao Duan and Guofeng Wang. A first principles study of oxygen reduction reaction on a Pt (111) surface modified by a subsurface transition metal M (M= Ni, Co, or Fe). *Physical Chemistry Chemical Physics*, 13(45):20178–20187, 2011.

[81] Rongrong Chen, Haixia Li, Deryn Chu, and Guofeng Wang. Unraveling oxygen reduction reaction mechanisms on carbon-supported Fe-phthalocyanine and Co-phthalocyanine catalysts in alkaline solutions. *The Journal of Physical Chemistry C*, 113(48):20689–20697, 2009.

[82] VS Bagotzky, MR Tarasevich, KA Radyushkina, OA Levina, and SI Andrusyova. Electrocatalysis of the oxygen reduction process on metal chelates in acid electrolyte. *Journal of Power Sources*, 2(3):233–240, 1978.

[83] Zheng Shi and Jiujun Zhang. Density functional theory study of transitional metal macrocyclic complexes' dioxygen-binding abilities and their catalytic activities toward oxygen reduction reaction. *The Journal of Physical Chemistry C*, 111(19):7084–7090, 2007.

[84] Muneyuki Tsuda, Eben Sy Dy, and Hideaki Kasai. Comparative study of O_2 dissociation on various metalloporphyrins. *The Journal of chemical physics*, 122(24):244719, 2005.

[85] Guofeng Wang, Nitia Ramesh, Andrew Hsu, Deryn Chu, and Rongrong Chen. Density functional theory study of the adsorption of oxygen molecule on iron phthalocyanine and cobalt phthalocyanine. *Molecular Simulation*, 34(10-15):1051–1056, 2008.

[86] Hui He, Yinkai Lei, Chan Xiao, Deryn Chu, Rongrong Chen, and Guofeng Wang. Molecular and electronic structures of transition-metal macrocyclic complexes as related to catalyzing oxygen reduction reactions: a density functional theory study. *The Journal of Physical Chemistry C*, 116(30):16038–16046, 2012.

[87] Shaorui Sun, Ning Jiang, and Dingguo Xia. Density functional theory study of the oxygen reduction reaction on metalloporphyrins and metallophthalocyanines. *The Journal of Physical Chemistry C*, 115(19):9511–9517, 2011.

[88] Antonín Trojánek, Jan Langmaier, Hana Kvapilová, Stanislav Záliš, and Zdeněk Samec. Inhibitory effect of water on the oxygen reduction catalyzed by cobalt(II) tetraphenylporphyrin. *The Journal of Physical Chemistry A*, 118(11):2018–2028, 2014.

[89] Linus Pauling and Joseph J Weiss. Nature of the iron–oxygen bond in oxyhaemoglobin. *Nature*, 203(4941):183–183, 1964.

[90] JS Griffith. On the magnetic properties of some haemoglobin complexes. In *Proceedings of the Royal Society of London A: Mathematical, Physical and Engineering Sciences*, volume 235, pages 23–36. The Royal Society, 1956.

[91] Edward Frank Holby, Gang Wu, Piotr Zelenay, and CD Taylor. Metropolis Monte Carlo search for non-precious metal catalyst active site candidates. *ECS Transactions*, 50(2):1839–1845, 2013.

[92] Edward F Holby and Piotr Zelenay. Linking structure to function: the search for active sites in non-platinum group metal oxygen reduction reaction catalysts. *Nano Energy*, 29:54–64, 2016.

[93] Shyam Kattel and Guofeng Wang. Reaction pathway for oxygen reduction on FeN_4 embedded graphene. *The journal of physical chemistry letters*, 5(3):452–456, 2014.

[94] EF Holby and CD Taylor. Control of graphene nanoribbon vacancies by Fe and N dopants: Implications for catalysis. *Applied Physics Letters*, 101(6):064102, 2012.

[95] Federico Calle-Vallejo, José Ignacio Martínez, and Jan Rossmeisl. Density functional studies of functionalized graphitic materials with late transition metals for oxygen reduction reactions. *Physical Chemistry Chemical Physics*, 13(34):15639–15643, 2011.

[96] Shyam Kattel, Plamen Atanassov, and Boris Kiefer. Catalytic activity of Co-N_x/C electrocatalysts for oxygen reduction reaction: a density functional theory study. *Physical Chemistry Chemical Physics*, 15(1):148–153, 2013.

[97] Shyam Kattel, Plamen Atanassov, and Boris Kiefer. Density functional theory study of Ni-N_x/C electrocatalyst for oxygen reduction in alkaline and acidic media. *The Journal of Physical Chemistry C*, 116(33):17378–17383, 2012.

[98] Shyam Kattel, Plamen Atanassov, and Boris Kiefer. A density functional theory study of oxygen reduction reaction on non-PGM Fe-N_x-C electrocatalysts. *Physical Chemistry Chemical Physics*, 16(27):13800–13806, 2014.

[99] Shyam Kattel and Guofeng Wang. A density functional theory study of oxygen reduction reaction on Me–N_4 (Me= Fe, Co, or Ni) clusters between graphitic pores. *Journal of Materials Chemistry A*, 1(36):10790–10797, 2013.

[100] Walter Orellana. Catalytic properties of transition metal–N_4 moieties in graphene for the oxygen reduction reaction: evidence of spin-dependent mechanisms. *The Journal of Physical Chemistry C*, 117(19):9812–9818, 2013.

[101] Jing Zhang, Zhijian Wang, and Zhenping Zhu. The inherent kinetic electrochemical reduction of oxygen into H_2O on FeN_4-carbon: a density functional theory study. *Journal of Power Sources*, 255:65–69, 2014.

[102] Heine A Hansen, Venkatasubramanian Viswanathan, and Jens K Nørskov. Unifying kinetic and thermodynamic analysis of $2e^-$ and $4e^-$ reduction of oxygen on metal surfaces. *The Journal of Physical Chemistry C*, 118(13):6706–6718, 2014.

[103] Liang Qi and Ju Li. Adsorbate interactions on surface lead to a flattened sabatier volcano plot in reduction of oxygen. *Journal of catalysis*, 295:59–69, 2012.

[104] JC Chen and IR Harrison. Modification of polyacrylonitrile (PAN) carbon fiber precursor via post-spinning plasticization and stretching in dimethyl formamide (DMF). *Carbon*, 40(1):25–45, 2002.

[105] Zhang Wangxi, Liu Jie, and Wu Gang. Evolution of structure and properties of PAN precursors during their conversion to carbon fibers. *Carbon*, 41(14):2805–2812, 2003.

[106] Xingxu Yan, Lin Gan, Yuh-Chen Lin, Lu Bai, Tuo Wang, Xiangqing Wang, Jun Luo, and Jing Zhu. Controllable synthesis and enhanced electrocatalysis of iron-based catalysts derived from electrospun nanofibers. *Small*, 10(20):4072–4079, 2014.

[107] Xingxu Yan, Kexi Liu, Xiangqing Wang, Tuo Wang, Jun Luo, and Jing Zhu. Optimized electrospinning synthesis of iron–nitrogen–carbon nanofibers for high electrocatalysis of oxygen reduction in alkaline medium. *Nanotechnology*, 26(16):165401, 2015.

[108] Gang Wu, Christina M Johnston, Nathan H Mack, Kateryna Artyushkova, Magali Ferrandon, Mark Nelson, Juan S Lezama-Pacheco, Steven D Conradson, Karren L More, Deborah J Myers, et al. Synthesis–structure–performance correlation for polyaniline–Me–c non-precious metal cathode catalysts for oxygen reduction in fuel cells. *Journal of Materials Chemistry*, 21(30):11392–11405, 2011.

[109] Bjørk Hammer and Jens Kehlet Nørskov. Theoretical surface science and catalysiscalculations and concepts. *Advances in catalysis*, 45:71–129, 2000.

[110] D. R. Hamann, M. Schlüter, and C. Chiang. Norm-conserving pseudopotentials. *Phys. Rev. Lett.*, 43:1494–1497, Nov 1979.

[111] D. R. Hamann. Generalized norm-conserving pseudopotentials. *Phys. Rev. B*, 40:2980–2987, Aug 1989.

[112] David Vanderbilt. Soft self-consistent pseudopotentials in a generalized eigenvalue formalism. *Phys. Rev. B*, 41:7892–7895, Apr 1990.

[113] Kari Laasonen, Roberto Car, Changyol Lee, and David Vanderbilt. Implementation of ultrasoft pseudopotentials in *ab initio* molecular dynamics. *Phys. Rev. B*, 43:6796–6799, Mar 1991.

[114] Kari Laasonen, Alfredo Pasquarello, Roberto Car, Changyol Lee, and David Vanderbilt. Car-parrinello molecular dynamics with vanderbilt ultrasoft pseudopotentials. *Phys. Rev. B*, 47:10142–10153, Apr 1993.

[115] P. E. Blöchl. Projector augmented-wave method. *Phys. Rev. B*, 50:17953–17979, Dec 1994.

[116] G. Kresse and D. Joubert. From ultrasoft pseudopotentials to the projector augmented-wave method. *Phys. Rev. B*, 59:1758–1775, Jan 1999.

[117] Robert O Jones and Olle Gunnarsson. The density functional formalism, its applications and prospects. *Reviews of Modern Physics*, 61(3):689, 1989.

[118] John P Perdew and Alex Zunger. Self-interaction correction to density-functional approximations for many-electron systems. *Physical Review B*, 23(10):5048, 1981.

[119] Axel D Becke. Density-functional exchange-energy approximation with correct asymptotic behavior. *Physical review A*, 38(6):3098, 1988.

[120] Chengteh Lee, Weitao Yang, and Robert G Parr. Development of the colle-salvetti correlation-energy formula into a functional of the electron density. *Physical review B*, 37(2):785, 1988.

[121] John P Perdew, John A Chevary, Sy H Vosko, Koblar A Jackson, Mark R Pederson, Dig J Singh, and Carlos Fiolhais. Atoms, molecules, solids, and surfaces: Applications of the generalized gradient approximation for exchange and correlation. *Physical Review B*, 46(11):6671, 1992.

[122] John P Perdew, Kieron Burke, and Matthias Ernzerhof. Generalized gradient approximation made simple. *Physical review letters*, 77(18):3865, 1996.

[123] Bernard Delley. From molecules to solids with the DMol^3 approach. *The Journal of chemical physics*, 113(18):7756–7764, 2000.

[124] John P Perdew and Yue Wang. Accurate and simple analytic representation of the electron-gas correlation energy. *Physical Review B*, 45(23):13244, 1992.

[125] Georg Kresse and Jürgen Hafner. Ab initio molecular dynamics for liquid metals. *Physical Review B*, 47(1):558, 1993.

[126] Georg Kresse and Jürgen Furthmüller. Efficiency of ab-initio total energy calculations for metals and semiconductors using a plane-wave basis set. *Computational Materials Science*, 6(1):15–50, 1996.

[127] Hendrik J Monkhorst and James D Pack. Special points for brillouin-zone integrations. *Physical review B*, 13(12):5188, 1976.

[128] Graeme Henkelman, Blas P Uberuaga, and Hannes Jónsson. A climbing image nudged elastic band method for finding saddle points and minimum energy paths. *The Journal of chemical physics*, 113(22):9901–9904, 2000.

[129] Robert C Weast, Melvin J Astle, William H Beyer, et al. *CRC handbook of chemistry and physics*, volume 69. CRC press Boca Raton, FL, 1988.

[130] Jens Kehlet Nørskov, Jan Rossmeisl, Ashildur Logadottir, LRKJ Lindqvist, John R Kitchin, Thomas Bligaard, and Hannes Jonsson. Origin of the overpotential for oxygen reduction at a fuel-cell cathode. *The Journal of Physical Chemistry B*, 108(46):17886–17892, 2004.

[131] Vladimir Tripković, Egill Skúlason, Samira Siahrostami, Jens K Nørskov, and Jan Rossmeisl. The oxygen reduction reaction mechanism on Pt (111) from density functional theory calculations. *Electrochimica Acta*, 55(27):7975–7981, 2010.

[132] Joseph M Ziegelbauer, Tim S Olson, Svitlana Pylypenko, Faisal Alamgir, Cherno Jaye, Plamen Atanassov, and Sanjeev Mukerjee. Direct spectroscopic observation of the structural origin of peroxide generation from Co-based pyrolyzed porphyrins for ORR applications. *The Journal of Physical Chemistry C*, 112(24):8839–8849, 2008.

[133] Kateryna Artyushkova, Svitlana Pylypenko, Tim S Olson, Julia E Fulghum, and Plamen Atanassov. Predictive modeling of electrocatalyst structure based on structure-to-property correlations of X-ray photoelectron spectroscopic and electrochemical measurements. *Langmuir*, 24(16):9082–9088, 2008.

[134] Kateryna Artyushkova, Stephen Levendosky, Plamen Atanassov, and Julia Fulghum. XPS structural studies of nano-composite non-platinum electrocatalysts for polymer electrolyte fuel cells. *Topics in Catalysis*, 46(3-4):263–275, 2007.

[135] Jason Wu, Wenmu Li, Drew Higgins, and Zhongwei Chen. Heat-treated nonprecious catalyst using Fe and nitrogen-rich 2, 3, 7, 8-tetra (pyridin-2-yl) pyrazino [2, 3-g] quinoxaline coordinated complex for oxygen reduction reaction in PEM fuel cells. *The Journal of Physical Chemistry C*, 115(38):18856–18862, 2011.

[136] Siyu Ye and Ashok K Vijh. Cobalt-carbonized aerogel nanocomposites electrocatalysts for the oxygen reduction reaction. *International journal of hydrogen energy*, 30(9):1011–1015, 2005.

[137] Keith E Gubbins and Robert D Walker. The solubility and diffusivity of oxygen in electrolytic solutions. *Journal of The Electrochemical Society*, 112(5):469–471, 1965.

[138] Chao Wang, Hideo Daimon, Taigo Onodera, Tetsunori Koda, and Shouheng Sun. A general approach to the size-and shape-controlled synthesis of platinum nanoparticles and their catalytic reduction of oxygen. *Angewandte Chemie International Edition*, 47(19):3588–3591, 2008.

[139] Joelma Perez, Hebe M Villullas, and Ernesto R Gonzalez. Structure sensitivity of oxygen reduction on platinum single crystal electrodes in acid solutions. *Journal of Electroanalytical Chemistry*, 435(1-2):179–187, 1997.

[140] Hubert A Gasteiger, Shyam S Kocha, Bhaskar Sompalli, and Frederick T Wagner. Activity benchmarks and requirements for Pt, Pt-alloy, and non-Pt oxygen reduction catalysts for PEMFCs. *Applied Catalysis B: Environmental*, 56(1):9–35, 2005.

[141] Hubert A Gasteiger and Nenad M Marković. Just a dreamor future reality? *science*, 324(5923):48–49, 2009.

[142] Xingxu Yan, Kexi Liu, Tuo Wang, Yong You, Jianguo Liu, Peng Wang, Xiaoqing Pan, Guofeng Wang, Jun Luo, and Jing Zhu. Atomic interpretation of high activity on transition metal and nitrogen doped carbon nanofibers for catalyzing oxygen reduction. *Journal of Materials Chemistry A*, 5:3336–3345, 2017.

[143] UA Paulus, TJ Schmidt, HA Gasteiger, and RJ Behm. Oxygen reduction on a high-surface area Pt/Vulcan carbon catalyst: a thin-film rotating ring-disk electrode study. *Journal of Electroanalytical Chemistry*, 495(2):134–145, 2001.

[144] Yves Jean. *Molecular orbitals of transition metal complexes*. OUP Oxford, 2005.

[145] Barbara Gonzalez, Jay Kouba, Sharon Yee, Christopher A Reed, John F Kirner, and W Robert Scheidt. Manganese (II) porphyrins. synthesis, structures, and preference for five-coordination. *Journal of the American Chemical Society*, 97(11):3247–3249, 1975.

[146] James P Collman, JL Hoard, Nancy Kim, George Lang, and Christopher A Reed. Synthesis, stereochemistry, and structure-related properties of α, β, γ, δ-tetraphenylporphinatoiron (II). *Journal of the American Chemical Society*, 97(10):2676–2681, 1975.

[147] Paul Madura and W Robert Scheidt. Stereochemistry of low-spin cobalt porphyrins. 8. α, β, γ, δ-tetraphenylporphinatocobalt (II). *Inorganic Chemistry*, 15(12):3182–3184, 1976.

[148] Philip Coppens and Liang Li. Electron density studies of porphyrins and phthalocyanines. III. the electronic ground state of iron (II) phthalocyanine. *The Journal of chemical physics*, 81(4):1983–1993, 1984.

[149] Meng-Sheng Liao and Steve Scheiner. Electronic structure and bonding in metal porphyrins, metal= Fe, Co, Ni, Cu, Zn. *The Journal of chemical physics*, 117(1):205–219, 2002.

[150] Meng-Sheng Liao and Steve Scheiner. Electronic structure and bonding in metal phthalocyanines, metal= Fe, Co, Ni, Cu, Zn, Mg. *The Journal of Chemical Physics*, 114(22):9780–9791, 2001.

[151] Geoffrey A Williams, Brian N Figgis, Ronald Mason, Sax A Mason, and Peter E Fielding. Structure of phthalocyaninatocobalt (II) at 4.3 K: a neutron-diffraction study. *Journal of the Chemical Society, Dalton Transactions*, (9):1688–1692, 1980.

[152] Roald Hoffmann, Maynard ML Chen, and David L Thorn. Qualitative discussion of alternative coordination modes of diatomic ligands in transition metal complexes. *Inorganic Chemistry*, 16(3):503–511, 1977.

[153] DW Clack and JR Yandle. Electronic spectra of the negative ions of some metal phthalocyanines. *Inorganic Chemistry*, 11(8):1738–1742, 1972.

[154] Piter S Miedema, Matti M van Schooneveld, René Bogerd, Tulio CR Rocha, Michael Havecker, Axel Knop-Gericke, and Frank MF de Groot. Oxygen binding to cobalt and iron phthalocyanines as determined from in situ X-ray absorption spectroscopy. *The Journal of Physical Chemistry C*, 115(51):25422–25428, 2011.

[155] JR Kitchin, Jens Kehlet Nørskov, MA Barteau, and JG Chen. Modification of the surface electronic and chemical properties of Pt (111) by subsurface $3d$ transition metals. *The Journal of chemical physics*, 120(21):10240–10246, 2004.

[156] Zhiyao Duan and Guofeng Wang. Comparison of reaction energetics for oxygen reduction reactions on Pt (100), Pt (111), Pt/Ni (100), and Pt/Ni (111) surfaces: a first-principles study. *The Journal of Physical Chemistry C*, 117(12):6284–6292, 2013.

[157] José H Zagal, Sophie Griveau, J Francisco Silva, Tebello Nyokong, and Fethi Bedioui. Metallophthalocyanine-based molecular materials as catalysts for electrochemical reactions. *Coordination Chemistry Reviews*, 254(23):2755–2791, 2010.

[158] Justus Masa, Kenneth Ozoemena, Wolfgang Schuhmann, and José H Zagal. Oxygen reduction reaction using N_4-metallomacrocyclic catalysts: fundamentals on rational catalyst design. *Journal of Porphyrins and Phthalocyanines*, 16(07n08):761–784, 2012.

[159] J Zagal, M Paez, AA Tanaka, JR Dos Santos, and CA Linkous. Electrocatalytic activity of metal phthalocyanines for oxygen reduction. *Journal of Electroanalytical Chemistry*, 339(1-2):13–30, 1992.

[160] Ling Lin, Qing Zhu, and An-Wu Xu. Noble-metal-free Fe–N/C catalyst for highly efficient oxygen reduction reaction under both alkaline and acidic conditions. *Journal of the American Chemical Society*, 136(31):11027–11033, 2014.

[161] Alexey Serov, Kateryna Artyushkova, and Plamen Atanassov. Fe-N-C oxygen reduction fuel cell catalyst derived from carbendazim: Synthesis, structure, and reactivity. *Advanced Energy Materials*, 4(10), 2014.

[162] Wenmu Li, Jason Wu, Drew C Higgins, Ja-Yeon Choi, and Zhongwei Chen. Determination of iron active sites in pyrolyzed iron-based catalysts for the oxygen reduction reaction. *Acs Catalysis*, 2(12):2761–2768, 2012.

[163] Csaba E Szakacs, Michel Lefèvre, Ulrike I Kramm, Jean-Pol Dodelet, and François Vidal. A density functional theory study of catalytic sites for oxygen reduction in Fe/N/C catalysts used in H_2/O_2 fuel cells. *Physical Chemistry Chemical Physics*, 16(27):13654–13661, 2014.

[164] Jing Sun, Ya-Hui Fang, and Zhi-Pan Liu. Electrocatalytic oxygen reduction kinetics on Fe-center of nitrogen-doped graphene. *Physical Chemistry Chemical Physics*, 16(27):13733–13740, 2014.

[165] Alexey Titov, Peter Zapol, Petr Král, Di-Jia Liu, Hakim Iddir, Kopinjol Baishya, and Larry A Curtiss. Catalytic Fe-xN sites in carbon nanotubes. *The Journal of Physical Chemistry C*, 113(52):21629–21634, 2009.

[166] Duck Hyun Lee, Won Jun Lee, Won Jong Lee, Sang Ouk Kim, and Yong-Hyun Kim. Theory, synthesis, and oxygen reduction catalysis of Fe-porphyrin-like carbon nanotube. *Physical review letters*, 106(17):175502, 2011.

[167] Frank Abild-Pedersen, Jeff Greeley, Felix Studt, Jan Rossmeisl, TR Munter, Poul Georg Moses, Egill Skulason, Thomas Bligaard, and Jens Kehlet Nørskov. Scaling properties of adsorption energies for hydrogen-containing molecules on transition-metal surfaces. *Physical review letters*, 99(1):016105, 2007.

[168] Venkatasubramanian Viswanathan, Heine Anton Hansen, Jan Rossmeisl, and Jens K Nørskov. Universality in oxygen reduction electrocatalysis on metal surfaces. *ACS Catalysis*, 2(8):1654–1660, 2012.

[169] Marc TM Koper. Thermodynamic theory of multi-electron transfer reactions: Implications for electrocatalysis. *Journal of Electroanalytical Chemistry*, 660(2):254–260, 2011.

[170] Venkatasubramanian Viswanathan, Heine Anton Hansen, Jan Rossmeisl, and Jens K Nørskov. Unifying the $2e^-$- and $4e^-$-reduction of oxygen on metal surfaces. *The journal of physical chemistry letters*, 3(20):2948–2951, 2012.

[171] Dingshan Yu, Qiang Zhang, and Liming Dai. Highly efficient metal-free growth of nitrogen-doped single-walled carbon nanotubes on plasma-etched substrates for oxygen reduction. *Journal of the American Chemical Society*, 132(43):15127–15129, 2010.

[172] Linfei Lai, Jeffrey R Potts, Da Zhan, Liang Wang, Chee Kok Poh, Chunhua Tang, Hao Gong, Zexiang Shen, Jianyi Lin, and Rodney S Ruoff. Exploration of the active center structure of nitrogen-doped graphene-based catalysts for oxygen reduction reaction. *Energy & Environmental Science*, 5(7):7936–7942, 2012.

[173] Yan Jiao, Yao Zheng, Mietek Jaroniec, and Shi Zhang Qiao. Origin of the electrocatalytic oxygen reduction activity of graphene-based catalysts: a roadmap to achieve the best performance. *Journal of the American Chemical Society*, 136(11):4394–4403, 2014.

[174] Tan Xing, Yao Zheng, Lu Hua Li, Bruce CC Cowie, Daniel Gunzelmann, Shi Zhang Qiao, Shaoming Huang, and Ying Chen. Observation of active sites for oxygen reduction reaction on nitrogen-doped multilayer graphene. *ACS nano*, 8(7):6856–6862, 2014.

[175] Wei Ding, Zidong Wei, Siguo Chen, Xueqiang Qi, Tao Yang, Jinsong Hu, Dong Wang, Li-Jun Wan, Shahnaz Fatima Alvi, and Li Li. Space-confinement-induced synthesis of pyridinic- and pyrrolic-nitrogen-doped graphene for the catalysis of oxygen reduction. *Angewandte Chemie International Edition*, 52(45):11755–11759, 2013.

[176] Hai-Wei Liang, Xiaodong Zhuang, Sebastian Brüller, Xinliang Feng, and Klaus Müllen. Hierarchically porous carbons with optimized nitrogen doping as highly active electrocatalysts for oxygen reduction. *Nature communications*, 5, 2014.

[177] Donghui Guo, Riku Shibuya, Chisato Akiba, Shunsuke Saji, Takahiro Kondo, and Junji Nakamura. Active sites of nitrogen-doped carbon materials for oxygen reduction reaction clarified using model catalysts. *Science*, 351(6271):361–365, 2016.

[178] Juan Herranz, Frédéric Jaouen, Michel Lefèvre, Ulrike I Kramm, Eric Proietti, Jean-Pol Dodelet, Peter Bogdanoff, Sebastian Fiechter, Irmgard Abs-Wurmbach, Patrick Bertrand, et al. Unveiling N-protonation and anion-binding effects on Fe/N/C catalysts for o_2 reduction in proton-exchange-membrane fuel cells. *The Journal of Physical Chemistry C*, 115(32):16087–16097, 2011.

[179] Chang Hyuck Choi, Hyung-Kyu Lim, Min Wook Chung, Jong Cheol Park, Hyeyoung Shin, Hyungjun Kim, and Seong Ihl Woo. Long-range electron transfer over graphene-based catalyst for high-performing oxygen reduction reactions: importance of size, N-doping, and metallic impurities. *Journal of the American Chemical Society*, 136(25):9070–9077, 2014.

[180] Sheng Chen, Jiyu Bi, Yu Zhao, Lijun Yang, Chen Zhang, Yanwen Ma, Qiang Wu, Xizhang Wang, and Zheng Hu. Nitrogen-doped carbon nanocages as efficient metal-free electrocatalysts for oxygen reduction reaction. *Advanced materials*, 24(41):5593–5597, 2012.

[181] Qingying Jia, Nagappan Ramaswamy, Hasnain Hafiz, Urszula Tylus, Kara Strickland, Gang Wu, Bernardo Barbiellini, Arun Bansil, Edward F Holby, Piotr Zelenay, et al. Experimental observation of redox-induced Fe–N switching behavior as a determinant role for oxygen reduction activity. *ACS nano*, 9(12):12496–12505, 2015.

[182] Alfred B Anderson and Reyimjan A Sidik. Oxygen electroreduction on Fe^{II} and Fe^{III} coordinated to N_4 chelates. Reversible potentials for the intermediate steps from quantum theory. *The Journal of Physical Chemistry B*, 108(16):5031–5035, 2004.

[183] Shizhong Liu, Michael G White, and Ping Liu. Mechanism of oxygen reduction reaction on pt (111) in alkaline solution: Importance of chemisorbed water on surface. *The Journal of Physical Chemistry C*, 120(28):15288–15298, 2016.

[184] J Greeley, IEL Stephens, AS Bondarenko, Tobias Peter Johansson, Heine Anton Hansen, TF Jaramillo, Jan Rossmeisl, INJK Chorkendorff, and Jens Kehlet Nørskov. Alloys of platinum and early transition metals as oxygen reduction electrocatalysts. *Nature chemistry*, 1(7):552–556, 2009.

[185] Hanguang Zhang, Sooyeon Hwang, Maoyu Wang, Zhenxing Feng, Stavros Karakalos, Langli Luo, Zhi Qiao, Xiaohong Xie, Chongmin Wang, Dong Su, et al. Single atomic iron catalysts for oxygen reduction in acidic media: Particle size control and thermal activation. *Journal of the American Chemical Society*, 2017.

[186] Nastaran Ranjbar Sahraie, Ulrike I Kramm, Julian Steinberg, Yuanjian Zhang, Arne Thomas, Tobias Reier, Jens-Peter Paraknowitsch, and Peter Strasser. Quantifying the density and utilization of active sites in non-precious metal oxygen electroreduction catalysts. *Nature communications*, 6, 2015.